

2

Thesis

Quasi-two-dimensional Mott transition system
 $\text{Ca}_{2-x}\text{Sr}_x\text{RuO}_4$

Graduate School of Science, Kyoto University
Satoru Nakatsuji

October 16, 2000

Contents

1	Introduction	6
2	Phase diagram of new quasi-two-dimensional Mott transition system $\text{Ca}_{2-x}\text{Sr}_x\text{RuO}_4$	10
2.1	Experimental	10
2.2	Phase Diagram of $\text{Ca}_{2-x}\text{Sr}_x\text{RuO}_4$	11
3	Physical properties of each region of the phase diagram	13
3.1	Mott transition in $\text{Ca}_{2-x}\text{Sr}_x\text{RuO}_4$	13
3.1.1	New layered perovskite Mott insulator Ca_2RuO_4	13
3.1.2	Metal/non-metal transition	19
3.2	Antiferromagnetically correlated metallic state in Magnetic Metallic region	21
3.2.1	Broad peak in the susceptibility	21
3.2.2	Metamagnetic transition [20]	22
3.2.3	Broad peak in the specific heat	24
3.3	Second order structural transition in the metallic region	27
3.4	Ferromagnetic instability at $x_c \simeq 0.5$	33
3.4.1	Evolution of the temperature dependence of the susceptibility	33
3.4.2	Non-Fermi-liquid behavior of resistivity	39
3.4.3	Evolution of the temperature dependence of the specific heat	42
3.4.4	Observation of itinerant ferromagnetism at $x = 0.5$	47
3.5	Anisotropic transport properties	51

4	Discussion	57
4.1	Origin of the Magnetoelastic Coupling in Ca_2RuO_4	57
4.2	Ground State Crossover in the Metallic Region	58
4.2.1	Electronic Configuration of Sr_2RuO_4	58
4.2.2	Band Splitting Model	60
5	Conclusion	65
	Acknowledgement	67
A	Appendices	68
A.1	Synthesis of polycrystalline $\text{Ca}_{2-x}\text{Sr}_x\text{RuO}_4$	68
A.2	Crystal growth of $\text{Ca}_{2-x}\text{Sr}_x\text{RuO}_4$	73
	Bibliography	74

List of Tables

3.1	Cell parameters of Sr_2RuO_4 and Ca_2RuO_4	13
A.1	Optimized recipe for the synthesis of $\text{Ca}_{2-x}\text{Sr}_x\text{RuO}_4$	72

List of Figures

1.1	Phase diagram of $\text{La}_{2-x}\text{Sr}_x\text{CuO}_4$	7
1.2	Layered perovskite (K_2NiF_4 -type) structure	8
2.1	Phase diagram of $\text{Ca}_{2-x}\text{Sr}_x\text{RuO}_4$	12
3.1	X-ray spectra of Sr_2RuO_4 and Ca_2RuO_4 at room temperature	14
3.2	$\rho(T)$ of polycrystalline and single crystalline Ca_2RuO_4	15
3.3	$\chi(T)$ of polycrystalline Ca_2RuO_4	16
3.4	M - H curve for polycrystalline Ca_2RuO_4 at 5 K	16
3.5	$\chi(T)$ of single crystalline Ca_2RuO_4	18
3.6	C_p/T of single crystalline Ca_2RuO_4	19
3.7	$\rho_{ab}(T)$ for $\text{Ca}_{2-x}\text{Sr}_x\text{RuO}_4$	20
3.8	$\chi(T)$ of $\text{Ca}_{1.8}\text{Sr}_{0.2}\text{RuO}_4$ in the M-M region	22
3.9	M - H curve at 1.8 K for $\text{Ca}_{1.8}\text{Sr}_{0.2}\text{RuO}_4$ in the M-M region . .	23
3.10	In-plane spin-structure of AF ordered Ca_2RuO_4	24
3.11	C_p/T of single crystalline $\text{Ca}_{2-x}\text{Sr}_x\text{RuO}_4$	25
3.12	C_e/T of single crystalline $\text{Ca}_{2-x}\text{Sr}_x\text{RuO}_4$	26
3.13	$S(T)$ of single crystalline $\text{Ca}_{2-x}\text{Sr}_x\text{RuO}_4$	27
3.14	X-ray ($\text{Cu-}K\alpha$) diffraction spectra at room temperature for $\text{Ca}_{2-x}\text{Sr}_x\text{RuO}_4$	28
3.15	Cell parameters of $\text{Ca}_{2-x}\text{Sr}_x\text{RuO}_4$ at room temperature.	29
3.16	In-plane anisotropy of the susceptibility for $\text{Ca}_{1.8}\text{Sr}_{0.2}\text{RuO}_4$. .	30
3.17	Anisotropy ratio of $\chi_{ab}(T)$ for $\text{Ca}_{2-x}\text{Sr}_x\text{RuO}_4$	31
3.18	$\chi(T)$ for metallic region II and III of $\text{Ca}_{2-x}\text{Sr}_x\text{RuO}_4$	34
3.19	Curie-Weiss parameters for $\text{Ca}_{2-x}\text{Sr}_x\text{RuO}_4$	36
3.20	$\chi_{ab}^{-1}(T)$ for $x = 0.5$	38
3.21	$\chi(0)$ against x in the metallic regions II and III	39

3.22	$\rho_{ab}(T)$ for $x = 0.2, 0.5$ and 2	40
3.23	Longitudinal in-plane magnetoresistance for $x = 0.2$	41
3.24	C_e/T against $T^{1/2}$ for the metallic region II and III.	43
3.25	x dependence of the γ of $\text{Ca}_{2-x}\text{Sr}_x\text{RuO}_4$	44
3.26	γ vs $\ln \chi(0)$ for $\text{Ca}_{2-x}\text{Sr}_x\text{RuO}_4$	46
3.27	γ vs $\chi(0)^{1/2}$ for $\text{Ca}_{2-x}\text{Sr}_x\text{RuO}_4$	46
3.28	A jump in the low temperature C_e/T for $x = 0.5$	48
3.29	Low temperature dc SQUID magnetometer	49
3.30	Low temperature susceptibility for $x = 0.5$	50
3.31	$\rho_{ab}(T)$ of the metallic region II and III in $\text{Ca}_{2-x}\text{Sr}_x\text{RuO}_4$	52
3.32	$\rho_c(T)$ of the metallic region II and III in $\text{Ca}_{2-x}\text{Sr}_x\text{RuO}_4$	53
4.1	Band splitting model	59
4.2	Schematic view of the real space configuration of the orbital ordering	62
A.1	Phase diagram for synthesis of $\text{Ca}_{2-x}\text{Sr}_x\text{RuO}_4$	69
A.2	Detailed phase diagram for synthesis of CaSrRuO_4	70
A.3	Configuration of pellets on an Al_2O_3 crucible	73

Chapter 1

Introduction

Almost one and a half decades have passed since the discovery of high- T_c superconductivity in layered perovskite cuprates [1]. In addition to their remarkably high transition temperatures, the curious relation between superconductivity and insulator has made a strong impact of the discovery. After thoroughly extensive investigations, the phase diagram has been established as in Fig. 1.1, which revealed that the superconductivity appears just near an antiferromagnetic (AF) Mott insulator by carrier doping. This phase diagram has attracted considerable interest since it clearly demonstrates that the superconducting and insulating states, the two extremes of the ground states are inherently connected; in other words, the mechanism of superconductivity is crucially related with a Mott transition. Now the symmetry of the superconductivity has been determined to be d -wave, and as for the mechanism, it has gained a consensus that AF spin fluctuations in a strongly-correlated CuO_2 layer play an important role, as is expected from the phase diagram.

Since all the high- T_c superconductors have two-dimensional CuO_2 layers, it is natural to expect a new superconductor in the same layered perovskite oxides even without copper. Through searches worldwide, the first and still unique success has been made by our group in 1994 with the discovery of a new superconductivity in the copper-free material Sr_2RuO_4 [2]. In spite of its rather low $T_c = 1.5$ K, very extensive researches have been performed not only with the original motivation due to its close structural resemblance with the high- T_c cuprates (see Fig. 1.2), but for the possibility of an exotic

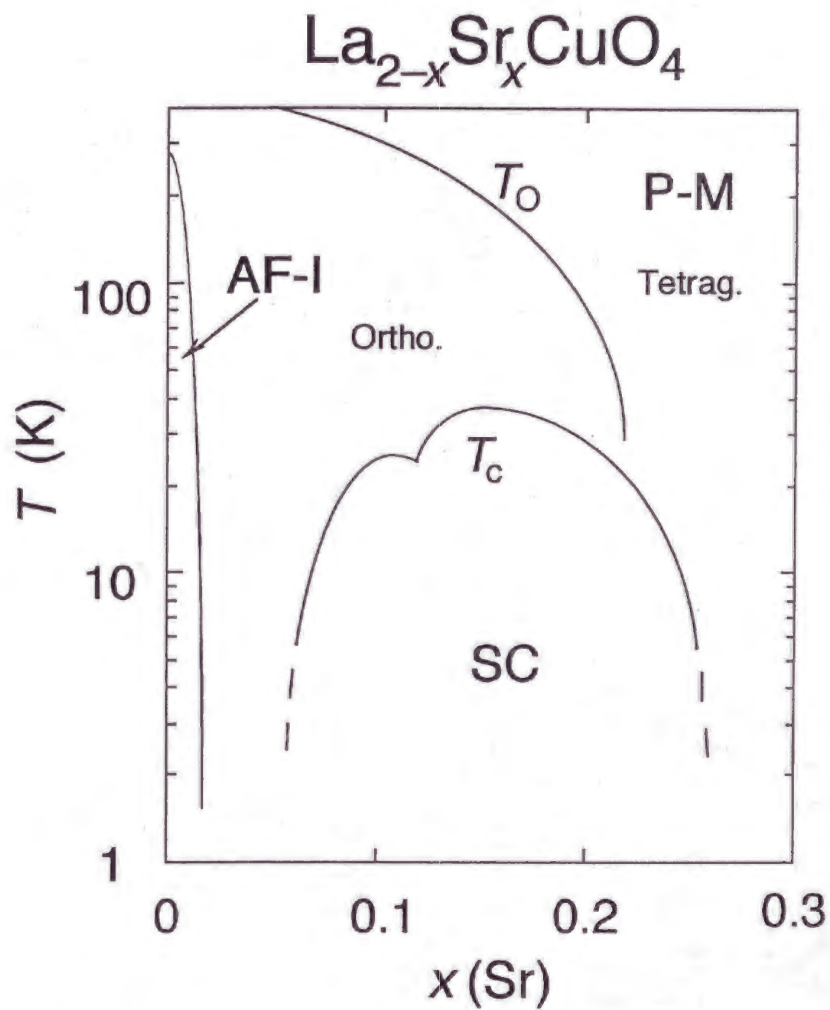


Figure 1.1: Phase diagram of $\text{La}_{2-x}\text{Sr}_x\text{CuO}_4$ with the abbreviations: P for paramagnetic, AF for antiferromagnetic, SC for superconducting phase, -M for metallic phase and -I for insulating phase. T_0 denotes the structural phase boundary between high temperature tetragonal and low temperature orthorhombic phases.

p -wave pairing, which has been recently confirmed by an NMR Knight shift measurement [3].

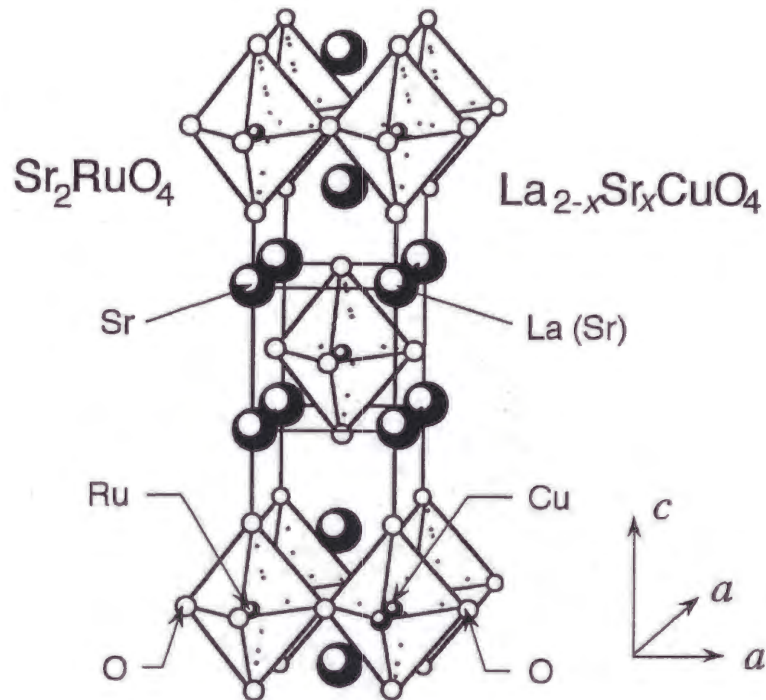


Figure 1.2: Layered perovskite (K_2NiF_4 -type) structure. Sr_2RuO_4 has the same K_2NiF_4 -type structure as one of the best studied high- T_c cuprates $La_{2-x}Sr_xCuO_4$.

Moreover, the studies have clarified that Sr_2RuO_4 is a quasi-two-dimensional Fermi liquid with strong electron-electron correlation [4, 5]. Therefore, as in the cuprates, it is expected that the p -wave superconductivity in Sr_2RuO_4 must be correlated with a Mott transition [6], and thereby that a Mott insulator exists among the related layered perovskite ruthenates.

In this study, we have succeeded in synthesizing a new layered perovskite Mott insulator Ca_2RuO_4 [7]. Moreover, we have revealed the magnetic and structural phase diagram of $Ca_{2-x}Sr_xRuO_4$: the complete solution system between Ca_2RuO_4 and Sr_2RuO_4 , by establishing their full synthesis and crystal growth [8, 9, 10]. The phase diagram of this new quasi-two-dimensional Mott transition system has revealed a new Mott transition route to the p -wave su-

perconductor. The phase diagram contains rich and unconventional physical phenomena due to the strong correlation among electrons in the multiple bands. It serves as a counterpart of the generic phase diagram established in the cuprates in the following aspects.

First, because Ca^{2+} and Sr^{2+} are isovalent, the p -wave superconductivity appears through the Mott transition by a band-width control, not by carrier doping as in cuprates. This establishes a new route to achieve unconventional superconductivity starting from a parent compound of quasi-two-dimensional Mott insulator.

Second, in contrast to the d -wave superconductivity appearing just next to the Mott transition in cuprates, we have revealed that the p -wave superconductivity emerges through the drastic change of magnetic coupling from AF to ferromagnetic (FM) one in the metallic phase. The appearance of the spin-triplet p -wave superconductivity through a ferromagnetic instability point by the band widening is an important result for the consideration of the mechanism of the p -wave superconductivity.

Third, while the cuprates have only a single band of $d_{x^2-y^2}$ orbital at the Fermi level, this system has triply degenerate t_{2g} bands. We have clarified that this orbital degree of freedom should play a crucial role in the exotic change of the itinerant magnetism, and also in the Mott transition.

The phase diagram with these rich and novel phenomena has established the only other example, after the cuprates, of how a Mott insulator evolves into an unconventional superconductor. Moreover, $\text{Ca}_{2-x}\text{Sr}_x\text{RuO}_4$ will provide an ideal model system to unveil generic roles of the orbital degree of freedom in the itinerant magnetism and superconductivity near a Mott transition.

In the following parts, we will first take a brief look at the phase diagram in Chap. 2, and then describe the evolution of the physical properties with the Sr substitution in this system in Chap. 3. Finally, we will discuss a unified picture to understand the sequence of exotic phenomena observed in this system in Chap. 4. The details for the preparations of polycrystalline and single crystalline samples will be presented in Appendices.

Chapter 2

Phase diagram of new quasi-two-dimensional Mott transition system



2.1 Experimental

We have succeeded in synthesizing polycrystalline samples and in growing single crystals of $\text{Ca}_{2-x}\text{Sr}_x\text{RuO}_4$ in the whole region of x ($0 \leq x \leq 2$). Details of the preparation will be described in Appendices [10]. The crystal structures were studied by powder X-ray diffraction analysis at room temperature. No trace of any second phase was found in the single crystals. For polycrystalline samples, almost all the spectra were identified as a single phase, except for minor peaks of CaO detected in several batches.

To determine the oxygen content, the thermogravimetric (TG) analysis was performed, in which powdered samples were heated up to 1200°C at a rate of $2^\circ\text{C}/\text{min}$ in a 90% Ar + 10% H_2 flow. All the results show one sharp decrease in the thermogravimetric weight around 440°C , corresponding to the decomposition reaction: $\text{Ca}_{2-x}\text{Sr}_x\text{RuO}_{4+\delta} \rightarrow (2-x)\text{CaO} + x\text{SrO} + \text{Ru} + (1 + \delta/2)\text{O}_2$. From these results, we determined δ values to be $-0.01(2)$ for the stoichiometric Ca_2RuO_4 (corresponding to 'S phase' in [7, 11, 12]), and $0.00(2)$ for $x = 0.09, 0.2, 1.0$ and 2.0 . As a result, all the members of $\text{Ca}_{2-x}\text{Sr}_x\text{RuO}_4$ essentially contain 4.0 oxygens per formula unit and the electronic configuration is $\{\text{Kr}\}4d^4$. Due to a large crystal field, Ru^{4+}

ions should be in the low-spin configuration t_{2g}^4 .

The electrical resistivity was measured by a standard four-probe dc method. Magnetization measurements from 330 K down to 1.8 K were made with a commercial SQUID magnetometer 'Quantum Design MPMS-5', equipped with a sample-stage rotator. For high temperature measurements up to 700 K, we used a sample space oven inserted into the magnetometer. For the magnetization measurements down to 0.26 K, we have constructed a SQUID magnetometer attached to a commercial ^3He refrigerator 'Oxford Instruments Heliox 2VL'. The specific heat was measured by a thermal relaxation method from 300 K to 0.4 K with 'Quantum Design PPMS'.

2.2 Phase Diagram of $\text{Ca}_{2-x}\text{Sr}_x\text{RuO}_4$

We have determined the phase diagram as represented in Fig. 2.1, which consists of the following three regions:

I. ($0 \leq x < 0.2$) An AF insulating ground state. A metal/non-metal (M/NM) transition occurs by varying temperature except $x = 0$. Ca_2RuO_4 ($x = 0$) is a Mott insulator at least up to 350 K [13, 14]. The M/NM transition by varying x occurs at $x \simeq 0.2$.

II. ($0.2 \leq x < 0.5$) An antiferromagnetically correlated metallic region, which we call 'Magnetic metallic (M-M) region', appears at low temperatures below the peak temperature T_P of the susceptibility. A second-order structural transition occurs at T_O between high temperature tetragonal and low temperature orthorhombic phases, and has its instability point at $x_c \simeq 0.5$.

III. ($0.5 \leq x \leq 2$) At $x = 0.5$ just near the structural instability point, and where T_P vanishes, a ferromagnetic ordering is found below about 0.5 K. Except this ferromagnetism at $x = 0.5$, a paramagnetic metallic phase spreads in this wide region. The low temperature susceptibility exhibits critical enhancement at $x = 0.5$ and decreases with x , as itinerant magnetism changes continuously from Curie like paramagnetism at $x = 0.5$ to enhanced Pauli paramagnetism at $x = 2.0$. Superconductivity occurs at $x = 2.0$ below $T_c = 1.5$ K.

In Chap. 3, we will describe these characteristic properties of each region

in order of the region I, II and III. Finally, the physical origin of this distinct variation of the ground state will be discussed in Chap. 4.

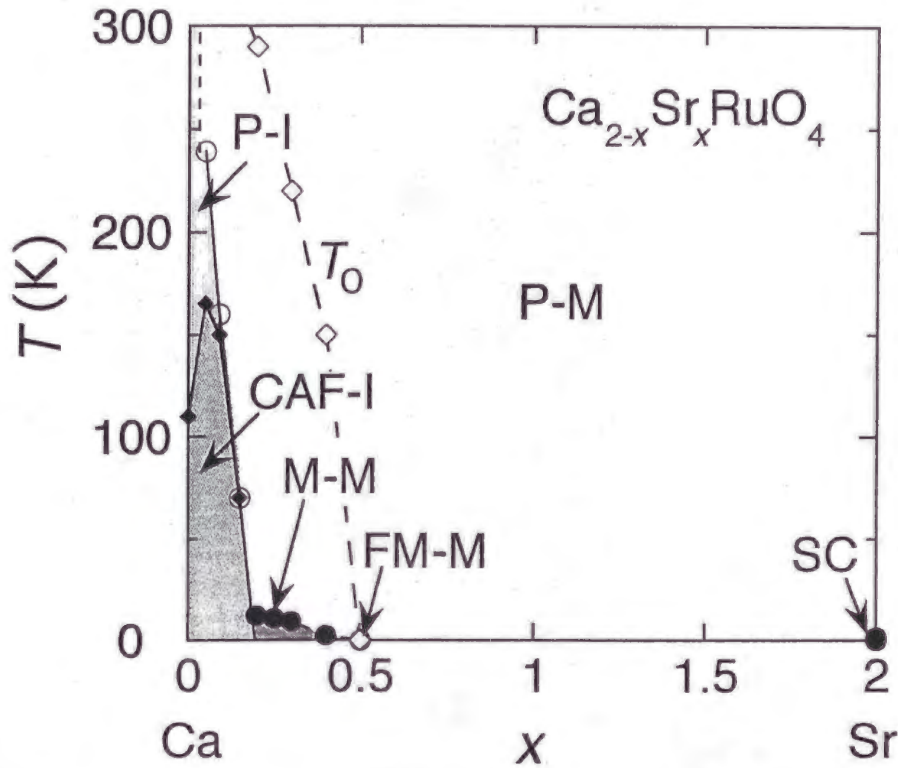


Figure 2.1: Phase diagram of $\text{Ca}_{2-x}\text{Sr}_x\text{RuO}_4$ with abbreviations: P for paramagnetic, CAF for canted antiferromagnetic, FM for ferromagnetic, M for magnetic, SC for superconducting phase, -M for metallic phase and -I for insulating phase. The boundaries are characterized by the peak temperature T_P of susceptibility for the [001] component (solid circle), the metal/non-metal transition temperature $T_{M/NM}$ (open circle) and the antiferromagnetic transition temperature T_N (solid diamond). T_O (open diamond) is the structural phase transition temperature between high temperature tetragonal and low temperature orthorhombic phases.

Chapter 3

Physical properties of each region of the phase diagram

3.1 Mott transition in $\text{Ca}_{2-x}\text{Sr}_x\text{RuO}_4$

3.1.1 New layered perovskite Mott insulator Ca_2RuO_4

As we mentioned in Chap. 1, we have found a new layered perovskite Mott insulator Ca_2RuO_4 [7]. In Fig. 3.1, we compare the results of powder X-ray diffraction measurements of Ca_2RuO_4 with that of Sr_2RuO_4 . The diffraction spectrum is basically similar to that of Sr_2RuO_4 , but somewhat more complicated; however, it is well indexed for an orthorhombic symmetry with the unit cell volume of $\sqrt{2}a_t \times \sqrt{2}a_t \times c_t$, where a_t and c_t are the parameters for an $I4/mmm$ cell. The parameters of the indexing are shown in Table 3.1 in comparison with those of Sr_2RuO_4 .

Table 3.1: Crystallographic information for Sr_2RuO_4 and Ca_2RuO_4 . Ca_2RuO_4 "S" denotes that it has stoichiometric oxygen content [7, 11].

Compound	Lattice	a (Å)	b (Å)	c (Å)	c/a	V (Å ³)
Sr_2RuO_4	tetragonal	3.870(2)	—	12.740(1)	3.29	190.8
Ca_2RuO_4 "S"	orthorhombic	5.402(2)	5.493(2)	11.932(3)		354.1
		3.820 ^{a)}	3.884 ^{a)}		3.10 ^{b)}	177.0 ^{c)}

a) Divided by $\sqrt{2}$ b) Multiplied by $\sqrt{2}$. c) Divided by 2.

The cell parameters and volume of Ca_2RuO_4 are substantially smaller

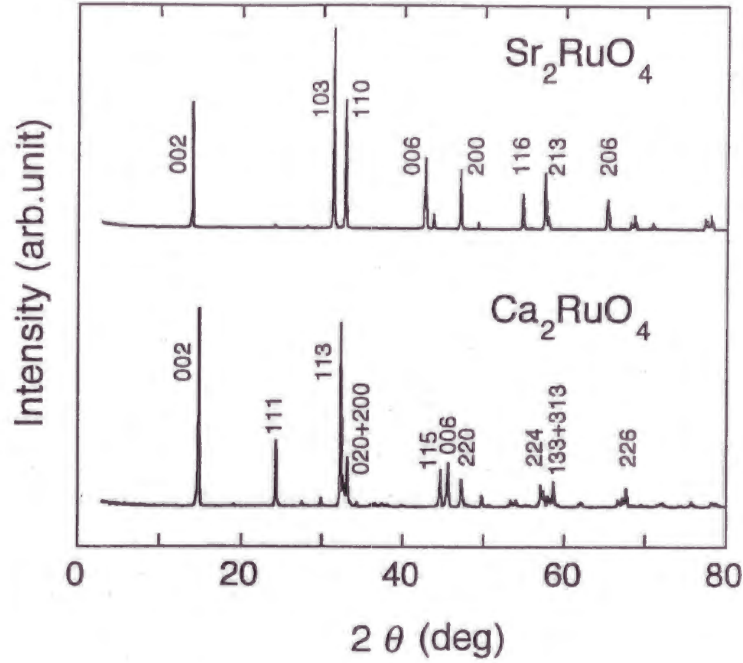


Figure 3.1: X-ray diffraction spectra of Sr_2RuO_4 and Ca_2RuO_4 at room temperature. Indices of the representative peaks are assigned according to the lattice symmetry in Table 3.1.

than those of Sr_2RuO_4 , reflecting the smaller ionic radius of Ca^{2+} than Sr^{2+} . The similarities in diffraction spectra and cell parameters indicate that the structure of Ca_2RuO_4 is of the same layered perovskite type as that of Sr_2RuO_4 . Therefore, the presence of the orthorhombic distortion is attributed to rotation and/or tilting of RuO_6 octahedra. This is in accord with the smaller tolerance factor $t = 0.903$ for Ca_2RuO_4 than $t = 0.949$ for Sr_2RuO_4 .

The structure refinements of Ca_2RuO_4 by powder neutron diffraction measurements have directly revealed the distortion including both rotation and tilt of RuO_6 [11].

The electrical resistivity $\rho(T)$ in Fig. 3.2 indicates insulating behavior of Ca_2RuO_4 . This is in sharp contrast with the metallic behavior of Sr_2RuO_4 , observed also in the polycrystalline samples. The temperature dependence is well fit to the activation-type behavior at all the temperatures measured with the activation energy of 0.20 eV.

The temperature dependence of the magnetic susceptibility $\chi(T) \equiv M/H$

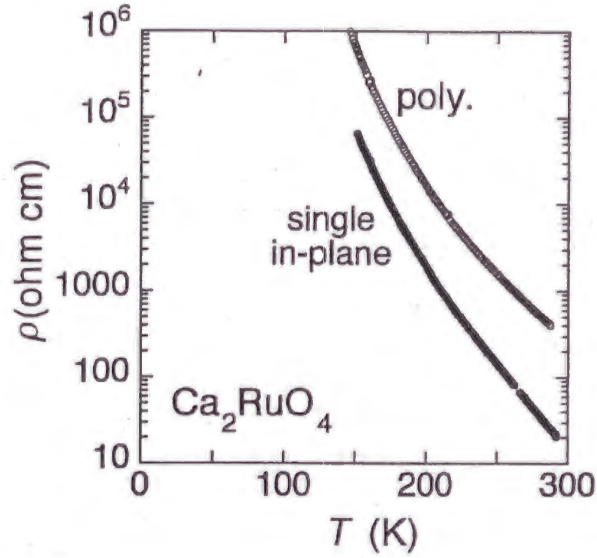


Figure 3.2: Temperature dependence of the resistivity of polycrystalline and single crystalline Ca_2RuO_4 .

of Ca_2RuO_4 is shown in Fig. 3.3 for the zero-field-cooled (ZFC) and field-cooled (FC) sequences. Fig. 3.4 is the magnetization vs the applied field (M - H curve) of the sample at 5 K. A significant cusp is observed near 110 K in both ZFC and FC $\chi(T)$ curves. In most preparations, an increase and a plateau in the FC susceptibility beginning near 160 K are observed on cooling, most likely due to the inclusion of a ferromagnetic (FM) impurity, which is now revealed to be Ca_2RuO_4 with excess oxygen [11]. Moreover, the less FM impurity is, the closer the FC curve approaches the ZFC curve with less increase near 160 K. The M - H curve also shows the same tendency: the less FM impurity, the less hysteresis. These tendencies and the cusp near 110 K in the $\chi(T)$ data indicate that there is an intrinsic transition near 110 K due to three-dimensional antiferromagnetic ordering of the Ru^{4+} moment. By the powder neutron measurement, it has been confirmed that the AF occurs in Ca_2RuO_4 at 110 K most likely with spin canting [11].

The above results indicate that the intraplanar Ru-Ru coupling of Ca_2RuO_4 is basically antiferromagnetic. This is consistent with our expectation that the intersite spin interaction of the insulating Ca_2RuO_4 is dominated by the antiferromagnetic superexchange interaction between half-filled, overlapping

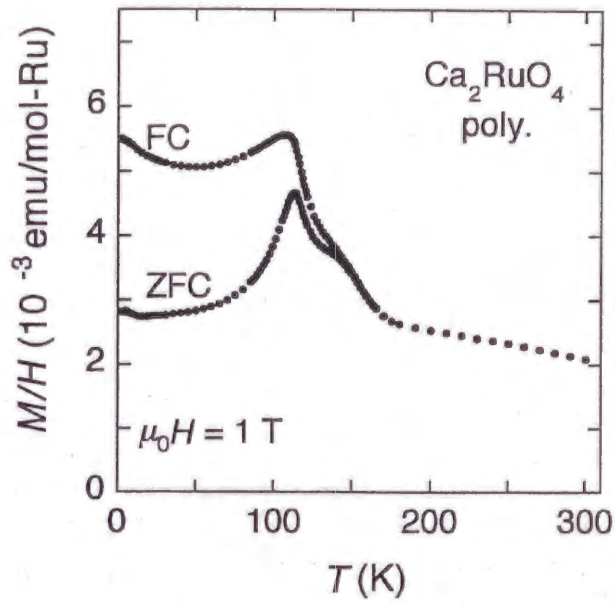


Figure 3.3: Temperature dependence of the susceptibility $\chi(T)$ of polycrystalline Ca_2RuO_4 under a field of $\mu_0 H = 1 \text{ T}$ between 2 K and 300 K. "ZFC" and "FC" represent the zero-field-cooled and field-cooled data, respectively.

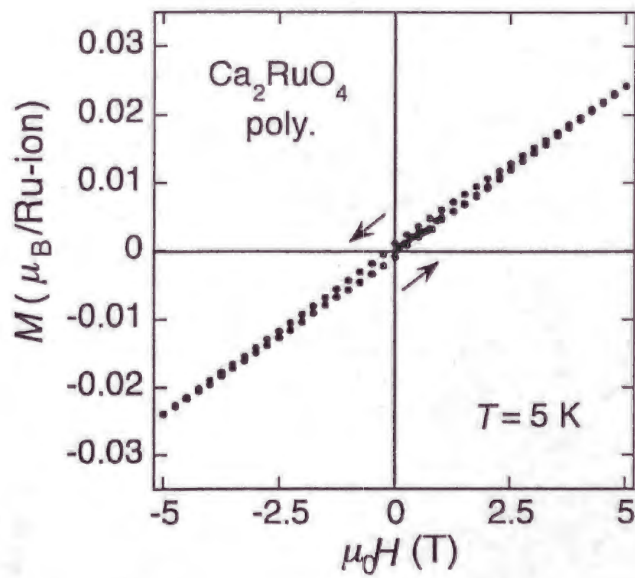


Figure 3.4: Magnetization vs applied field of polycrystalline Ca_2RuO_4 at 5 K.

t_{2g} orbitals, rather than the ferromagnetic one between the filled and the half-filled, nonoverlapping t_{2g} orbitals [15]. Dzyaloshinski-Moriya (D-M) interaction [16, 17] is probably the main mechanism for the canted moments in the RuO_2 planes because the distortion in Ca_2RuO_4 reduces the symmetry to enable the D-M interaction. The cusp near 110 K shown in Fig. 3.3 indicates that the canted moments in the successive layers interact antiferromagnetically with each other.

Just following us, Cao *et al.* have succeeded independently in growing the single crystal of Ca_2RuO_4 by a flux method [18]. They reported almost the same physical properties as that we characterized here, although they conclude that the temperature dependence of the in-plane resistivity is the three-dimensional variable-hopping-type. They also performed the heat capacity measurement and obtained the electronic specific heat coefficient $\gamma = 4 \text{ mJ/molK}^2$ suggestive of the localized metallic ground state with the density of states (DOS) remaining at the Fermi level.

Recently, we have also succeeded in growing single crystals of Ca_2RuO_4 by a floating zone (FZ) method, and revealed the anisotropy of $\chi(T)$ and $\rho(T)$ as in Fig. 3.5 and 3.2, respectively [12]. $\chi(T)$ shows a distinct AF transition at 110 K with the easy-axis along $[110]$ and the hard-axis along $[1\bar{1}0]$. The ZFC and FC curves almost coincide with each other, which indicates that the crystals are nearly free from the FM impurities found in the polycrystalline samples. We also observed basically an activation-type temperature dependence in $\rho_{ab}(T)$ with the activation energy of 0.2 eV. These results are fully consistent with those obtained by polycrystalline samples.

Moreover, the temperature dependence of the specific heat has been measured using the single crystals. Fig. 3.6 shows the result of C_p/T , from which we derived $\gamma = 0.0(2) \text{ mJ/molK}^2$ and Debye temperature $\Theta_D = 420 \text{ K}$. This γ value supports the result that Ca_2RuO_4 is truly an insulator down to low temperatures, and cast doubts on the results by Cao *et al.* [18], which claims that Ca_2RuO_4 may be understood as a localized metal. The difference between two crystals may arise from the differences in the crystal growth methods or in the oxygen stoichiometry. As we will discuss in Appendix A.2, the sample is basically free from the contamination during its growth by our FZ method,

while crystals grown by the flux-method which Cao *et al.* used are known to be susceptible to contaminations from Cl-flux and a Pt crucible.

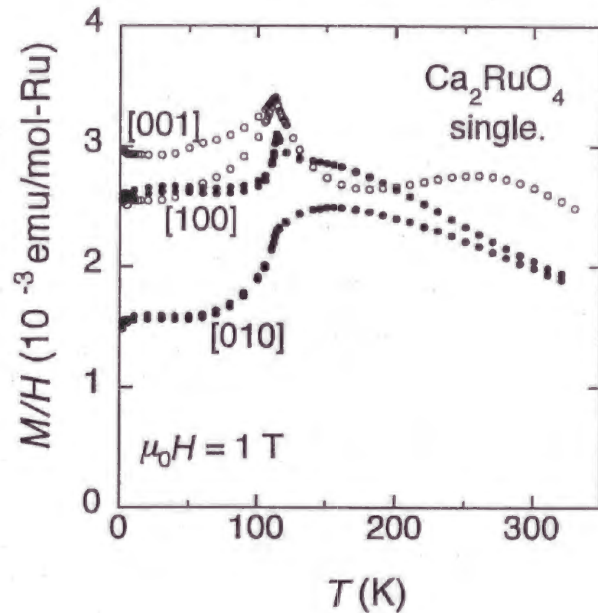


Figure 3.5: Temperature dependence of the susceptibility $\chi(T)$ of single crystalline Ca_2RuO_4 under a field of $\mu_0 H = 1$ T along each axis. All the data are taken under the zero-field-cooled condition.

These results of magnetic measurements of Ca_2RuO_4 fully confirm anti-ferromagnetic ground state within a basal plane. A simple band insulator would show no magnetic order because it has equally-filled bands of up-spin and down-spin electrons. Therefore, Ca_2RuO_4 should not be a band insulator. Taking their integer-filling configuration into account, we conclude that Ca_2RuO_4 is a Mott insulator. This is also consistent with the fact that the neighboring ruthenate Sr_2RuO_4 has strong electron-electron correlations with $U/W \simeq 1.7$. (U is the on-site Coulomb energy and W is the band width.) In Sr_2RuO_4 , the electronic states in the immediate vicinity of the Fermi energy are formed by the anti-bonding $dp\pi^*$ band and dominated by Ru-4d character, not by O-2p character [19]. Therefore, Ca_2RuO_4 is a Mott-Hubbard-type insulator, rather than charge-transfer-type one.

It is naively expected that W of Ca_2RuO_4 is larger than that of Sr_2RuO_4 , since the Ru-O distance in the RuO_2 plane is shorter in Ca_2RuO_4 with the

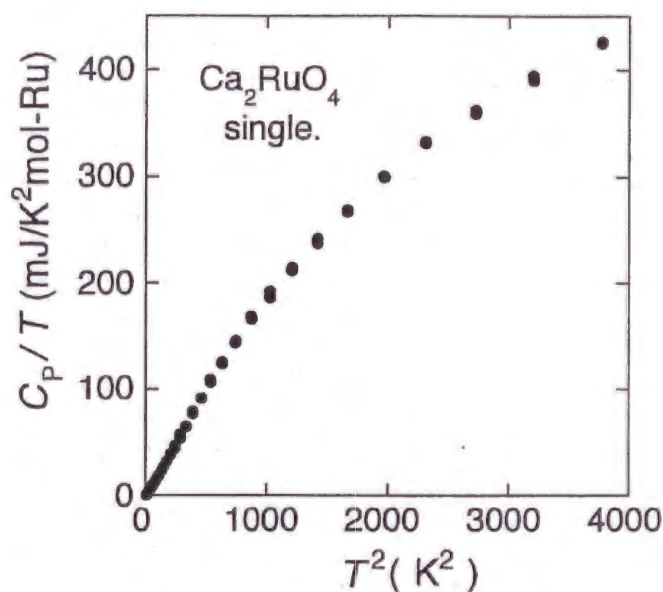


Figure 3.6: Temperature dependence of the specific heat divided by temperature C_p/T for single crystalline Ca_2RuO_4 .

smaller size of Ca^{2+} compared with Sr^{2+} , leading to the stronger overlap of the wave functions. Considering that U should take the intrinsic value for Ru^{4+} ion and does not change in the first approximation, Ca_2RuO_4 would have smaller U/W and be metallic. The experimental results, however, show that Ca_2RuO_4 is an insulator. This indicates that, contrary to the naive expectation above, Ca_2RuO_4 has a larger value of U/W , that is, a smaller W than Sr_2RuO_4 . The smaller band-width is due to distortions such as rotations and buckling in the RuO_2 plane which are absent in Sr_2RuO_4 . These distortions, which are the cause of the orthorhombicity in Ca_2RuO_4 , reduce the overlap between the $\text{Ru-}4d$ orbitals mediated by the $\text{O-}2p$ orbital and bring the decrease of W .

3.1.2 Metal/non-metal transition

In contrast to the Mott insulator Ca_2RuO_4 , slight Sr substitution for Ca stabilizes a metallic state at high temperatures, and induces a M/NM transition at a temperature $T_{\text{M/NM}}$ on cooling as in Fig. 2.1. The results of $x = 0.09$ and 0.15 in Fig. 3.7 represent $\rho_{\text{ab}}(T)$ for the region I with $T_{\text{M/NM}} \simeq 155$

K and 65 K, respectively. With abrupt increases by factors more than 10^4 at $T_{M/NM}$, they show the non-metallic behavior described by variable-range hopping. For $x = 0.15$, for example, the data below $T_{M/NM}$ well fits $\rho_{ab}(T) = A \exp(T_0/T)^{1/4}$ with $T_0 = 9 \times 10^4$ K. This suggests that strong localization dominating the non-metallic behavior drives the M/NM transition, preceding the gap opening toward the Mott insulator. Below $T_{M/NM}$, the

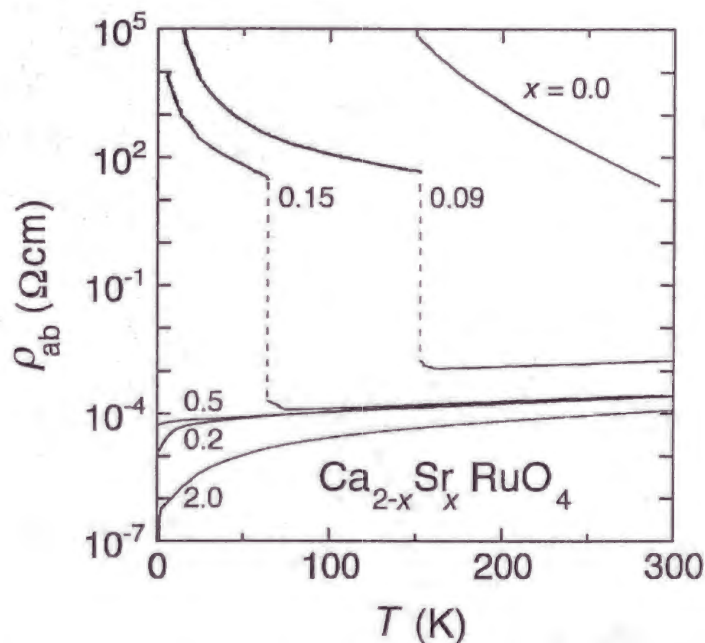


Figure 3.7: Temperature dependence of the in-plane resistivity $\rho_{ab}(T)$ for $\text{Ca}_{2-x}\text{Sr}_x\text{RuO}_4$ with different values of x . The vertical broken lines are guides to the eye.

susceptibility χ also shows a distinct magnetic transition at a temperature T_{CAF} on cooling, which finally coincides with the M/NM transition for about $x \geq 0.1$. The magnetization vs. the field (M - H curve) at 5 K exhibits weak FM hysteresis ascribable to canted AF as in Ca_2RuO_4 [7, 11]. The M/NM transition of the ground state occurs at $x \simeq 0.2$, as illustrated in Fig. 3.7.

Powder neutron diffraction measurements have been carried out for $x = 0.1$ and 0.2 down to 1.5 K [11], and have shown that the M/NM transition either by varying x or T involves the first-order structural transition, consistent with the thermal hystereses observed in $\rho(T)$ and $\chi(T)$.

3.2 Antiferromagnetically correlated metallic state in Magnetic Metallic region

3.2.1 Broad peak in the susceptibility

What characterizes the M-M region in the region II is the susceptibility peak. Figure 3.8 shows $\chi(T)$ curves for $x = 0.2$ under fields of 1 T parallel to the $[110]$, $[1\bar{1}0]$ and $[001]$ axes. The in-plane susceptibility exhibits the maximum and the minimum for fields along $[110]$ and $[1\bar{1}0]$, respectively. There is no observable difference between field-cooled and zero-field-cooled data, so our measurements are not suggestive of spin glass ordering. The most prominent feature is the broad maximum in each axis component. Well above T_P , these components show Curie-Weiss (C-W) behavior with AF Weiss temperatures Θ_W comparable to T_P . Such characteristics indicate that some kind of AF ordering occurs at T_P .

However, the broad nature of these maxima is far from the usual sharp cusp at a Néel point. Moreover, the peak temperatures T_P for the in-plane components are definitely different from each other: $T_P^{[110]}$ for the easy-axis $[110]$ is 8.2 K, while $T_P^{[1\bar{1}0]}$ for the hard axis $[1\bar{1}0]$ is 12.2 K, identical to that for c-axis $[001]$. Therefore, although the substantial reduction of the susceptibility should originate from the AF correlation, the long-range order (LRO) does not emerge at T_P but is somehow destabilized. In fact, within the resolution limit of $0.05 \mu_B$, no magnetic LRO was detected for $x = 0.2$ down to 1.5 K in the neutron diffraction measurement [13].

Another evidence for the AF correlation in the M-M region is the anisotropy of the susceptibility below T_P . As shown in Fig. 3.8, the $[110]$ component decreases on cooling almost three times more than the others. This corresponds to the anisotropy for an AF ordering with the easy-axis $[110]$ and with the hard-axes $[1\bar{1}0]$ and $[001]$. In fact, the anisotropy obtained here is very similar to that of AF-LRO state in Ca_2RuO_4 [12], with spins aligned antiferromagnetically along the $[110]$ axis [11]. Moreover, the M - H curve in this region exhibits a metamagnetic transition (for example, at $\mu_0 H \approx 2.3$ T $\parallel [110]$ for $x = 0.2$), similar to the one observed in the ordered Ca_2RuO_4 [18], as we will describe in detail in Sec 3.2.2. These substantial resemblances in-

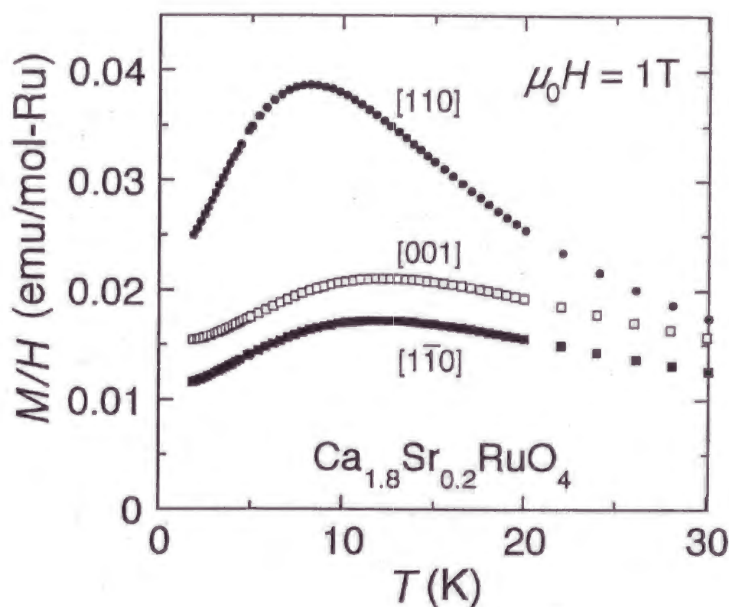


Figure 3.8: Temperature dependence of the susceptibility of $\text{Ca}_{1.8}\text{Sr}_{0.2}\text{RuO}_4$ under $\mu_0 H = 1$ T parallel to each axis. Field-cooled and zero-field-cooled curves agree very well.

dicates that an AF short-range order (SRO) is well stabilized in the magnetic *metallic* region just next to the M/NM transition.

3.2.2 Metamagnetic transition [20]

As we mentioned above, we have observed definite metamagnetization in the M-M region, under the field along the easy-axis [110] below T_P . Figure 3.9 displays the M - H curves for $\text{Ca}_{1.8}\text{Sr}_{0.2}\text{RuO}_4$ measured at 1.8 K under the field up to 5 T parallel to the [110], $[1\bar{1}0]$ and [001] axes. In contrast with the linear dependence observed at 50 K (not shown), the magnetization curves for 1.8 K show a distinct field dependence. Especially, the [110] curve shows a metamagnetic transition at $\mu_0 H \approx 2.3$ T. For the other components, the transition is likely to occur at fields higher than 5 T.

The direction of the easy axis along [110] is consistent with the magnetic structure in the AF insulating state of Ca_2RuO_4 [11], which is schematically shown in Fig. 3.10. From the [110] curve, the saturated moment determined through the extrapolation to the zero field is around $0.3 \mu_B$, which is almost

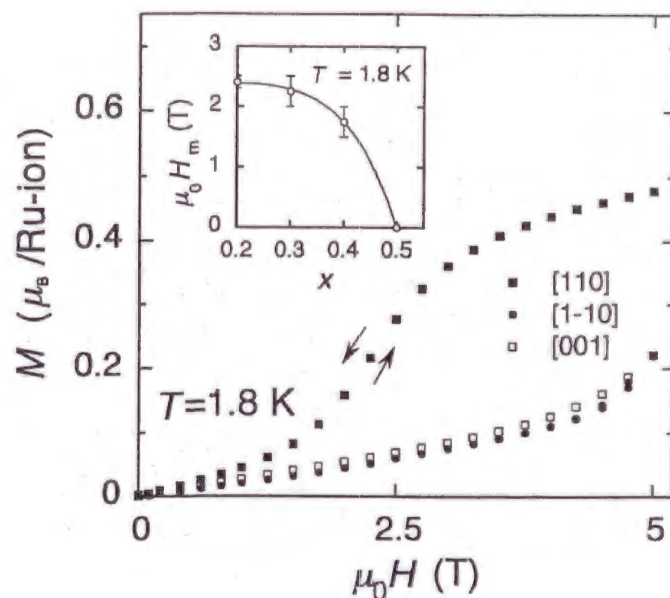


Figure 3.9: M - H curve at 1.8 K under the magnetic field up to 5 T parallel to each axis for $\text{Ca}_{1.8}\text{Sr}_{0.2}\text{RuO}_4$. All the data show no hysteresis. The inset displays the x dependence of the metamagnetic transition field H_m . The line is a guide to the eye.

the same as the in-plane ferromagnetic component in the canted AF-LRO state in Ca_2RuO_4 [11]. These similarities again suggest that the in-plane AF correlation observed in the insulating Ca_2RuO_4 should survive even in this magnetic metallic region just next to the M/NM transition. The metamagnetic transition is ascribable to the destruction of the AF-SRO state by the applied field. On the other hand, considering its layered structure, another spin configuration of the in-plane ferromagnetic SRO, coupled antiferromagnetically between adjacent layers, is still possible. Neutron diffuse scattering study is needed to clarify which of the possibilities is realized in this system.

In the inset of Fig. 3.9, we display the x dependence of H_m under the field parallel to the [110] axis. We defined H_m as the field where the M - H curve has the largest derivative. The larger error-bar with x reflects the broader transition. The field H_m enhances with decreasing x , indicating the evolution of the AF correlation toward the Mott transition.

On the other hand, H_m diminishes to zero around $x \simeq 0.5$. It is at this

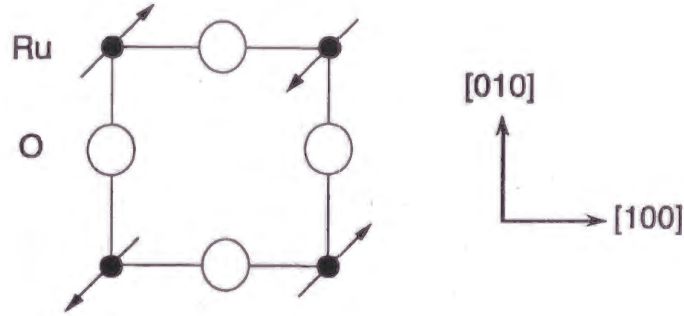


Figure 3.10: Schematic picture of the in-plane spin-structure of AF ordered Ca_2RuO_4 . The canting of the spins are not shown. The notation for $I4/mmm$ symmetry cell is adopted here.

same point that the low temperature susceptibility critically enhances as described in Sec. 3.4.1 and also T_P goes down to zero. This critical behavior indicates that the magnetic properties of the ground state drastically changes at the zero-temperature point at $x_c \simeq 0.5$. This critical behavior suggests the enhanced quantum fluctuation in the M-M region which destabilizes the underlying magnetic LRO. In fact, $x_c \simeq 0.5$ corresponds to the structural quantum critical point as we will describe in Sec. 3.3.

3.2.3 Broad peak in the specific heat

Figure 3.11 represents the temperature dependence of the specific heat divided by temperature C_p/T for all the region of x of $\text{Ca}_{2-x}\text{Sr}_x\text{RuO}_4$. We assume that C_p/T consists of the electronic and lattice contributions

$$C_p/T = C_e/T + C_{\text{lat}}/T, \quad (3.1)$$

$$C_e/T \equiv \gamma T. \quad (3.2)$$

In order to derive systematic change of C_e/T over a wide range of the temperature, we need to estimate C_{lat}/T . Fortunately, C_p/T of the Mott insulator Ca_2RuO_4 gives the fairly reliable evaluation of the lattice contribution C_{lat}/T . Ca_2RuO_4 shares basically the same structure in this system and moreover should have neither electronic nor magnetic contribution to C_p/T

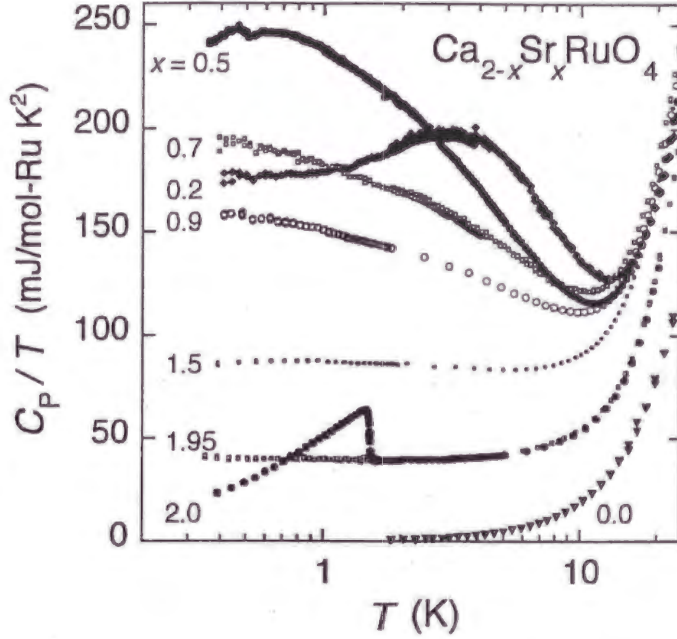


Figure 3.11: Temperature dependence of the specific heat divided by the temperature C_p/T for single crystalline $\text{Ca}_{2-x}\text{Sr}_x\text{RuO}_4$ with variable x .

at low temperatures. In fact, it is a well defined insulator with the relatively large activation energy gap of 0.2 eV. Moreover, the AF transition freezes the spin degree of freedom so that C_p/T well below its Néel temperature 110 K should not have strong contribution from magnetic fluctuations.

At low temperatures, the C_p/T of a conventional non-magnetic, non-superconductive material is [21]

$$C_p/T = A_1T + A_3T^3 + A_5T^5 + A_7T^7 + A_9T^9 + \dots, \quad (3.3)$$

where $\gamma \equiv A_1$ and $\beta \equiv A_2$. The Debye temperature Θ_D is determined by the relation $\Theta_D = (1.944 \times 10^6 r/\beta)^{1/3}$, where r is the number of atoms per formula unit ($r = 7$ here) and β is in units of mJ/mol K^4 . We performed the fitting of Eq. (3.3) to the data for Ca_2RuO_4 up to 80 K and obtained $\gamma = 1(1) \text{ mJ/mol K}^2$ and $\Theta_D = 410 \text{ K}$, which are consistent with the results in Sec. 3.1.1. We derived the C_e/T using the lattice contribution estimated by the above fitting, as shown in Fig. 3.12. Here, we focus on the C_e/T for $\text{Ca}_{1.8}\text{Sr}_{0.2}\text{RuO}_4$ in the M-M region ($0.2 \leq x \leq 0.5$). We will discuss results

for other regions in Sec. 3.4.3.

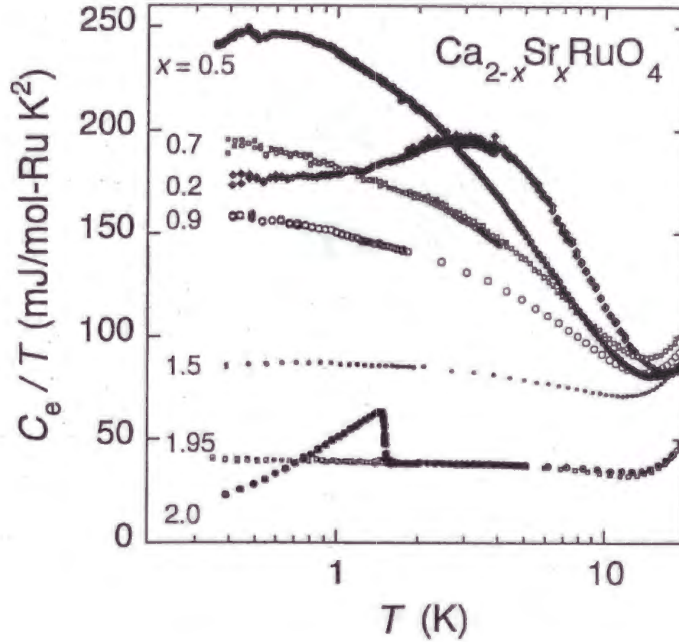


Figure 3.12: Temperature dependence of the electronic part of the specific heat divided by the temperature C_e/T for single crystalline $\text{Ca}_{2-x}\text{Sr}_x\text{RuO}_4$ with variable x .

As we discussed in Sec. 3.2.1, the susceptibility shows a clear peak at $T_P \simeq 10$ K for $x = 0.2$. Likewise, C_e/T forms a broad peak at around $T_P^\gamma = 2.8$ K, well below T_P . It should also be noted that the enhancement of C_e/T to form the peak starts around 12 K close to T_P . Taking account of the fact that the AF-SRO presumably starts to appear below T_P , this peak in C_e/T should be the result of the entropy release due to the formation of AF-SRO. In fact, the temperature dependence of the electronic entropy (see Fig. 3.13) calculated by

$$S(T) = \int_0^T \frac{C_e}{T} dT \quad (3.4)$$

shows sharp change around 3 K, which becomes a little moderate above 10 K. The entropy release below 10 K is so large as about one thirds of $R \ln 2$.

According to the relation

$$S = R \ln(2S_{\text{eff}} + 1), \quad (3.5)$$

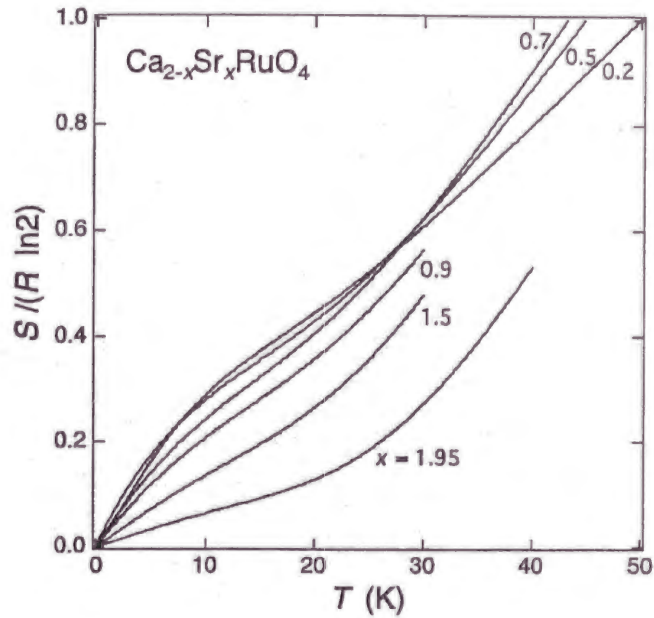


Figure 3.13: Temperature dependence of the electronic entropy $S(T)$ for single crystalline $\text{Ca}_{2-x}\text{Sr}_x\text{RuO}_4$ with variable x .

the effective spin S_{eff} involved in the release below T_P is about a half of spin $1/2$. As we will discuss in Sec. 3.4.1, the estimated localized spin at high temperatures in this system is close to spin $1/2$. The strong spin fluctuation expected due to the structural low dimensionality and the orbital degree of freedom may explain the reduced S_{eff} in comparison with spin $1/2$. Another important point is that the T_P^γ has almost the same energy scale as the metamagnetic transition field $\mu_0 H \approx 2.3$ T. This suggests a crude picture that it is at T_P^γ that the coherence length of AF-SRO, which starts to grow rapidly below around T_P , becomes sizable in the bulk system.

3.3 Second order structural transition in the metallic region

In Fig. 3.14, we display the results of X-ray diffraction measurements of powdered single crystals for $x = 0.09, 0.2$ and 2 . All diffraction spectra are similar to each other, reflecting the basic K_2NiF_4 -type structure. Especially, the results of Sr_2RuO_4 ($x = 2.0$) and $x = 0.2$ agree with the same tetragonal symmetry. Meanwhile, the spectrum of $x = 0.09$ shows weak but definite or-

thorhombicity with splitting between (hkl) and (khl) peaks. As an example, the inset of Fig. 3.14 shows that (110) peak of $x = 0.2$ splits into (200) and (020) peaks of $x = 0.09$. Accordingly, the result of $x = 0.09$ is well indexed with an orthorhombic unit cell with a volume of $\sqrt{2}a_t \times \sqrt{2}a_t \times c_t$, where a_t and c_t are parameters for an $I4/mmm$ cell. This is a situation similar to the case of Ca_2RuO_4 ($x = 0$) with an orthorhombic Pbca symmetry [7, 11].

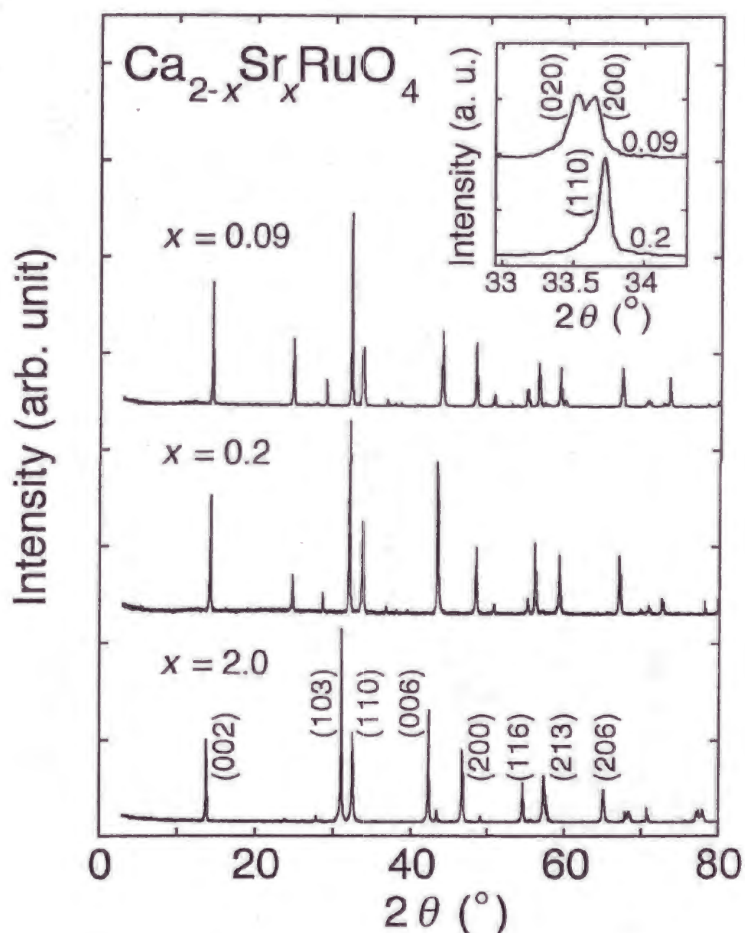


Figure 3.14: X-ray ($\text{Cu-}K\alpha$) diffraction spectra at room temperature for $\text{Ca}_{2-x}\text{Sr}_x\text{RuO}_4$ with $x = 0.09, 0.2$ and 2 . The inset shows that the (110) peak of $x = 0.2$ splits into the (020) and (200) peaks for $x = 0.09$. For the inset, the $K\alpha_2$ component has been subtracted.

The cell parameters for all the regions are shown in Fig. 3.15. In order to obtain an overall view, we adopted the $I4/mmm$ cell for the tetragonal lattice,

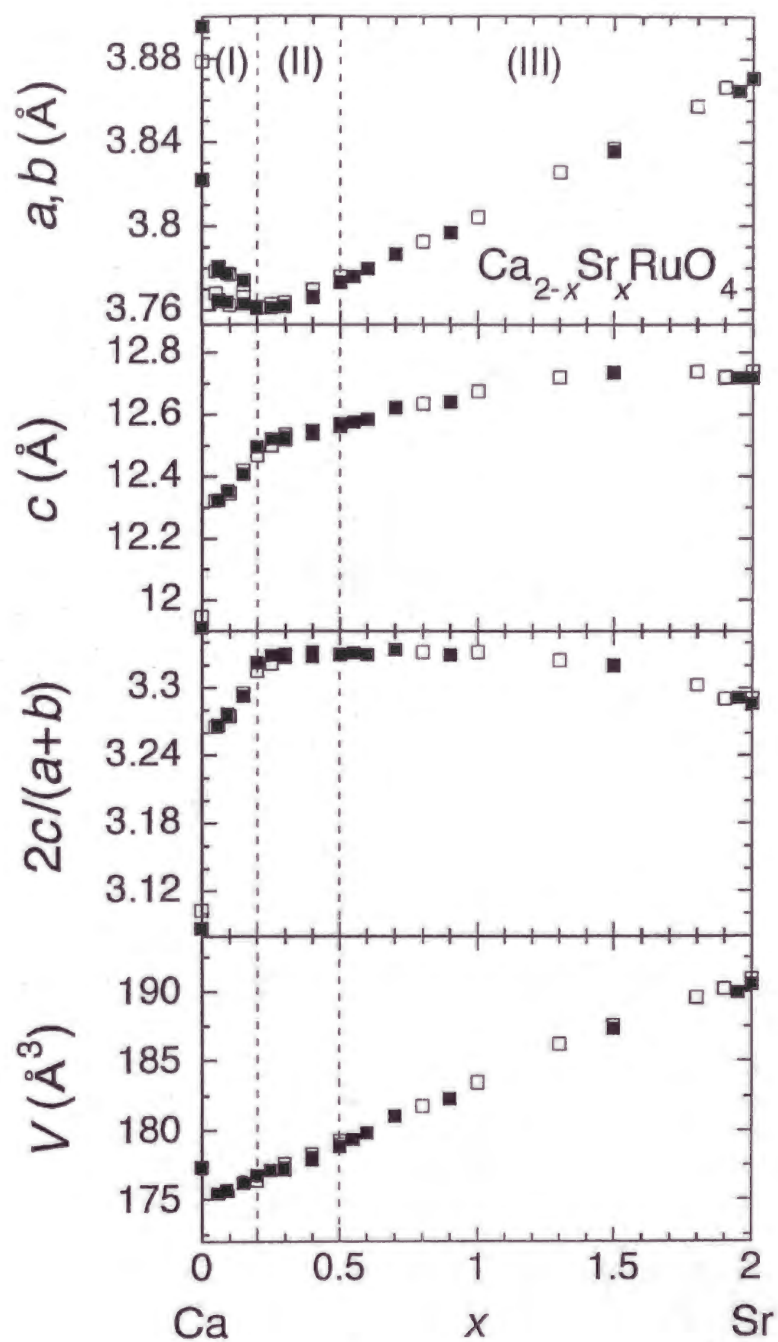


Figure 3.15: Cell parameters a , b , c , $2c/(a + b)$ and unit cell volume V of $\text{Ca}_{2-x}\text{Sr}_x\text{RuO}_4$ at room temperature. The open and solid squares represent those parameters of polycrystalline and single crystalline samples, respectively.

the same as that of Sr_2RuO_4 , while for the orthorhombic one, $a/\sqrt{2}$ and $b/\sqrt{2}$ are given instead of a and b . At each composition, the parameters for single crystalline samples agree well with those for polycrystalline ones. This indicates that the nominal composition x for each single crystal is essentially the same as the actual composition.

Starting from Sr_2RuO_4 , the volume decreases continuously with the Ca substitution owing to the smaller size of Ca^{2+} than that of Sr^{2+} . However, there are clear kinks without discontinuity in a , b and c at $x = 0.2$, where the splitting between a and b starts in region I (see also Fig. 2.1). This clearly reveals a structural transition at room temperature from a tetragonal phase in region II and III, to an orthorhombic one in region I. Finally, near $x = 0$, there is a large jump of the cell parameters due to a first order structural transition, accompanied by the M/NM transition [8, 13]. Therefore, the orthorhombic symmetry of the metallic phase in region I should be different from the orthorhombic Pbca symmetry of the insulating phase.

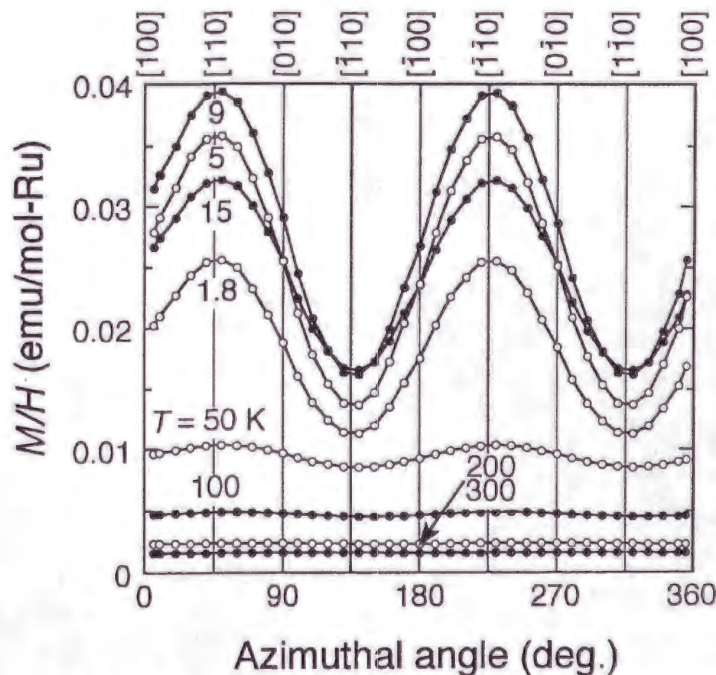


Figure 3.16: In-plane anisotropy of the susceptibility under $\mu_0 H = 1$ T for $\text{Ca}_{1.8}\text{Sr}_{0.2}\text{RuO}_4$ at different temperatures.

In region II, the susceptibility $\chi(T)$ shows a broad peak at the temperature T_P , which characterizes the AF correlation in the M-M region [8]. At the same time, it exhibits another important aspect, namely the in-plane anisotropy. The azimuthal angle dependence of the in-plane susceptibility at various temperatures is displayed in Fig. 3.16 for $x = 0.2$. In comparison with the isotropic dependence at high temperatures, the anisotropy with two-fold symmetry becomes evident as the temperature decreases. In order to quantify this temperature dependence, we define $R(T)$ as the susceptibility ratio of the easy-axis $[110]$ to the hard-axis $[1\bar{1}0]$. Figure 3.17 shows that $R(T)$ for $x = 0.2$ increases on cooling and reaches more than 200% below $T_P \simeq 12$ K. It is worth noting that, as in the inset of Fig. 3.17, $R(T)$ for $x = 0.2$ starts to deviate from the isotropic value of 100% at a characteristic temperature $T_0 \simeq 290$ K.

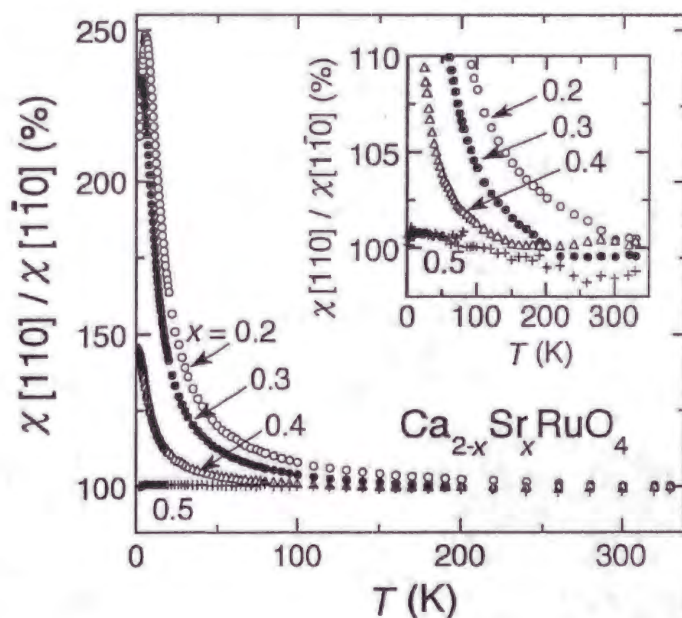


Figure 3.17: Temperature dependence of the anisotropy ratio of the in-plane susceptibilities: $R(T) = \chi[110]/\chi[1\bar{1}0]$ for $\text{Ca}_{2-x}\text{Sr}_x\text{RuO}_4$ with $x = 0.2, 0.3, 0.4$ and 0.5 . The inset shows the appearance of the in-plane anisotropy at T_0 .

Since the magnetic anisotropy reflects the structural symmetry [22], the appearance of the two-fold symmetry below T_0 is ascribable to a struc-

tural transition from a high-temperature tetragonal to a low-temperature orthorhombic phase. We measured the in-plane azimuthal dependence of the susceptibility at various temperatures also for $x = 0.3, 0.4, 0.5$ and 0.7 . The two-fold symmetry was found only in region II. From the $R(T)$ plots shown in Fig. 3.17, we determined T_O as 220 K for $x = 0.3$, 150 K for 0.4 , and below 1.8 K for 0.5 and 0.7 . Plotting the variation of T_O in the phase diagram of Fig. 2.1, we notice that the T_O line crosses room temperature around $x = 0.2$. Quite consistently, it is at this point where the structural transition was detected by the X-ray diffraction measurement. In addition to the strong shrinkage of the c -axis shown in Fig. 3.15, the a and b -axes start to elongate and split in region I. Therefore, we conclude that across the T_O line, a structural transition occurs from a tetragonal phase in the Sr-rich and high-temperature region to an orthorhombic phase in the Ca-rich and low-temperature region, involving the lattice flattening.

This transition is also detected as kinks in the resistivity data $\rho_{ab}(T)$ and $\rho_c(T)$ (see Fig. 3.31 for $\rho_{ab}(T)$ of $x = 0.2$ and the inset of Fig. 3.32 (a) for $\rho_c(T)$ of $x = 0.2$ and 0.4). The absence of the thermal hysteresis at these kinks suggests that this transition should be of the second-order. The decrease of $\rho_c(T)$ and increase of $\rho_{ab}(T)$ below T_O are consistent with the lattice flattening. This will weaken the hybridization between the in-plane Ru $4d$ orbitals, while supporting coherent hopping between layers.

Neutron powder diffraction measurements have recently been performed for samples with $x = 0.1, 0.2, 0.5$ and 1.0 [13]. The results confirm that the second-order structural transition from a high-temperature tetragonal to a low-temperature orthorhombic phase occurs at T_O , inducing the lattice flattening owing to orthorhombic deformation of RuO₆ octahedra as well as their tilting. Details of the results are described in [13].

Another important point is that T_O decreases with x and finally goes down to zero at $x = 0.5$ as in Fig. 2.1. This suggests that $x_c \simeq 0.5$ should be the instability point at absolute zero, in other words, the quantum critical point of the second-order structural transition.

3.4 Ferromagnetic instability at $x_c \simeq 0.5$

3.4.1 Evolution of the temperature dependence of the susceptibility

Curie-Weiss Analysis

In the entire metallic region, the $\chi(T)$ curve shows a systematic variation with x . We define the susceptibility $\chi \equiv M/H$ at low enough fields (up to 1 T) where the magnetization M shows linear dependence on the field H . In Fig. 3.18(a) and (b), we display the in-plane $\chi_{ab}(T)$ curves for single crystalline samples in region II and III, respectively. The inverse susceptibilities measured up to 700 K for polycrystalline samples in region II and III are also given in the insets of Fig. 3.18 (a) and Fig. 3.18 (b), respectively.

In order to clarify the evolution of the temperature dependence, we performed the Curie-Weiss (C-W) analysis, as usually done for an itinerant electron system with spin fluctuations. As shown by band calculations [19], the states at the Fermi level (E_F) in Sr_2RuO_4 are mainly composed of $4d$ t_{2g} bands. Basically, this configuration should not change throughout the system, and thus the *itinerant* t_{2g} spins are responsible for the dominating C-W term.

The analyses were made in a high-temperature fitting (HT) region: 300-700 K for polycrystalline samples, and in a low-temperature fitting (LT) region: 50-330 K for both polycrystalline and single crystalline samples. For the samples in region II, we restricted the LT region within the orthorhombic phase from 50 K to $T_O - 20$ K. Since Ca_2RuO_4 exhibits a first-order structural transition around 350 K [13, 14], we performed the fitting for HT region between 380 and 700 K. We adopted the fitting formula as

$$\chi = \chi_0 + \frac{C}{T - \Theta_W}. \quad (3.6)$$

Here, χ_0 is a temperature independent term, C is the Curie constant and Θ_W is the Weiss temperature. The effective Bohr magneton p_{eff} was derived from the formula:

$$C = \frac{N_A p_{\text{eff}}^2 \mu_B^2}{3k_B}, \quad (3.7)$$

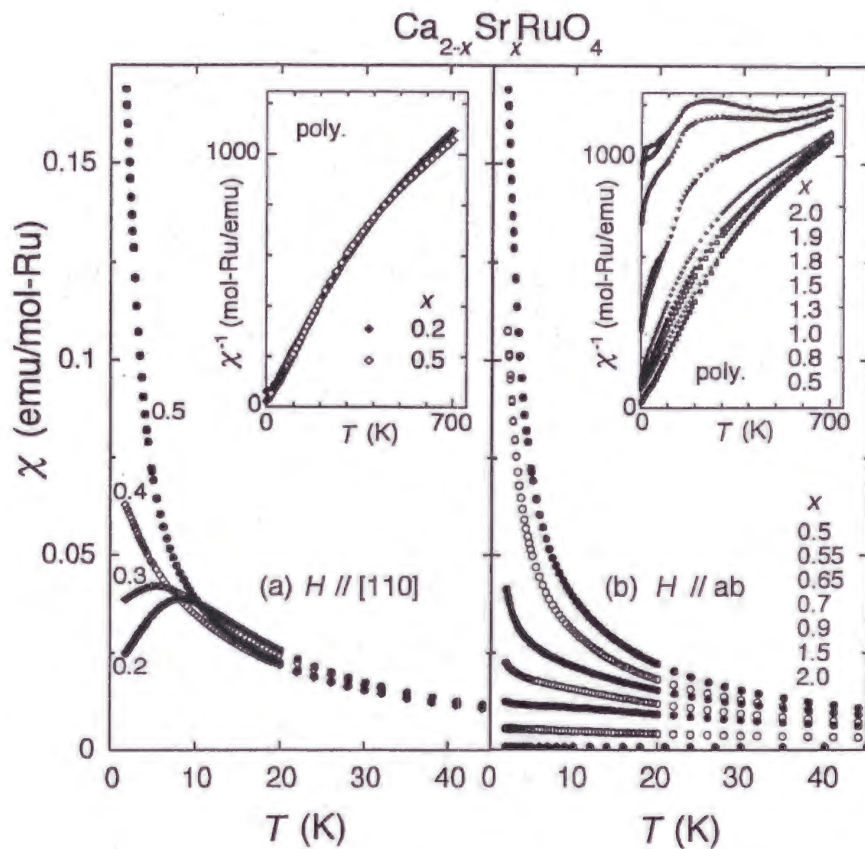


Figure 3.18: Temperature dependence of the in-plane susceptibility for $\text{Ca}_{2-x}\text{Sr}_x\text{RuO}_4$ with different values of x (a) in region II for the $[110]$ component and (b) in region III. For both regions, zero-field-cooled (ZFC) and field-cooled (FC) curves agree very well. The insets for (a) and (b) display the inverse susceptibility of polycrystalline samples in regions II and III, respectively. For polycrystalline samples only around $x = 2.0$, the difference between the ZFC and FC curves can be seen at low temperatures. This is probably due to a small inclusion ($< 0.04\%$) of ferromagnetic impurity $\text{Ca}_{1-x}\text{Sr}_x\text{RuO}_3$.

where N_A , μ_B and k_B are Avogadro's number, Bohr magneton and Boltzmann's constant. For $x = 1.9$ and 2 , the fitting was not successful because χ is almost constant up to 700 K. p_{eff} can be related with the effective spin S_{eff} by the formula:

$$p_{\text{eff}} = 2\sqrt{S_{\text{eff}}(S_{\text{eff}} + 1)}, \quad (3.8)$$

χ_0 consists of temperature independent spin susceptibility, diamagnetic susceptibility and orbital susceptibility. The diamagnetic and orbital susceptibilities are -0.91×10^{-4} emu/mol-Ru and 1.8×10^{-4} emu/mol-Ru for Sr_2RuO_4 ($x = 2$) [23], which are expected to keep the same order of magnitude with the Ca substitution. Actually throughout this system, χ_0 has values only of the order of 10^{-4} emu/mol-Ru and just slightly decreases with the Ca substitution as the temperature dependence of the spin susceptibility becomes significant. As a result, χ_0 is negligible in comparison with the low temperature susceptibility $\chi(0)$ at 1.8 K, except around $x = 2$ [8]. Hence, we will focus on the fitting results of p_{eff} and Θ_W , which are summarized in Fig. 3.19(a) and (b), respectively.

Figure 3.19(a) shows a systematic x dependence of p_{eff} . First, Ca_2RuO_4 ($x = 0$) has the largest p_{eff} with almost 80% of the expected value for $S = 1$ configuration. Here, C-W term comes from the localized spins. As the system goes away from the insulating phase, p_{eff} decreases rapidly in region I and finally becomes almost constant in the region $0.2 \leq x \leq 1.5$. Quite interestingly, the results in this region, especially the HT results for polycrystalline samples (solid circles), are close to the value corresponding to localized $S = 1/2$ spin. Given the Hund's coupling in the t_{2g} band, $S = 1$ configuration is naturally expected. In addition to being a metal, the enhanced spin fluctuations due to the structural two-dimensionality and the orbital degree of freedom are probably responsible for the reduced p_{eff} . However, this mechanism alone does not explain why the effective S remains close to $1/2$.

According to the conventional analysis for localized spins, positive and negative values of Θ_W indicate the strength of ferromagnetic and antiferromagnetic interactions, respectively. While for Ca_2RuO_4 , this rule works well

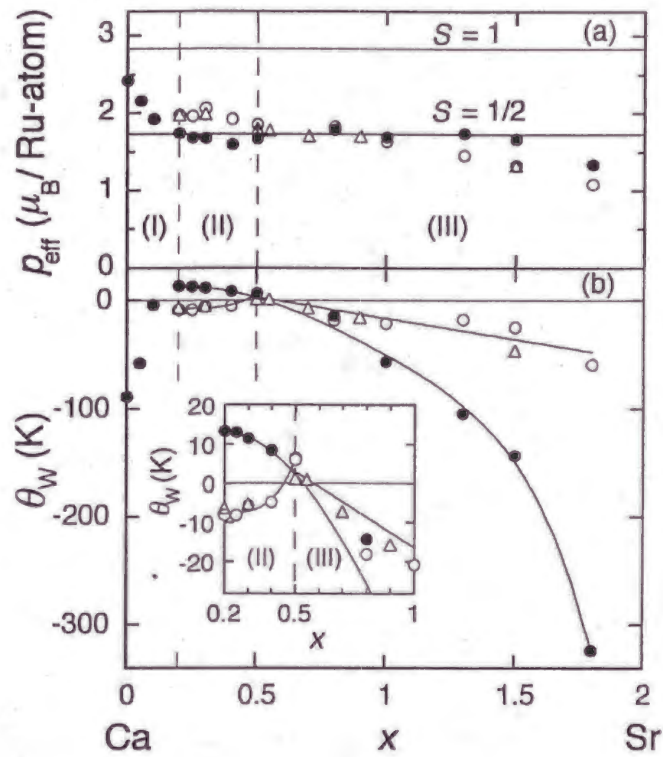


Figure 3.19: Curie-Weiss parameters against the Sr content x in $\text{Ca}_{2-x}\text{Sr}_x\text{RuO}_4$. The solid and open circles correspond to the results of polycrystalline samples for the high temperature and the low temperature fitting regions, respectively. The open triangles represent the low temperature fitting results of single crystals for the ab -plane component in region III and $[1\bar{1}0]$ component in region II. In the panel (a), the solid horizontal lines correspond to the effective Bohr magnetons with $S = 1/2$ and 1. The inset in the panel (b) is an enlarged figure for region II. The solid curves are guides to the eye.

and $\Theta_W \simeq 90$ K has the same order of magnitude as its Néel point $T_N = 110$ K, slight Ca substitution reduces the absolute value of Θ_W much faster than that of T_N . However, the increase of negative Θ_W toward zero with increasing x is still qualitatively consistent with the decrease of AF coupling of the order of T_N in region I.

In region III, Θ_W for both HT and LT regions also has negative values, but increases with decreasing x . LT results for single crystals (open triangles) are consistent with those for polycrystalline samples (open circles). In general, a fairly large value of Θ_W is necessary to reproduce almost temperature-independent behavior by Eq. (3.6). Accordingly, near the Pauli paramagnetic Sr_2RuO_4 , Θ_W has a large negative value, and owing to the evolution of Curie-Weiss behavior the magnitude decreases rapidly with the Ca substitution. Thus, the negative value of Θ_W in this region does not indicate the strength of AF coupling. Alternatively, according to the Self-Consistent Renormalization (SCR) theory [24], this increase in negative Θ_W to zero can be well understood as the result of the evolution of FM spin fluctuations. The band narrowing due to the Ca substitution must be the main cause of this FM coupling, as we will discuss in Sec. 4.2.2.

Here, it is also important to stress that both HT and LT results show qualitatively the same feature that the negative Θ_W increases toward zero with the Ca substitution. Furthermore, they finally coincide around $x = 0.8$ and approaches zero together near $x = 0.5$. In fact, as in Fig. 3.20, the temperature dependence of the inverse in-plane susceptibility for $x = 0.5$ shows almost T -linear Curie behavior in a wide range of temperature.

Once the system enters region II, however, Θ_W for each fitting region starts to show definitely different x dependence, as shown in the inset of Fig. 3.19(b). While the result for $T > T_O$ (solid circles) increases continuously on the extended track from region III, Θ_W for $T < T_O$ of both polycrystalline samples (open circles) and $[1\bar{1}0]$ component of single crystalline samples (open triangles) stops increasing at $x = 0.5$ and starts to decrease in region II. Notably, Θ_W for $T < T_O$ has a negative value with the same order of magnitude as T_P , the peak temperature in $\chi(T)$. This sign reversal of Θ_W across T_O indicates that *the structural transition induces a change of*

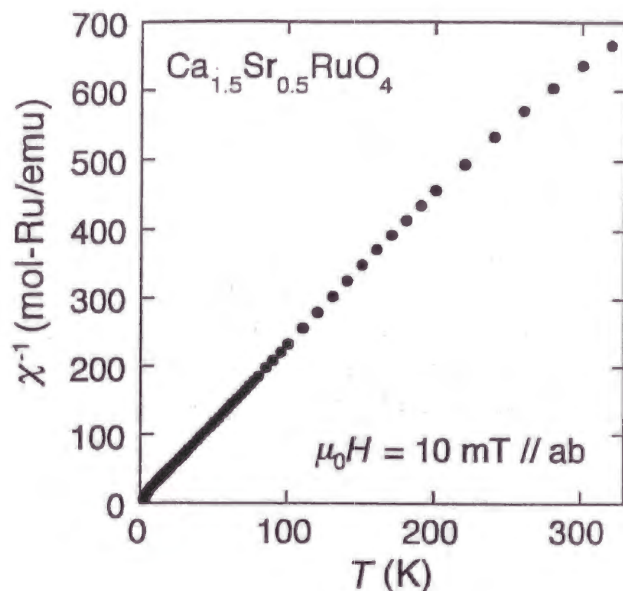


Figure 3.20: Temperature dependence of the inverse in-plane susceptibility $\chi_{ab}^{-1}(T)$ for $x = 0.5$ under a field of 100 G.

magnetic coupling.

Divergence of the low temperature susceptibility

In the ground state, this change of magnetic coupling becomes evident: the low temperature susceptibility $\chi(0)$, represented here by the value at 2 K reveals intriguing systematic variation in the *metallic* regions II and III, as presented in Fig. 3.21. Corresponding to the evolution of the C-W behavior, $\chi(0)$ for $2.0 \geq x \geq 0.5$ increases with decreasing x . It is critically enhanced at $x = 0.5$, reaching a value more than 100 times larger than that of Sr_2RuO_4 . In the region II, on the other hand, $\chi(0)$ sharply decreases with decreasing x , reflecting the formation of the susceptibility peak at the higher temperature T_P as shown in Fig. 2.1.

We note that this critical enhancement of $\chi(0)$ occurs at $x_c = 0.5$, and thus appears to be correlated with Θ_W approaching zero in the region III and T_P increasing from zero in the region II. This criticality indicates a drastic change of the ground state at the structural instability. The continuous increase of the HT result of Θ_W across $x = 0.5$ implies that without the structural transition, $\chi(0)$ would keep diverging with decreasing x . Therefore, the critical point at $x_c \simeq 0.5$ should be very close to a FM instability. In fact, almost singularly at $x = 0.5$, we have found a FM ordering at very

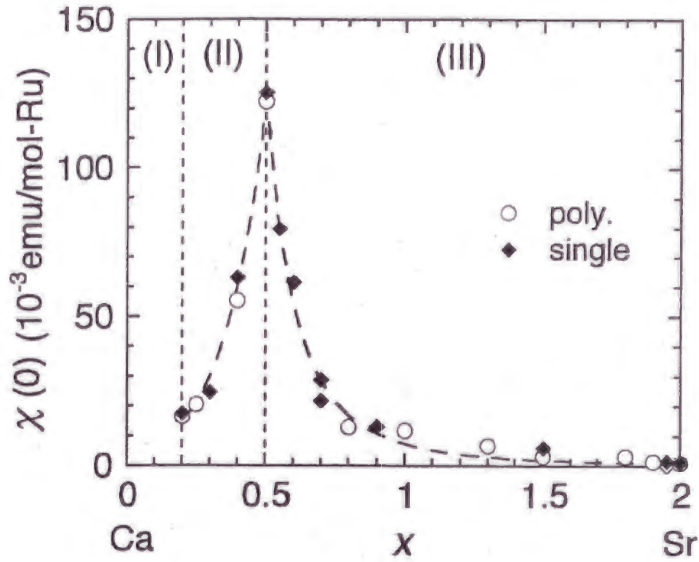


Figure 3.21: $\chi(0)$: the susceptibility at 2.0 K against the Sr concentration x in the metallic regions II and III. The values for the polycrystalline samples are indicated by open circles, while for the single crystals, the solid diamonds represent the mean values $\chi_m(0)$ determined by the relation: $\chi_m(0) = \{\chi_a(0) + \chi_b(0) + \chi_c(0)\}/3$. The broken lines are guides to the eye.

low temperatures around 0.5 K, as we describe in Sec. 3.4.4. In the M-M region, however, the AF correlation rapidly evolves with the Ca substitution toward the Mott transition. Here, the negative Θ_W as well as T_P must be the indicator of the strength of the AF coupling. Thus, it is natural to consider that the structural transition halts the growth of the FM coupling and switches on the AF coupling.

3.4.2 Non-Fermi-liquid behavior of resistivity

The low temperature parts of $\rho_{ab}(T)$ in Fig. 3.7 for $x = 0.2, 0.5$ and 2 are presented in Fig. 3.22, where $\rho_{ab}(T) - \rho_{ab}(0)$ is plotted against $T^{1.4}$. Sr_2RuO_4 shows T -squared dependence as indicated by a fitting curve, reflecting its Fermi liquid state established by a variety of measurements [4, 5]. In contrast, for $x = 0.2$ and 0.5, the in-plane resistivities severely deviate from the T -squared dependence. In order to clarify the temperature dependence at low temperatures, we performed a fitting with a formula: $\rho_{ab}(T) = \rho_{ab}(0) + AT^n$. Here, $\rho_{ab}(0)$, A and n are fitting parameters. The best fit was obtained in the form of $\rho_{ab}(T) = \rho_{ab}(0) + AT^{1.4}$. At $x = 0.5$, this $T^{1.4}$ dependence appears

up to 3 K followed by T -linear one up to 5.5 K. Meanwhile, the resistivity for $x = 0.2$ starts to decrease strongly below about $T_P^{[110]} \approx 8$ K and shows the $T^{1.4}$ dependence toward the lowest temperature.

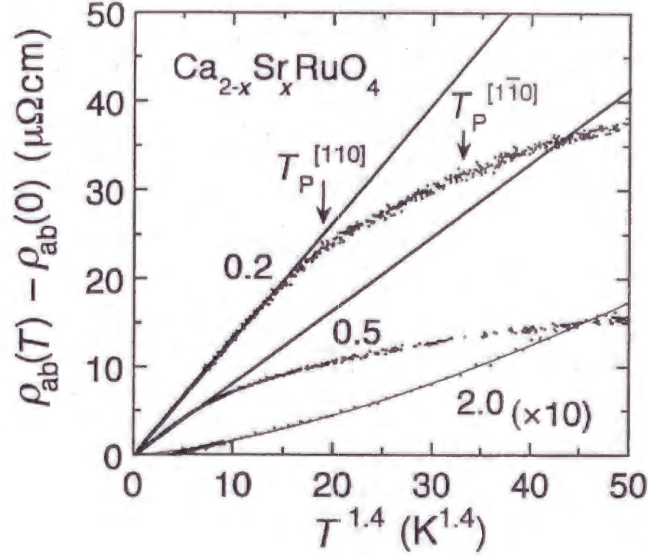


Figure 3.22: Temperature dependence of the in-plane resistivity $\rho_{ab}(T)$ for $x = 0.2, 0.5$ and 2 . Solid lines indicate fits with T^2 ($x = 2$), and $T^{1.4}$ ($x = 0.2$ and 0.5) dependence. The peak temperatures of the susceptibilities are indicated for $x = 0.2$.

Works on heavy fermion compounds and cuprates have revealed that such NFL behavior is due to critical fluctuations, and persists to low temperature near a magnetic instability [25, 26]. Therefore, the non-Fermi-liquid (NFL) behavior observed down to 0.3 K not only around $x_c \simeq 0.5$ but at $x = 0.2$ suggests that the enhanced spin fluctuations, which destabilize the magnetic LRO, dominates the entire M-M region. In a two-dimensional system near AF and FM instabilities, the resistivity is expected to show T -linear [27] and $T^{4/3}$ [28] dependence, respectively. The observed $T^{1.4}$ -dependence is quite close to the latter one, which is also found in Sr_2RuO_4 under pressure [29]. Along with the strong enhancement of the low temperature susceptibility, this gives a consistent interpretation that $x_c \simeq 0.5$ is just near a FM instability. On the other hand, for the AF-SRO in the M-M region, there are basically

two possible spin configurations: simple in-plane AF or interlayer AF with the dominant in-plane FM spin fluctuations. It is not possible to distinguish between these possibilities on the basis of the current data. Further studies by neutron diffuse scattering are needed for this region.

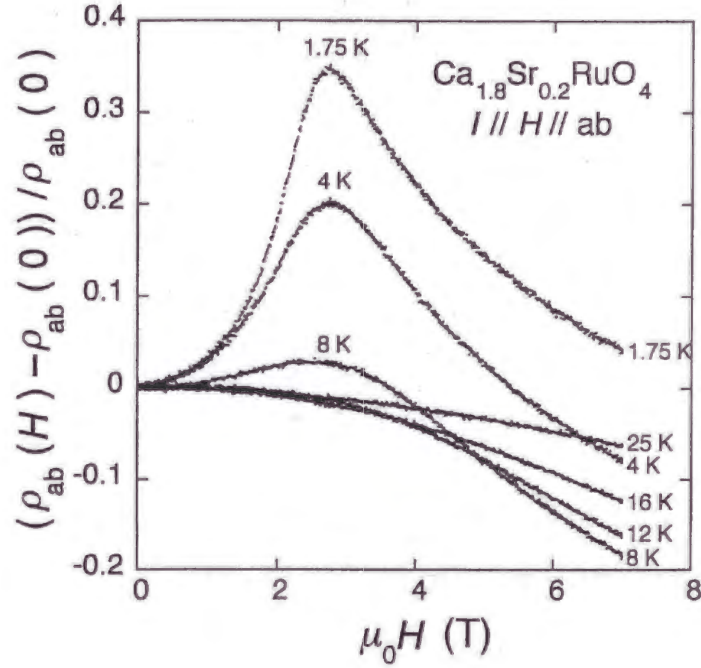


Figure 3.23: Longitudinal in-plane magnetoresistance ($I \parallel H \parallel ab$) for $x = 0.2$ at various temperatures.

In Fig. 3.22, it should also be noted that $\rho_{ab}(T) - \rho_{ab}(0)$ becomes smaller with x . This most probably results from the weakened inelastic (especially, spin) scattering due to the band widening. Moreover, for $x = 0.2$ below T_P , the formation of AF-SRO should induce the strong decrease in $\rho_{ab}(T)$ because of the reduced spin scattering. In fact, well below T_P , the field dependence of the longitudinal in-plane magnetoresistance ($I \parallel H \parallel ab$) for $x = 0.2$ (Fig. 3.23) shows a clear peak at $\mu_0 H \approx 2.8$ T, corresponding to the metamagnetic transition, while only a negative dependence was observed above T_P .

3.4.3 Evolution of the temperature dependence of the specific heat

Critical enhancement in $\gamma(T)$

As described in Sec. 3.4.1, the temperature dependence of the susceptibility evolves systematically with the Ca substitution. Likewise, the temperature dependence of C_e/T in Fig. 3.12 shows continuous and critical enhancement in the region III. As for Sr_2RuO_4 , it exhibits a jump in C_e/T at the superconducting transition temperature $T_c \simeq 1.5$ K. Reflecting its Fermi liquid ground state, the C_e/T above T_c is almost constant up to around 12 K. This situation is clearer in the data for $x = 1.95$, which manifests temperature independent C_e/T without any transition down to the lowest temperature 0.4 K. The spin-triplet superconductivity is extremely sensitive to impurities: several hundred ppm is enough to kill the superconductivity [30]. For Sr-site impurities of Ca, the present study indicates that at least 2.5% substitution is enough to suppress the transition. Further study is still needed to characterize how rapidly the transition temperature changes with the Ca substitution.

With decreasing the Sr content x from Sr_2RuO_4 , C_e/T and its temperature dependence gradually increases as in Fig. 3.12. While C_e/T at $x = 1.5$ is still almost temperature independent below about 5 K, those for $x = 0.9$ and 0.7 exhibit significant increase of C_e/T on cooling down to the lowest temperature 0.4 K. Moreover, C_e/T for $x = 0.5$ enhances the most steeply, although it forms a cusp below about 1 K. We will discuss its origin in Sec. 3.4.4. In order to clarify the systematic evolution of the temperature dependence, we plot C_e/T against $T^{1/2}$ in Fig. 3.24. Although C_e/T for $x = 2.0$, 1.95 and 1.5 is almost constant at low temperatures, those for $x = 0.9$, 0.7 and 0.5 increase linearly with $-T^{1/2}$ down to low temperature.

This non-Fermi-liquid behavior must be correlated with that observed in the low temperature resistivity discussed in the previous section and should be regarded as critical behavior most likely of ferromagnetism. Furthermore, the temperature dependence of the entropy in Fig. 3.13 is also consistent with this picture. As a system goes closer to a magnetic instability, the char-

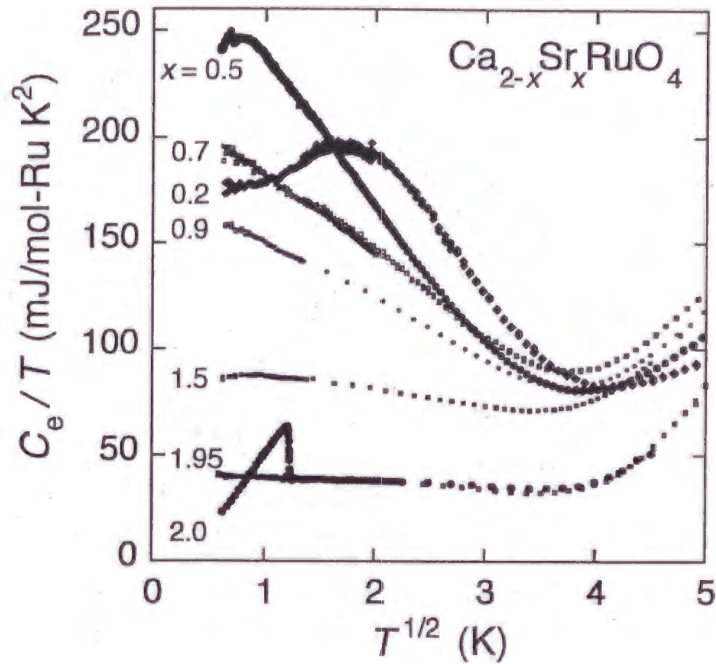


Figure 3.24: Electronic part of the specific heat C_e/T against $T^{1/2}$ for the metallic region II and III of $\text{Ca}_{2-x}\text{Sr}_x\text{RuO}_4$

acteristic energy of the spin fluctuation decreases, and thereby the entropy due to the spin degree of freedom increases at low temperatures. This should explain the continuous enhancement of the low temperature entropy in Fig. 3.13 with decreasing x . As this system enters the M-M region, however, the C_e/T starts to form a peak in its temperature dependence, as also discussed in Sec. 3.2.3. This is presumably the result of the crossover of magnetic coupling from FM to AF in the M-M region.

Wilson ratio

As we can see in Fig. 3.12, C_e/T in region III shows a large enhancement with the Ca substitution as well as on cooling. This systematic change is well summarized in Figure 3.25 which displays the $\gamma \equiv C_e/T (0.4 \text{ K})$ against the Sr content x . While Sr_2RuO_4 itself has a large value about 37 mJ/mol K^2 , γ increases significantly by the Ca substitution and it finally reaches the maximum of about $250 \text{ mJ/mol-Ru K}^2$ at $x = 0.5$. To our knowledge, this

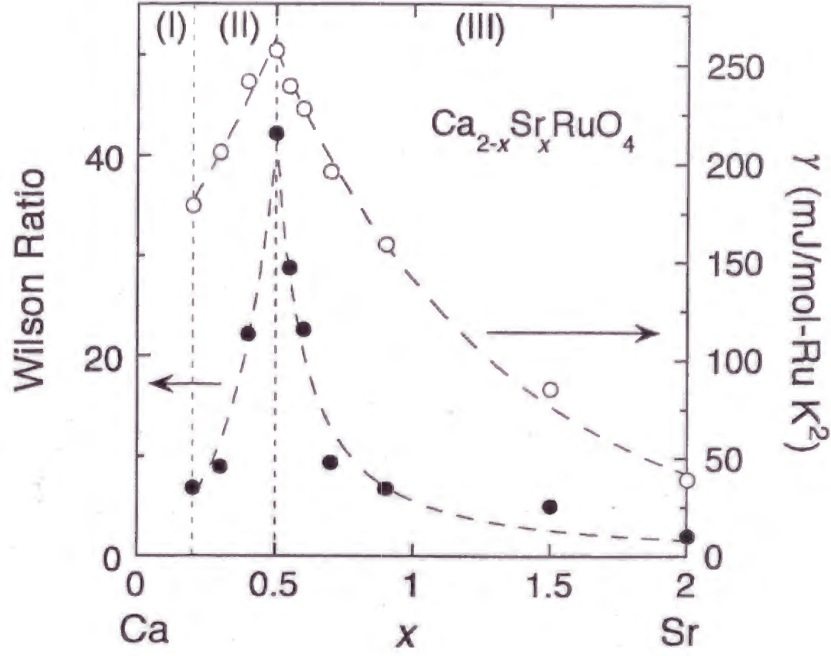


Figure 3.25: x dependence of the electronic specific heat coefficient γ at 0.4 K (open circle, right axis) and Wilson ratio (solid circle, left axis) for single crystalline $\text{Ca}_{2-x}\text{Sr}_x\text{RuO}_4$. The broken lines are guides to the eye.

value of $\gamma \simeq 250 \text{ mJ/mol-Ru K}^2$ is the largest among those for the transition metal oxides, and surpasses $\gamma \simeq 210 \text{ mJ/mol-V K}^2$ for LiV_2O_4 , which is known as a heavy-fermion transition-metal oxide [31]. Taking account of the fact that the ferromagnetic instability as well as structural instability exists just near $x = 0.5$, the large γ value at this point should be attributed to the critical enhancement due to both the ferromagnetic spin fluctuations and the electron-phonon interaction.

While γ decreases with the Ca substitution in the M-M region, reflecting the formation of the peak in the temperature dependence of C_e/T , it is significant that the system still maintains a large value around 200 mJ/mol K^2 even at around the M/NM transition point around $x = 0.2$. This is attributable to the electron-electron correlation enhanced near the Mott transition.

A well-defined measure to characterize the enhancement by the correlation effect is the Wilson ratio, which is defined by

$$R_W = \frac{\pi^2 k_B^2 \chi(0)}{g^2 \mu_B^2 \gamma S(S+1)} \quad (3.9)$$

This ratio is scaled to be unity for a non-interacting Fermi gas, and the change in the ratio reflects the electron correlation in the system. The electron-phonon interaction enhances γ , but not $\chi(0)$ and reduces R_W . The electron-electron correlation enhances the R_W to 2, as calculated for a Kondo system [32]. The enhancement beyond that is usually attributed to ferromagnetic spin correlation with additionally enhanced $\chi(0)$, and in fact observed in a series of nearly FM systems [33]. Although the ground state of $\text{Ca}_{2-x}\text{Sr}_x\text{RuO}_4$ may not be a Fermi liquid around $x = 0.5$, R_W is still a well-defined experimental measure to clarify how the electron correlation evolves from the Fermi liquid Sr_2RuO_4 with the Ca substitution.

Figure 3.25 illustrates the x dependence of the R_W calculated by Eq. (3.9). Here, $\chi(0)$ and γ in the equation are the lowest temperature values measured, that is, the susceptibility at 1.8 K in Fig. 3.21 and the γ at 0.4 K in Fig. 3.25. S is fixed to $1/2$ according to the result of Curie-Weiss fitting in Sec. 3.4.1. While R_W for Sr_2RuO_4 is 1.7 corresponding to its strongly correlated Fermi liquid ground state, R_W first increases gradually with the Ca substitution and then reveals critical divergence at $x = 0.5$ to reach the value more than 40. $R_W \approx 40$ is so large that it well surpasses those known for the other well-studied nearly FM materials, such as $R_W = 5.8$ for Pd, 5.4 for Ni_3Ga , and 12 for TiBe_2 [33]. This strongly suggests that the Ca substitution enhances the ferromagnetic coupling in Sr_2RuO_4 to leads to the nearly FM state near $x = 0.5$. Once the system goes beyond $x = 0.5$ into the M-M region, however, R_W decreases rapidly and finally down to 7 at $x = 0.2$ just near the M/NM transition. The crossover of the magnetic coupling to AF should result in this decrease of R_W .

As a result, the Wilson ratio exhibits a prominent criticality, which indicates the critical relation between $\chi(0)$ and γ . In fact, the γ vs $-\ln \chi(0)$ in Fig. 3.26 manifests that the relation $\gamma \propto -\ln \chi(0)$ roughly holds not only in region III (solid circles) but in region II (open circles). This critical relation is expected to hold in a system dominated by three-dimensional FM fluctuations [28, 34]. We also checked the relation $\gamma \propto \chi(0)^{1/2}$ expected for two-dimensional FM fluctuations as in Fig. 3.27, but it holds only in rather narrow range near $x = 0.5$.

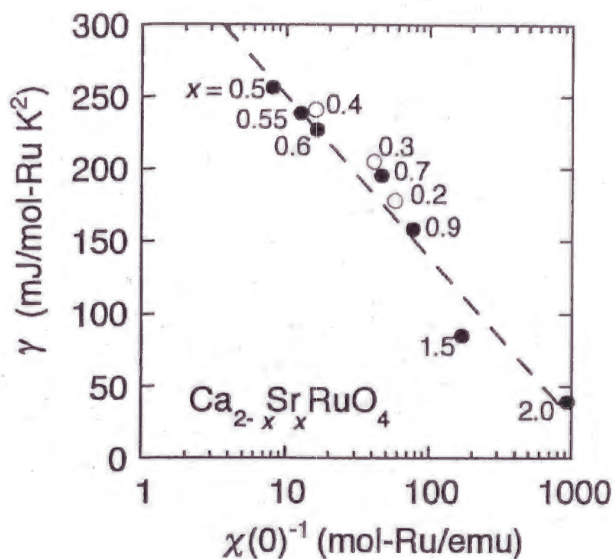


Figure 3.26: $\chi(0)$ vs $\ln \chi(0)$ for region II (open circles) and region III (solid circles) of single crystalline $\text{Ca}_{2-x}\text{Sr}_x\text{RuO}_4$. The broken line is a guide to the eye.

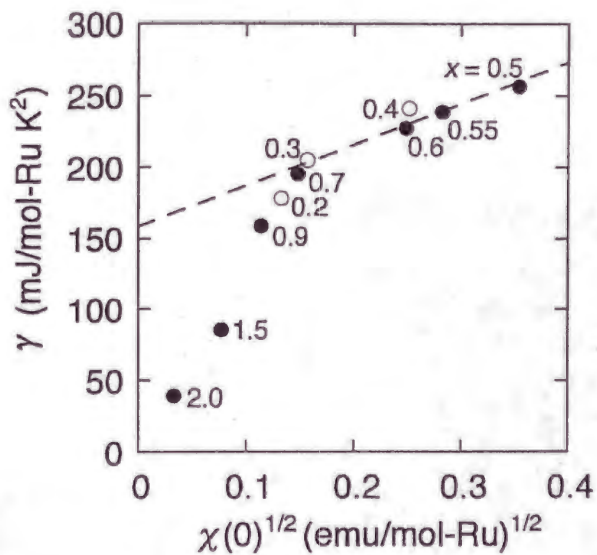


Figure 3.27: γ vs $\chi(0)^{1/2}$ for single crystalline $\text{Ca}_{2-x}\text{Sr}_x\text{RuO}_4$. The broken line is a guide to the eye.

Another criticality we should note here is the temperature dependence of C_e/T . As we discussed above, it decrease proportionally to $-T^{1/2}$ on heating near $x = 0.5$. According to the SCR theory [28], this type of critical behavior is expected near the quantum critical point (QCP) of three-dimensional (3D) AF ordering. (Around the QCPs of 2D and 3D FM ordering, C_e/T is expected to follow $T^{-1/3}$ and $-\ln T$ dependence, respectively [28].) However, it is clear that the three-dimensional AF fluctuations is irrelevant for this system, since the fluctuation localized at finite Q cannot make such a significant enhancement of $\chi(0)$ as in Fig. 3.21, the $Q = 0$ component of the susceptibility.

To summarize, we have observed the following critical behavior around $x = 0.5$;

1. Curie-like temperature dependence of $\chi(T)$ at $x = 0.5$ (Fig. 3.20)
2. Critical enhancement in $\chi(0)$ (Fig. 3.21)
3. Non-Fermi-liquid behavior in the in-plane resistivity: $\rho_{ab}(T) = \rho_{ab}(0) + AT^{1.4}$ (Fig. 3.22)
4. Critical enhancement in the Wilson ratio (Fig. 3.25)
5. The relation $\gamma \propto -\ln \chi(0)$ in all the metallic region (Fig. 3.26)

Although there is some uncertainty on the dimensionality of the fluctuations, we conclude that *the ferromagnetic spin fluctuations dominate in this system around the almost ferromagnetic state at $x = 0.5$.*

3.4.4 Observation of itinerant ferromagnetism at $x = 0.5$

We have shown in Sec. 3.3 that $x_c \simeq 0.5$ is the QCP of structural phase transition. However, these observations of the magnetic critical behavior centered at $x = 0.5$ strongly implies that the QCP for a ferromagnetic ordering also exists around this point. Despite this expectation, we could not find any clue of the magnetic long-range order inside the M-M region. However,

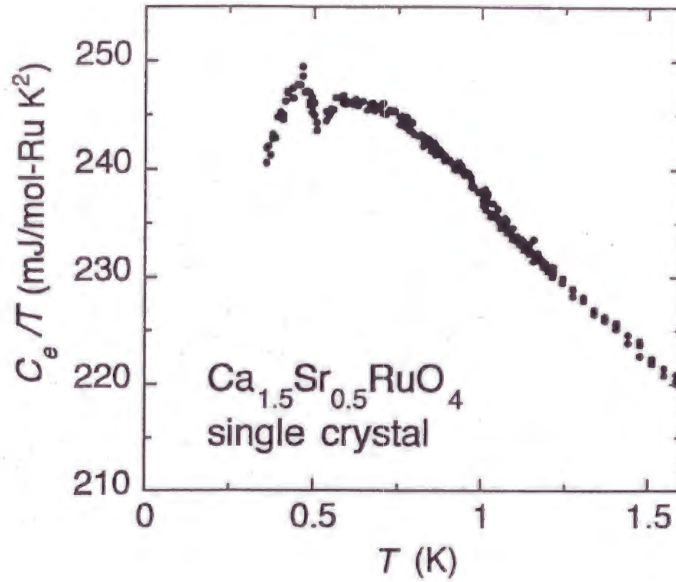


Figure 3.28: Low temperature C_e/T for single crystalline $\text{Ca}_{1.5}\text{Sr}_{0.5}\text{RuO}_4$

marginally at the edge of the M-M region at $x = 0.5$, we have indeed succeeded in obtaining clear pieces of the evidence for a ferromagnetic ordering.

One is the low temperature anomaly in the C_e/T for $x = 0.5$, as presented in Fig. 3.12. Although the $T^{1/2}$ dependence is observed down to the lowest temperature 0.4 K for $x = 0.7$ and 0.9, the C_e/T for $x = 0.5$ shows a cusp below about 1 K, following $-T^{1/2}$ dependence between 1 and 6 K. To look into the detail, we enlarge the low temperature part of C_e/T for $x = 0.5$ in Fig. 3.28. It clarifies a broad peak around 0.8 K, and moreover a small yet definite jump of C_e/T at 0.5 K, which demonstrates the presence of a phase transition.

In order to clarify the magnetic nature of this transition, we have constructed a low temperature magnetometer, using a commercial dc Superconducting QUantum Interface Device (SQUID) 'Tristan Technology dc-SQUID iMC303'. The schematic view of this system is shown in Fig. 3.29. A SQUID probe is mounted on a vacuum can of a commercial ^3He refrigerator 'Oxford Instruments Heliox 2VL' and immersed in ^4He liquid. Superconducting leads are introduced into the vacuum can through both a feedthrough and a tube

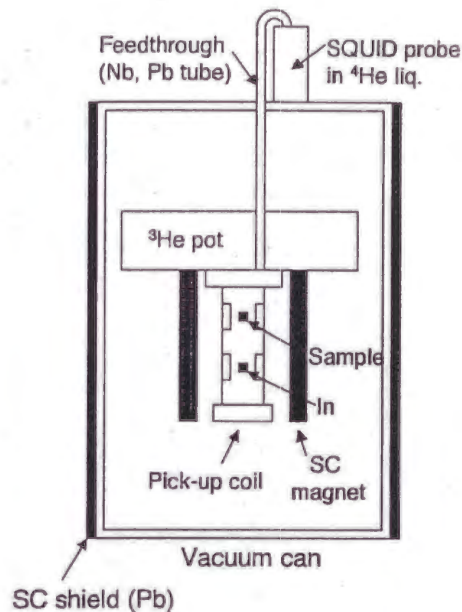


Figure 3.29: Schematic view of the low temperature dc SQUID magnetometer mounted on a ^3He refrigerator

made of either superconductor Nb or Pb. The outside surface of the vacuum can is also surrounded by Pb tube for superconducting shield. A pick-up coil is attached on a ^3He pot, which can be cooled down to 0.26 K. (The typical size of the pick-up coil is 5 mm in diameter and 1.2 mm in length.) A sample and a pure In are located at the centers of the canceling coils and are thermally connected to the ^3He pot, using copper wires. (The sizes of the sample and In that we used are about $3 \times 1 \times 0.2 \text{ mm}^3$ and $1 \times 1 \times 0.1 \text{ mm}^3$, respectively.) The output voltage of the SQUID is calibrated by the voltage jump at the superconducting transition of In. Magnetic fields up to 6 mT are applied to the sample and In by a superconducting excitation coil outside the pick-up coil. The sensitivity of this system is estimated to be of the order of 10^{-8} emu. This system can determine only the magnitude of the susceptibility change during a sequence of temperature sweep, because the initial number of flux trapped in the SQUID coil is not unique. Therefore, in order to obtain the absolute value, we utilize the result measured by the

commercial SQUID magnetometer 'Quantum Design MPMS-5' down to 1.8 K.

Figure 3.30 shows the low temperature susceptibility for $\text{Ca}_{1.5}\text{Sr}_{0.5}\text{RuO}_4$. The result measured by this dc SQUID magnetometer (solid line) is smoothly connected to the high temperature result (open circles) in Fig. 3.18 obtained by the commercial SQUID magnetometer. Both field-cooled (FC) and zero-field-cooled (ZFC) data are taken on heating under a field of 0.5 mT parallel to the *ab*-plane. A slight deviation between FC and ZFC curves starts below a kink temperature at 1.1 K. However, below 0.5 K, at which the specific heat jump occurs, the deviation becomes much clearer toward the lowest temperature 0.3 K. This observation confirms that a ferromagnetic ordering occurs at around 0.5 K.

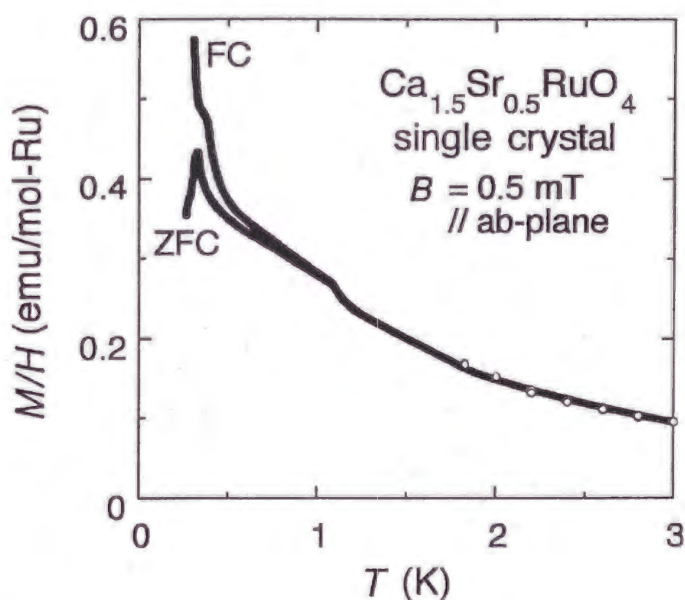


Figure 3.30: Low temperature susceptibility for single crystalline $\text{Ca}_{1.5}\text{Sr}_{0.5}\text{RuO}_4$ under a field of 0.5 mT parallel to the *ab*-plane. Clear deviation between the field-cooled (FC) and zero-field-cooled (ZFC) data can be seen.

On the other hands, the jump in C_e/T is quite small compared with that for the superconductivity of Sr_2RuO_4 , as can be seen in Fig. 3.12. This implies that the size of the spins involved in this magnetic transition be sig-

nificantly reduced, most likely owing to enhanced pin-fluctuations. In this sense, the broad peak around 1 K observed in C_e/T can be considered as a result of the well-developed short-range order above the transition temperature. This may also be related to the appearance of the small kink in the susceptibility even above the transition temperature.

This ferromagnetism is quite marginal in the sense of its low transition temperature and possible singularity in the phase diagram. Further study of this ordering is important to determine its precise boundary in the phase diagram and to clarify the origin of the unusual anomalies above the transition temperature. Regardless of the details, the appearance of this 'marginal' ferromagnetism just near the structural instability stands alone as one of the most intriguing features in this system.

3.5 Anisotropic transport properties

Reflecting the quasi-two-dimensional structure, the temperature dependence of the resistivity $\rho(T)$ is quite anisotropic. Figure 3.31 presents the temperature dependent part of the in-plane resistivity: $\rho_{ab}(T) - \rho_{ab}(0)$ measured down to 0.3 K for various values of $x \geq 0.2$. All curves show metallic behavior (i.e. $d\rho/dT > 0$). In fact, at low temperatures, $\rho_{ab}(T)$ are less than the Mott-Ioffe-Regel (MIR) limit of metallic conduction of about $200 \mu\Omega\text{cm}$ for Sr_2RuO_4 [35], which suggests the coherent metallic transport within the plane. As can be seen in Fig. 3.31, $\rho_{ab}(T) - \rho_{ab}(0)$ increases quite systematically with the Ca substitution. Because the temperature dependent term is basically determined by inelastic scattering, which becomes severe for a narrow band metal with high $N(E_F)$, this increase is consistent with the band narrowing with the Ca substitution. In addition, $\rho_{ab}(T) - \rho_{ab}(0)$ for $x = 0.2$ shows a steep decrease below $T_P \simeq 12$ K. This should come from the reduction of the spin scattering by the formation of the AF short-range order in the M-M region, as we discussed in Sec. 3.4.2.

The x dependence of the residual resistivity $\rho_{ab}(0)$ is presented in the inset of Fig. 3.31. In contrast with the continuous increase of $\rho_{ab}(T) - \rho_{ab}(0)$, $\rho_{ab}(0)$ has a peak around $x = 1.0$, which is qualitatively consistent with

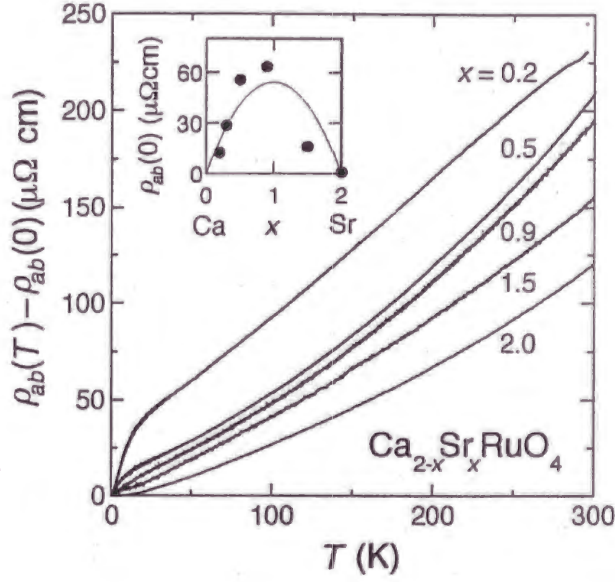


Figure 3.31: Temperature dependence of the in-plane resistivity $\rho_{ab}(T)$ for $\text{Ca}_{2-x}\text{Sr}_x\text{RuO}_4$ with different values of x . The inset shows the x dependence of the in-plane residual resistivity $\rho_{ab}(0)$. The solid curve represents a fit to the Nordheim law.

the Nordheim law. The Nordheim formula $Ax(2-x)$ roughly fits the x dependence of $\rho_{ab}(0)$, as indicated by the solid curve with $A = 54 \mu\Omega\text{cm}$. Since $\rho_{ab}(0)$ is basically determined by the impurity scattering [36], this result strongly implies that the randomness intrinsic to the Ca substitution is responsible for the residual resistivity in this system. However, if the Fermi surface parameters in this system keep the same order of magnitude as those of Sr_2RuO_4 , the mean free path estimated from the x dependence of $\rho_{ab}(0)$ should be at least one order of magnitude longer than the length between the minority ions of Ca/Sr. This is most likely due to the important fact that the Ca/Sr substitution introduces the randomness into (Ca,Sr)O planes, not directly into RuO_2 planes.

In comparison with the metallic behavior of the in-plane component, the out-of-plane resistivity $\rho_c(T)$ is less temperature dependent and in some cases even non-metallic (i.e. $d\rho/dT < 0$). In order to show the temperature dependence clearly, we display $\rho_c(T)$ normalized by the values at 300 K:

$\rho_c(T)/\rho_c(300\text{K})$ in Fig. 3.32(a). All of them were measured down to 0.3 K. $\rho_c(300\text{K})$ hardly depends on x and remains within $28 \pm 3 \text{ m}\Omega\text{cm}$ for all x .

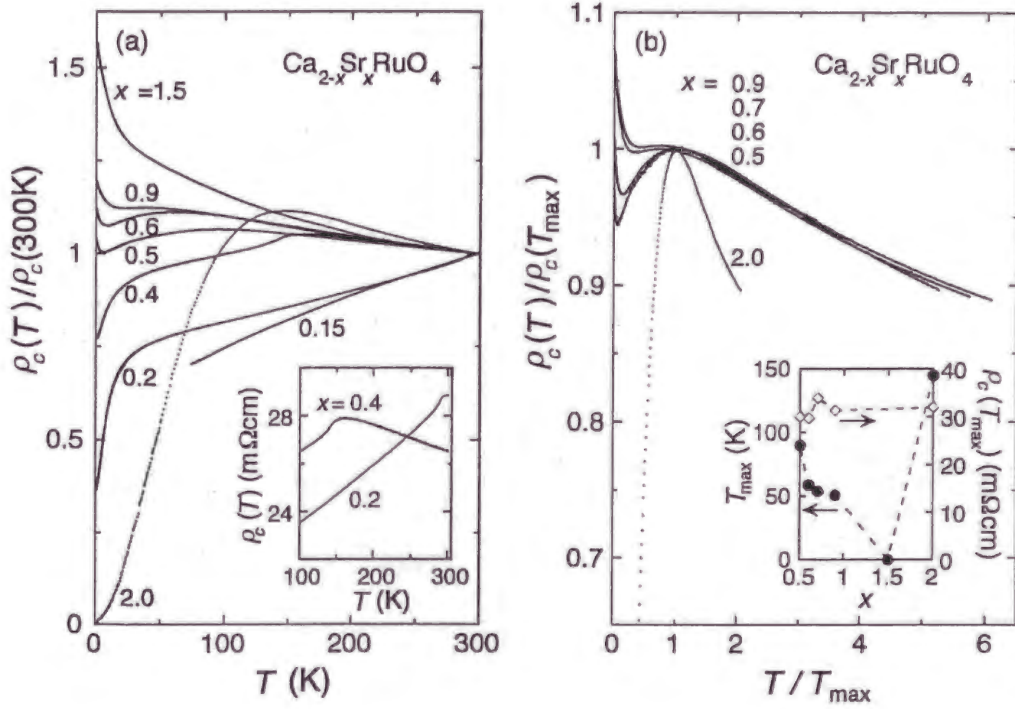


Figure 3.32: (a) Temperature dependence of the out-of-plane resistivity $\rho_c(T)$ normalized by the values at 300 K for $\text{Ca}_{2-x}\text{Sr}_x\text{RuO}_4$ with different values of x . For $x = 0.15$, the data are shown only above the M/NM transition point ~ 70 K. The inset illustrates the crossover at T_0 for $x = 0.2$ and 0.4 . (b) The variation of $\rho_c(T)/\rho_c(T_{\text{max}})$ against T/T_{max} for several values of x in region III. The inset displays the x dependence of T_{max} (solid circle) and $\rho_c(T_{\text{max}})$ (open diamond).

The MIR limit for the metallic c -axis conduction of Sr_2RuO_4 is estimated to be about $4 \text{ m}\Omega\text{cm}$ [29]. While the order of the limit should not be changed in this isostructural system, all the results of $\rho_c(T)$ are one order of magnitude higher than the limit except for Sr_2RuO_4 . Therefore, the metallic behavior observed in the region $0.15 \leq x < 0.5$ is not attributable to the coherent conduction in the band picture. Instead, we consider here the diffusion and thermally assisted hopping processes for the transport mechanism. In both processes, quasi-particles hop between layers with a jumping frequency τ_c^{-1} ,

and the out-of-plane resistivity reads

$$\rho_c = [N(E_F)\epsilon^2 l^2 \tau_c^{-1}]^{-1}, \quad (3.10)$$

where $N(E_F)$ is the density of states at E_F , ϵ is the elementary charge, and $D = l^2 \tau_c^{-1}$ is the diffusion coefficient with a jumping (interlayer) distance l .

$\rho_c(T)/\rho_{ab}(T)$ shows large anisotropy throughout the system. For example, the values for $x = 0.2, 0.9, 1.5$ and 2.0 are 120, 130, 160 and 230 at 300 K, and 780, 600, 2300 and 930 at 2 K, respectively. Therefore, the Fermi surface in this system must be remaining in almost cylindrical topology as that of Sr_2RuO_4 . Consequently, the interlayer transfer integral t_c should be so small that the in-plane scattering becomes a dominant process for the c -axis transport. In this case, one can write the jumping rate as [29, 37, 38, 39]

$$\tau_c^{-1} = t_c^2 \tau_{ab} / \hbar^2, \quad (3.11)$$

where τ_{ab}^{-1} is the in-plane scattering rate and $h = 2\pi\hbar$ is the Plank constant. From this equation, one can easily understand that even with this incoherent mechanism, ρ_c shows metallic behavior when ρ_{ab} is coherent so that τ_{ab}^{-1} becomes smaller on cooling. Hence, the metallic behavior in $0.15 \leq x < 0.5$ should arise from this mechanism.

The thermally assisted hopping process takes place when the thermal energy $k_B T$ is much larger than the effective band width W_c for the c -axis transport. In this case, the jumping rate can be expressed as [29]

$$\tau_c^{-1} = \tau_{c0}^{-1} \exp[-\alpha W_c / k_B T]^n, \quad (3.12)$$

where α is a numerical factor and n depends on the dimensionality of the hopping. This process explains the non-metallic behavior at high temperatures.

First in region I, $\rho_c(T)$ for $x = 0.15$ is metallic at all the temperatures measured down to the M/NM transition temperature of about 70 K. However in region II, a clear changeover from non-metallic to metallic behavior has been observed across T_O on cooling. (See the inset of Fig. 3.32(a) for $x = 0.2$ and 0.4 .) As we discussed in Sec. 3.3, the structural transition at

T_O involves the lattice flattening, which should enhance the interlayer coherence by enlarging t_c . In contrast with the non-metallic behavior due to the thermally assisted hopping at high temperatures, this increase in t_c by the transition must stabilize the diffusive hopping process below T_O , and thus more strongly metallic behavior appears with the Ca substitution.

In region III, however, the crossover in the temperature dependence occurs even without a structural transition, forming a maximum at T_{\max} . Figure 3.32(b) demonstrates a scaling with the normalized axes $\rho_c(T)/\rho_c(T_{\max})$ and T/T_{\max} in $0.5 \leq x \leq 0.9$. The inset of Fig. 3.32(b) illustrates the x dependence of T_{\max} and $\rho_c(T_{\max})$. $\rho_c(T_{\max})$ stays almost constant at around 32 m Ω cm, consistent with the result of the pressure dependence for Sr₂RuO₄ [29].

In this case, since the thermally assisted hopping becomes effective when $k_B T$ is larger than $W_c = 4t_c$, the crossover temperature T_{\max} should be roughly proportional to t_c . In fact, this expectation is consistent with several observations.

First, given this assumption, Eq. (3.12) qualitatively explains the nearly universal temperature dependence above T_{\max} as in Fig. 3.32(b). (The curve for $x = 2.0$ in Fig. 3.32(b) is not on the universal one. This is probably caused by the fact that only Sr₂RuO₄ has no rotational distortion as we will discuss below, which results in the difference in parameters such as α and n in Eq. (3.12).)

Second, on this assumption, T_{\max} shown in the inset of Fig. 3.32(b) indicates that W_c increases with decreasing x from 0.9 to 0.5. This is quite consistent with the expected enhancement in t_c due to the shrinkage of the interlayer distance $l = c/2$ as shown in Fig. 3.15.

Moreover, the extension of the metallic region below T_{\max} toward $x = 0.5$ is also understandable by Eq. (3.11) with this increase in t_c .

Finally, Eq. (3.12) may reproduce the nearly constant $\rho_c(T_{\max})$ in this region, as discussed in Ref. [29].

Although the metallic region becomes wider with higher T_{\max} as x changes from 1.5 to 0.5, the incoherent conduction at low temperatures still persists even at $x = 0.5$. This may be due to an anisotropic weak localization effect by

disorders in (Ca/Sr)O layers, which basically retains the coherent conduction in RuO₂ layers. Once the structural transition occurs in region II, however, $\rho_c(T)$ finally becomes metallic with a strong decrease at low temperatures.

On the other hand in this region III, T_{\max} decreases rapidly from $x = 2.0$ to 1.5. The Ca substitution for Sr₂RuO₄ introduces not only the randomness in SrO layers, but also the distortion in RuO₂ layers. Actually, the recent powder neutron diffraction confirms that the Ca substitution drives the rotation of RuO₆ octahedra along the c -axis, which is absent in Sr₂RuO₄ [13]. Hence, this rotational distortion as well as the localization effect due to the randomness, may be correlated with the incoherent $\rho_c(T)$ at $x = 1.5$.

To summarize this section, we confirmed by the above analyses that the c -axis transport in this system is dominated by the hopping process, which systematically changes from diffusive metallic hopping to the thermally assisted one with the Sr content x and the temperature, characterized by the small t_c (\sim several 10 K) due to the quasi-two-dimensional electronic structure.

Chapter 4

Discussion

4.1 Origin of the Magnetoelastic Coupling in Ca_2RuO_4

To understand those rich and unusual phenomena in $\text{Ca}_{2-x}\text{Sr}_x\text{RuO}_4$, we will discuss the variations of the ground state magnetism and electronic structure. First, let us look into the Mott insulator Ca_2RuO_4 . The neutron diffraction measurement by Braden *et al.* [11] has revealed strong magnetoelastic coupling in Ca_2RuO_4 . They reported severe flattening as well as tilting of RuO_6 octahedra on cooling toward its Néel temperature. The in-plane oxygen O(1)-O(1) distance elongates along the b -axis of the Pbca unit cell, while the Ru - apical oxygen O(2) bond shortens. However, once the staggered magnetic moment starts to align along the b -axis, both flattening and tilting of RuO_6 octahedra saturate at lower temperatures.

The flattening of octahedra may be understood simply by Jahn-Teller effect. As discussed below, it is owing to the flattening of the octahedra that d_{xy} orbital will have lower energy than the other two. Therefore, the flattening is naturally explained by Jahn-Teller effect to produce this orbital splitting, which stabilizes the fourth electron in comparison with the degenerate case [8, 11].

However, in order to explain the strong magnetoelastic coupling, we have to take account of spin-orbit coupling. Since the elongation of the O(1)-O(1) distance along the b -axis induces a distinct orthorhombic crystal field in the sequence of the flattening, the t_{2g} orbitals should split into three non-

degenerate ones: $d_{x_0^2-y_0^2}$ with the lowest energy, $d_{z_0x_0}$ in the middle, and $d_{y_0z_0}$ with the highest energy. Here, the x_0 , y_0 and z_0 -axes correspond to the a , b and c -axes of the orthorhombic $Pbca$ unit cell, respectively. (If we take the x and y -axes along the in-plane Ru-O bonds as in the $I4/mmm$ cell, $d_{x_0^2-y_0^2}$, $d_{y_0z_0}$ and $d_{z_0x_0}$ are transformed into d_{xy} , $(d_{zx} - d_{yz})/\sqrt{2}$ and $(d_{zx} + d_{yz})/\sqrt{2}$, respectively.) Basically, the tilting of RuO_6 octahedra along the b -axis also stabilizes the above configuration, generating the orthorhombic crystal field by the second-nearest oxygens in the plane from a Ru-ion. In this situation, the second order perturbation theory for the spin-orbit coupling allows us to deduce that the orthorhombic b -axis should become the easy-axis of the spin alignment, which agrees with the observation of Braden *et al.* [11].

At the same time, since the shortening of the out-of-plane Ru-O bond is nearly twice as much as the elongation of the in-plane one, the $d_{x_0^2-y_0^2}$ or d_{xy} orbital should have much lower energy than the other two orbitals. Given the four electrons in the t_{2g} orbitals, such electronic structure may well realize a half-filled configuration at E_F (with two electrons in $(d_{zx} - d_{yz})/\sqrt{2}$ and $(d_{zx} + d_{yz})/\sqrt{2}$ orbitals as shown in Fig. 4.1), which favors AF superexchange coupling between neighboring spins. As a result, the orthorhombic distortion enhanced toward T_N stabilizes both superexchange interaction and spin-orbit coupling in the Néel state. In this sense, the observed strong magnetoelastic coupling should be a cooperative phenomenon involving Jahn-Teller effect, superexchange and spin-orbit coupling.

4.2 Ground State Crossover in the Metallic Region

4.2.1 Electronic Configuration of Sr_2RuO_4

NMR studies have revealed that Sr_2RuO_4 exhibits exchange-enhanced paramagnetism, which is ascribable to a local ferromagnetic coupling between in-plane spins at neighboring sites [23, 40]. The origin of this coupling should consist in the electronic configuration. Because the out-of-plane Ru-O bond is longer than the in-plane ones in Sr_2RuO_4 , d_{xy} should have slightly different energy among the t_{2g} orbitals. However, the two-dimensionally spreading d_{xy}

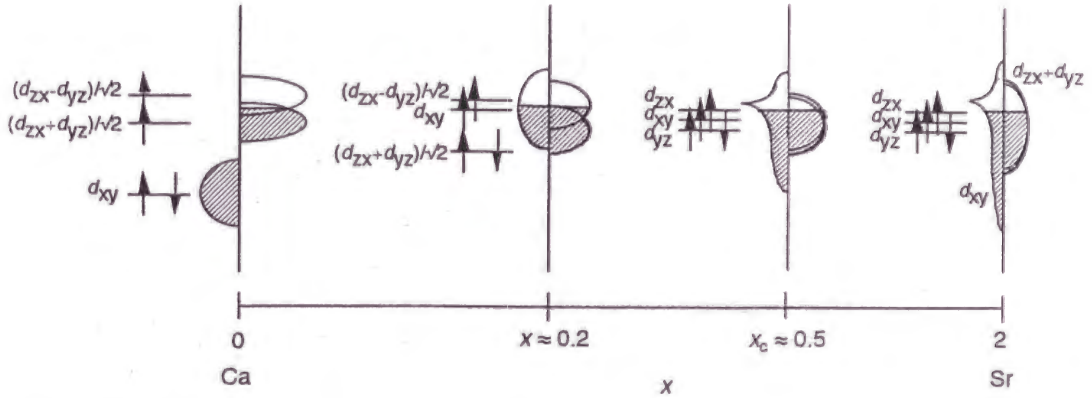


Figure 4.1: Schematic variation of the electronic configuration in $\text{Ca}_{2-x}\text{Sr}_x\text{RuO}_4$ according to the band splitting model.

forms the γ band wide enough to degenerate with the $d_{yz, zx}$ orbitals that produce rather narrow α and β bands reflecting their one-dimensional networks [19]. Consequently, the Ru^{4+} t_{2g} band provides the electronic configuration of *four electrons in the triply degenerate band*. In addition, according to the band structure calculation [19], the γ band has a large peak in the density of states (DOS) slightly (~ 50 meV) above E_F due to van Hove singularity (vHS), characteristic of a two dimensional system. Thus, it results in a strongly asymmetric DOS of the overall t_{2g} band.

According to the theories on ferromagnetism in the strongly correlated systems [41], such an asymmetric DOS with a strong peak near E_F favors ferromagnetism for its ground state, while a symmetric, half-filled band stabilizes antiferromagnetism. Although the electronic configuration of Sr_2RuO_4 nearly satisfies the former condition, no substantial FM fluctuation has been detected so far. It is probably because of the rather low $N(E_F)$ that the FM fluctuations are not well developed to a wide range but remain local so as to realize the exchange-enhanced paramagnetism [42].

We note that a recent inelastic neutron scattering measurement has revealed the incommensurate spin fluctuations located at $(\pm 0.6\pi/a, \pm 0.6\pi/a, 0)$ [43]. This is consistent with the prediction of nesting instability between α and β bands by a band structure calculation [44]. One dimensionality of

$d_{yz, zx}$ orbital network results in this nesting effect. For the superconductivity, however, we speculate that the local ferromagnetic coupling mentioned above possibly stabilizes the spin-triplet pairing of Sr_2RuO_4 , while the incommensurate spin fluctuations may have a minor or even an adverse effect. Mazin and Singh examined competition between p - and d -wave superconductivity by the calculation including both the incommensurate and FM spin fluctuations, and drew a similar conclusion [44, 45].

4.2.2 Band Splitting Model

The Ca substitution in Sr_2RuO_4 brings about the evolution of the critical behavior of ferromagnetism in the transport and magnetic properties, and finally induces the 'marginal' FM ordering at $x = 0.5$ just near the structural instability point at $x_c \simeq 0.5$. In contrast, once the system becomes orthorhombic from tetragonal across the structural transition, it is the AF correlation that becomes substantial, especially in the M-M region at $x < 0.5$. For the simplified picture of this switching of magnetic coupling, we propose the *band shape and filling dependent magnetism based on a band splitting model*, which is schematically illustrated in Fig. 4.1.

First, let us discuss the origin of the evolution of FM correlation toward x_c in region III. While Sr_2RuO_4 has no structural distortion, the Ca substitution stabilizes and enhances the rotational distortion of RuO_6 octahedra along the c -axis, as we mentioned in Sec. 3.5. As a consequence, the rotational distortion causes the following two main effects to enhance the FM coupling.

One is the band narrowing which enlarges $N(E_F)$. The distortion weakens the orbital hybridization and reduces the band-width. At the same time, since the structural symmetry remains tetragonal in region III, the crystal field symmetry around a Ru ion should be basically the same. Thus, the Ca substitution will neither lift the triple degeneracy of the bands, nor blunt the vHS. Therefore, the system should keep basically the same asymmetric DOS which favors ferromagnetism. Additionally, the band-narrowing will enhance the vHS, thereby $N(E_F)$ as well, so that the FM coupling gets stronger by the Stoner mechanism. This tendency is consistent with results by a recent

mean field theory based on the band structure of Sr_2RuO_4 [46].

Secondly, the rotation of octahedra will produce the stronger hybridization between d_{yz} and d_{zx} , which weakens the one-dimensional nature of α and β bands. Thus the nesting of these bands, the origin of the incommensurate spin correlation in Sr_2RuO_4 , may become weaker with decreasing x . As a result, the rotational distortion should develop the FM coupling from the enhanced paramagnetism of Sr_2RuO_4 .

In the M-M region, however, the triple degeneracy must be lifted by the structural transition to the orthorhombic phase. The two-fold anisotropy of the in-plane susceptibility below T_O indicates the broken tetragonal symmetry, which lifts the degeneracy of d_{yz} and d_{zx} orbital bands: the α and β bands. As the neutron diffraction measurement has clarified [13], the in-plane O(1)-O(1) bond of octahedra splits into a shorter one along $[110]$ and a longer one along $[1\bar{1}0]$ below T_O , while the Ru-O(1) and Ru-O(2) bonds keep their lengths almost the same as those for $x = 0.5$ as well as for Sr_2RuO_4 . Considering both the hybridization between the orbitals and the crystal field effect, the splitting in the bond length should bring about the following band degeneracy lifting, similar to the discussion in Sec. 4.1: the $(d_{zx} + d_{yz})/\sqrt{2}$ orbital will form a band with a lower energy, whereas the $(d_{zx} - d_{yz})/\sqrt{2}$ will generate a band with a higher energy, as depicted in Fig. 4.1. The change in the real space configuration of orbitals due to the above orbital ordering is schematically shown in Fig. 4.2. Since the lowest energy band absorbs more electrons, the filling of the bands at E_F decreases toward one half. Taking account of the spin-orbit coupling, this model naturally explains the in-plane anisotropy of the susceptibility in the M-M region.

Moreover, the symmetry breaking distortion may lift degeneracy of the states piled up at the vHS of the γ band, as what is discussed for the case in Ca substitution of $\text{Ca}_{1-x}\text{Sr}_x\text{RuO}_3$ [47, 48]. Therefore, due to the band splitting and the suppression of the vHS, the band at E_F will become more symmetric with smaller $N(E_F)$. This change from the asymmetric, strongly peaked band to the symmetric, half-filled band should weaken the FM coupling, but instead enhance the AF superexchange coupling in the M-M region.

In this model, the band degeneracy controls the electron filling of each

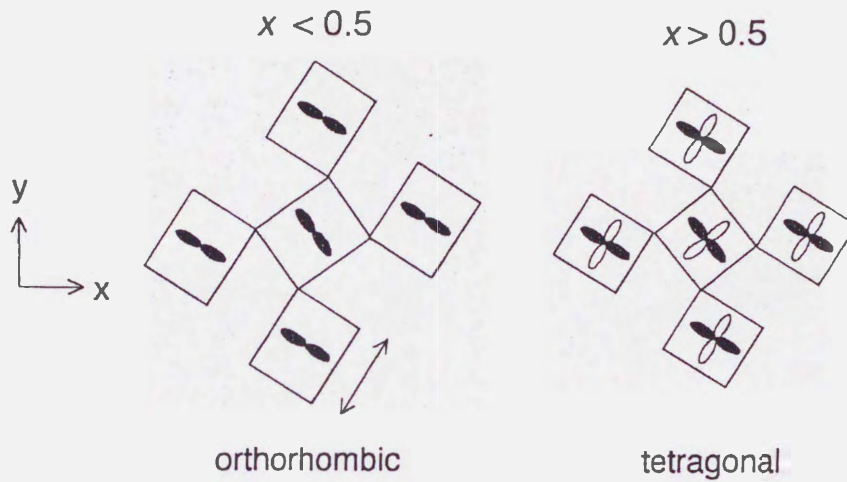


Figure 4.2: Schematic view of the real space configuration of the orbitals at the Fermi level E_F . RuO_2 planes with the rotational distortion are schematically represented by rectangles. For the tetragonal phase with $x > 0.5$ (right hand side), the two orbitals $(d_{zx} + d_{yz})/\sqrt{2}$ (a pair of open ellipses) and $(d_{zx} - d_{yz})/\sqrt{2}$ (a pair of solid ellipses) are degenerate at E_F , but for the orthorhombic phase with $x < 0.5$ (left hand side), the only $(d_{zx} - d_{yz})/\sqrt{2}$ (a pair of solid ellipses) is expected at E_F owing to the orbital ordering. (See also Fig. 4.1.) For simplicity, d_{xy} orbital is not shown here, which is expected to be at E_F at either side of x . The arrow denotes the direction of the elongation of O(1)-O(1) distance in the orthorhombic phase.

band. This differs from the carrier doping to the single $d_{x^2-y^2}$ band of the high- T_c cuprates by chemical substitutions in block layers. In contrast with this type of 'real space doping', the filling control here may be called the ' k -space doping.'

We note here the significant dependence on this filling of magnetic coupling, from the FM one at x_c with $2/3$ filling to the AF one at $x \simeq 0.2$ with effectively half filling, while the shape of the DOS should also be vital for the switching of magnetic coupling as we discussed above. In fact, this dependence is consistent with the theoretical studies by Alexander and Anderson [49], and by Moriya [50]. Based on the mean-field theory using the Anderson impurity model, they showed that the magnetic coupling switches from FM exchange to AF superexchange as the filling approaches one half. Especially, Moriya predicted that such a switching occurs at around 60% filling in the case with a simple band structure [50]. Notably, this suggests that the $2/3$ filling in region III is already quite close to the critical point, as long as $N(E_F)$ is large enough owing to the asymmetric DOS.

Then, why does the band splitting dominantly occur below x_c instead of a FM ordering? In order to understand this, we have to take account of the orbital degree of freedom. As $N(E_F)$ increases with band narrowing, the triply degenerate bands are prone to meet a Jahn-Teller type instability as well as a FM instability. In fact, the gap by the Jahn-Teller effect will stabilize the fourth electron in comparison with the degenerate case, and this stabilization energy becomes larger for a narrower band with higher $N(E_F)$. Therefore, we suggest that in region III, these instabilities compete with each other, and consequently the structural transition for the ground state takes over at x_c .

Moreover, the appearance of the 'marginal' FM ordering only around x_c should also be the result of the competition. The FM ordering is stable only while the Jahn-Teller type orbital ordering is negligible and thus the DOS keeps its high intensity. Once the orthorhombic lattice distortion becomes large enough, the FM ordering disappears.

However, this competition mechanism does not fully explain why the structural instability should coincide with the ferromagnetic quantum criti-

cal point. This intriguing observation described in Sec. 3.4.4 implies some unusual but inevitable relation between the spin and orbital degree of freedom in this system.

Moreover, the critical phenomena associated with orbital fluctuations and/or dynamical Jahn-Teller effect are expected on the verge of the instability point. This orbital fluctuations may lead to a nonuniform exchange interaction of spins through dynamical lifting of the orbital degeneracy. This dynamical coupling between spins and orbitals, which is recently suggested in the case of V_2O_3 [51, 52], would tend to suppress a magnetic (especially FM) long-range order at around x_c , and thus could be the reason why the transition temperature of 'magninal' FM is so low as 0.5 K.

Across $x \approx 0.2$ into region I, the first-order structural transition occurs [8] and induces another type of orbital ordering by the Jahn-Teller effect, as we discussed in Sec. 4.1. Supported by this orbital ordering, the system finally achieves the AF long-range order as well as the insulating ground state.

Chapter 5

Conclusion

The generic phase diagram of the high- T_c superconductors established by enormously intensive studies symbolizes one of the most important issues in the strongly correlated systems: how unconventional superconductivity appears through the Mott transition. Although the superconducting symmetry has been determined to be d -wave and it has been gained consensus that the strong antiferromagnetic correlation in the CuO_2 plane should be vital for the mechanism of the d -wave superconductivity, this significant problem coping with the mechanism of both the appearance of the superconductivity and the Mott transition has yet to be solved. Following the studies in the cuprates, the discovery of the p -wave superconductivity in the layered perovskite ruthenate Sr_2RuO_4 naturally lead our interest to the correspondingly important problem: How is this spin-triplet superconductivity correlated with the Mott transition?

In our study, we have found the new Mott insulator Ca_2RuO_4 and established the phase diagram of $\text{Ca}_{2-x}\text{Sr}_x\text{RuO}_4$, which bridges a new type of Mott transition route between the Mott insulator Ca_2RuO_4 and the spin-triplet superconductor Sr_2RuO_4 . The results make a sharp contrast to the generic phase diagram of the high- T_c superconductors, in which the spin-singlet d -wave superconductivity appears just next to the Mott transition, in the following senses.

First, the rich and unusual phase diagram of $\text{Ca}_{2-x}\text{Sr}_x\text{RuO}_4$ demonstrates that the orbital degree of freedom, which is absent in the cuprates with a single $d_{x^2-y^2}$ orbital, plays a vital role in the Mott transition mechanism and

also in the itinerant magnetism near the Mott transition.

The structural transition at the metal/non-metal transition strongly suggests that a Jahn-Teller orbital ordering is the primary origin for the Mott transition in this system. Besides this, in the metallic phase near the Mott transition, the magnetic coupling drastically changes from a nearly antiferromagnetic to a ferromagnetic one. We clarified that this change is induced by a second-order structural transition involving another type of Jahn-Teller orbital ordering. The changes in the shape and the filling of the band due to the band splitting by a Jahn-Teller effect should be responsible for such magnetic crossover.

Moreover, we argued that the development of the FM coupling observed toward the structural instability at $x = 0.5$ implies the competition between the ferromagnetism and the Jahn-Teller orbital ordering. Remarkably, the ferromagnetic state finally appears at low temperatures just at the structural instability at $x = 0.5$. This implies a novel and inevitable correlation between orbital and spin degrees of freedom. To the best of our knowledge, this is the first case of the itinerant ferromagnetism in the quasi-two-dimensional system. The possibility of the two-dimensional FM spin fluctuation suggested by the observed critical behavior should be confirmed with further extensive measurements.

The other important aspect, in contrast with the high- T_c superconductors, is that the phase diagram shows how the spin-triplet superconductor Sr_2RuO_4 is connected to the ferromagnetic instability. We revealed the systematic development of the critical behavior of ferromagnetism toward the instability point $x = 0.5$ by the band-narrowing from Sr_2RuO_4 . This experimentally provides the first example of the relation between the spin-triplet superconductivity and the ferromagnetism and must be significant to clarify the mechanism of the occurrence of the spin-triplet superconductivity.

With these rich and unusual phenomena, the new quasi-two-dimensional Mott transition system $\text{Ca}_{2-x}\text{Sr}_x\text{RuO}_4$ may well serve as an archetypal system in the study of the strongly correlated electron systems, especially to help deepening our insight into the role of the orbital degree of freedom in the itinerant magnetism and superconductivity near a Mott transition.

Acknowledgement

The author wishes to express his sincere thanks to Professor Yoshiteru Maeno for his direct guidance and stimulating discussion, and to Professor Takehiko Ishiguro for his helpful discussion and encouragement. He wishes to express appreciation to Dr. Markus Braden and Mr. Oliver Fiedt for their good collaboration in neutron diffraction measurements, to Professor Kosaku Yamada, Professor Manfred Sigrist and Professor Toshizo Fujita for their helpful discussion and kind support. He is grateful to Dr. Shin-ichi Ikeda for his collaboration and helpful discussion especially for the syntheses of Ca_2RuO_4 , and to Professor Masatoshi Shiga and Dr. Hiroyuki Nakamura for their guidance and fruitful discussion in magnetism. He thanks Mr. Hideto Fukazawa, Masanari Minakata and Mr. Takashi Ando for their helpful collaboration in the syntheses and crystal growth of $\text{Ca}_{2-x}\text{Sr}_x\text{RuO}_4$ and the measurement on them, and Dr. Zhiqiang Mao for important contribution in establishing the crystal growth. He deeply thanks Professor Andy Mackenzie for his collaboration and suggestive discussions and Dr. Hiroshi Yaguchi for his useful advice. He also wishes to thank Dr. Shuji Nishizaki, Dr. Eiji Ohmichi, Mr. Yasumitsu Mori and the other members of the Solid State Physics Laboratory for their technical support and valuable discussions. He is also grateful to the members of K. Kosuge's laboratory for allowing the use of their X-ray diffractometer. He acknowledges Japan Society of the Promotion of Science for the financial support. Finally, he wishes to remark thanks to the members of my family for their good supports and encouragement for his study.

Appendix A

Appendices

A.1 Synthesis of polycrystalline $\text{Ca}_{2-x}\text{Sr}_x\text{RuO}_4$

The condition of the synthesis of polycrystalline $\text{Ca}_{2-x}\text{Sr}_x\text{RuO}_4$ allows only a narrow window for the appropriate heating temperature and atmosphere that is heavily dependent on x . We synthesized polycrystalline $\text{Ca}_{2-x}\text{Sr}_x\text{RuO}_4$ from CaCO_3 (purity 4N), SrCO_3 (4N) and RuO_2 (3N) mixed in the stoichiometric proportion. The mixtures were pressed into pellets of the diameter 10 mm under about 2000 kgf/cm². A tubular furnace, which allows controlled gas flow, was used for the sintering. We explored the heating temperature between 1100 and 1570°C, and the O₂ partial pressure between 0 and 0.01 bar in Ar + O₂ atmosphere with the total pressure of 1 bar. In order to minimize the evaporation of RuO₂ at high temperatures, we directly inserted pellets into a hot furnace, and after heating, pulled them out of the furnace hot and quenched them in air. Heating periods of 12 and 16 hr were employed, but they yielded no significant difference.

Figures A.1(a) and (b) represent the dependence of the dominant phase in a pellet on the reaction temperature after the initial heating in the atmosphere of 99% Ar + 1% O₂ and 99.9% Ar + 0.1% O₂, respectively. The stability range of $\text{Ca}_{2-x}\text{Sr}_x\text{RuO}_4$ (214 phase in Fig. A.1(a) and (b)) remarkably changes with oxygen partial pressure. Furthermore, even in the same atmosphere, we see the significant and systematic variation of the stable temperature range with x for the 214 phase. Generally, the atmosphere becomes more reducing by raising temperature as well as by decreasing the oxygen

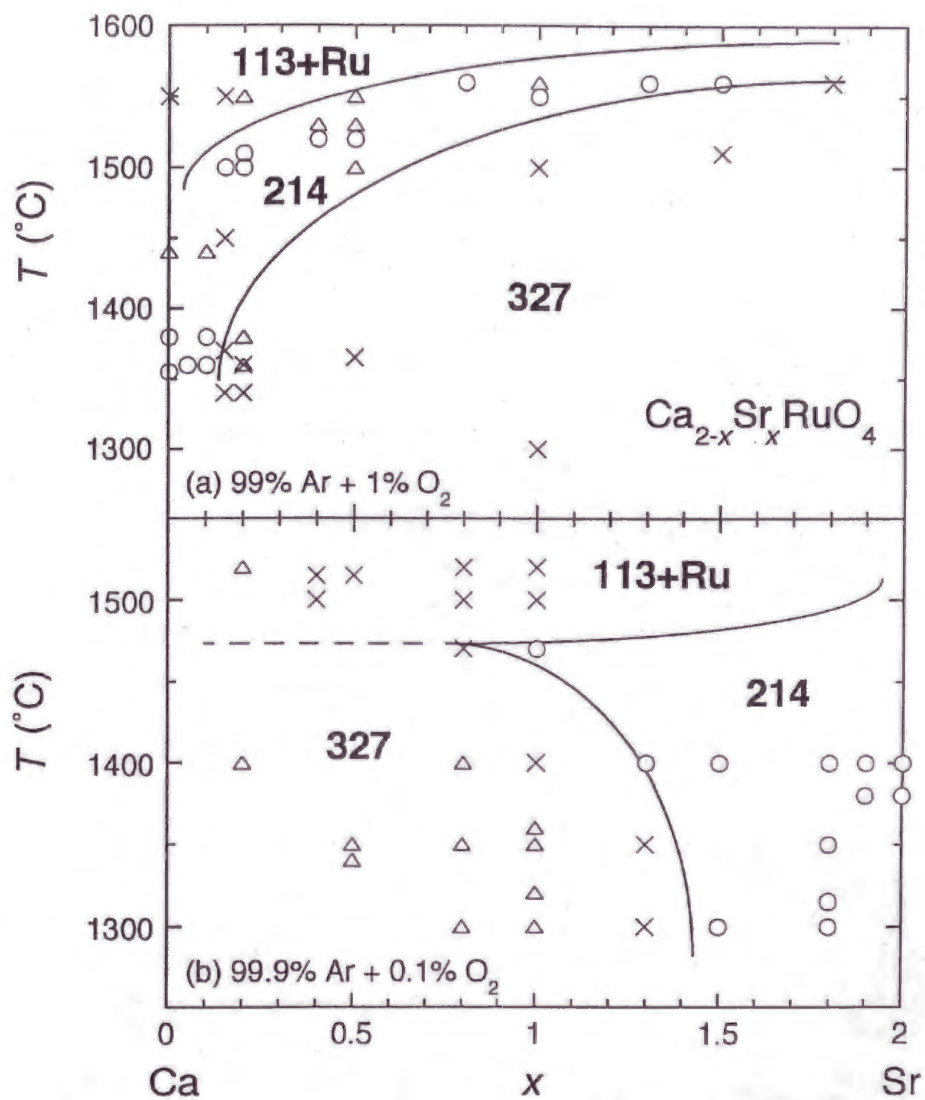


Figure A.1: Dominant phases in polycrystalline pellets as a function of the heating temperature and the Sr concentration x under the atmosphere of (a) 99% Ar+ 1% O_2 and (b) 99.9% Ar+ 0.1% O_2 . The circle, triangle and cross indicate that the fraction of the 214 phase is approximately more than 80%, around 50% and less than 30%, respectively. 327, 113, and Ru indicate that the dominant phase is $Ca_{3-x}Sr_xRu_2O_7$, $Ca_{1-x}Sr_xRuO_3$ and Ru metal, respectively. Although not shown in (a), only Sr_2RuO_4 ($x = 2$) has a wide temperature range of stability (from 1000 °C to about 1500 °C) even at 1 % O_2 .

partial pressure. Taking account of the physical phase diagram of magnetic and electrical properties described below, Figs. A.1(a) and (b) suggest that the metallic 214 phase is more stable under rather reducing condition, reflecting the expected stronger covalency of the metallic Ru-O bond. Although the single phase was obtained using those two types of atmosphere, we sometimes had difficulty in obtaining well-sintered samples for the region $0.2 \leq x \leq 1.0$. This is most likely due to the heavy evaporation of RuO_2 under rather high

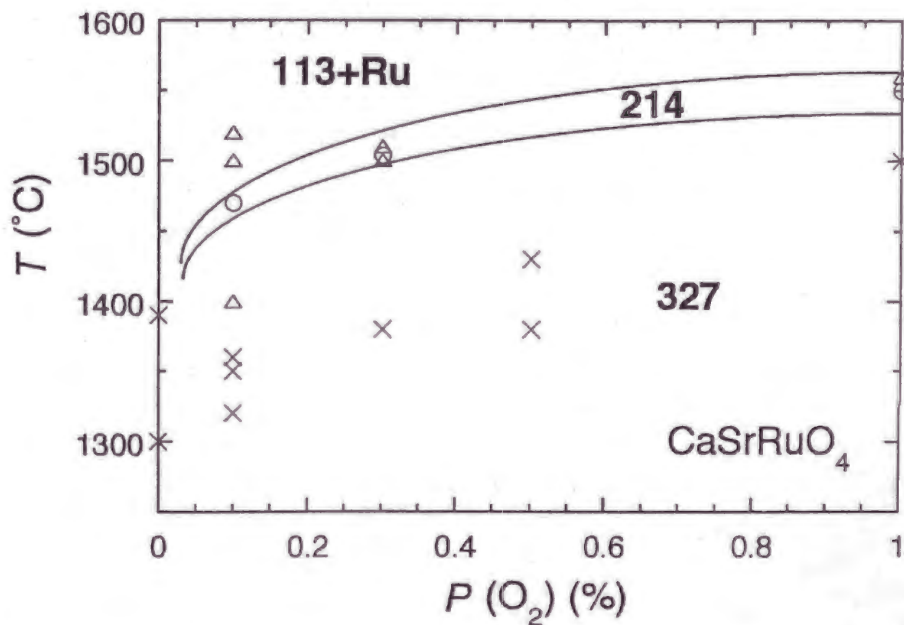


Figure A.2: Dominant phases in polycrystalline pellets as a function of the reaction temperature and the oxygen partial pressure $P(\text{O}_2)$ in the mixture of Ar and O_2 with the total pressure of 1bar. The nominal composition is CaSrRuO_4 ($x = 1.0$). The circle, triangle and cross indicate that the fraction of the 214 phase is approximately more than 80%, around 50% and less than 30%, respectively.

heating temperatures as in Figs. A.1(a) and (b). In order to lower the temperature for the synthesis, we carefully investigated the atmosphere and temperature dependence of the dominant phase in pellets with $x = 0.2, 0.4, 0.5, 0.8$ and 1.0 . Figure A.2 presents the result for the case with $x = 1.0$.

The systematic change of the reaction temperature in Figs. A.1(a),

A.1(b), and A.2 suggests the following two competing aspects. First, while the metallic 214 phase may favor rather reducing condition as noted above, too high temperature and too reducing atmosphere prevent the formation of 214 phase, but promote the reduction of RuO_2 into Ru metal. Once Ru metal appears in a pellet, we have never succeeded in obtaining the 214 phase by repeating the same heating process. This condition determines the upper limit of the annealing temperature.

Second, although the stoichiometric Sr_2RuO_4 and Ca_2RuO_4 can be obtained by annealing at relatively low temperature around 1300°C , the reaction temperature for the solution system $\text{Ca}_{2-x}\text{Sr}_x\text{RuO}_4$ increases as the Sr content x approaches 1. At the same time, $\text{Ca}_{3-x}\text{Sr}_x\text{Ru}_2\text{O}_7$ (327) phase becomes stable up to higher temperature. Such x dependence may be correlated with the additional diffusive process to mix Ca and Sr in the solution system, in contrast with the end members ($x = 0$ and 2.0).

Through the many trials described above, we have established the x dependence of the optimized reaction temperature and atmosphere, as summarized in Table A.1. The grinding and sintering were repeated several times to obtain more homogeneous samples with better crystallinity. As we mentioned above, we introduced pellets into the furnace already heated up to an appropriate temperature, and after heating, quenched them to room temperature. This procedure also helps avoid the inclusion of the 327 phase. However, to obtain well-sintered samples, we noticed that it is better to first synthesize a mixed phase of 214 with a little amount of 327 as a precursor, by reacting the raw material at slightly lower temperature (by about 50°C) than the stable one for 214. This preceding treatment yielded better sintered samples.

We also paid attention to minimizing the contamination. Especially, Ca in a sample easily reacts with an Al_2O_3 crucible and forms an eutectic Ca-Al-O compound with a melting point lower than 1300°C . In order to avoid this reaction as well as the contamination by diffusion of impurities, we placed two or three pellets of the same composition on top of a pellet of Sr_2RuO_4 in an Al_2O_3 crucible (Fig. A.3), and used only the top of the two or the middle of the three for measurements.

Table A.1: Optimized reaction temperature and atmosphere for polycrystalline $\text{Ca}_{2-x}\text{Sr}_x\text{RuO}_4$ with various values of x . For the final sintering, the samples were heated at the temperatures indicated in parentheses.

x	Temperature ($^{\circ}\text{C}$)	Atmosphere
0.00	1360-1380 (1360)	Ar+O ₂ 1.0%
0.05	1320-1340 (1340)	Ar+O ₂ 1.0%
0.10	1360-1380 (1380)	Ar+O ₂ 1.0%
0.15	1360 (1360)	Ar+O ₂ 0.3%
0.20	1380-1395 (1380)	Ar+O ₂ 0.3%
0.25	1400-1410 (1410)	Ar+O ₂ 0.3%
0.40	1520 (1520)	Ar+O ₂ 1.0%
0.50	1520 (1520)	Ar+O ₂ 1.0%
0.80	1500-1505 (1505)	Ar+O ₂ 0.3%
1.00	1503 (1503)	Ar+O ₂ 0.3%
1.30	1380-1400 (1400)	Ar+O ₂ 0.1%
1.50	1300-1400 (1400)	Ar+O ₂ 0.1%
1.80	1300-1400 (1400)	Ar+O ₂ 0.1%
1.90	1300-1400 (1400)	Ar+O ₂ 0.1%
2.00	1100-1400 (1400)	Ar+O ₂ 0.1%

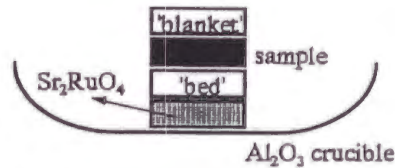


Figure A.3: Typical configuration of pellets on an Al_2O_3 (boat-type) crucible in a furnace. The solid rectangle indicates the sample pellet of $\text{Ca}_{2-x}\text{Sr}_x\text{RuO}_4$ in preparation. The 'blanket' and 'bed' are the pellets with the same composition as that of the sample. The shaded pellet is of Sr_2RuO_4 .

A.2 Crystal growth of $\text{Ca}_{2-x}\text{Sr}_x\text{RuO}_4$

We have recently succeeded in growing single crystals of $\text{Ca}_{2-x}\text{Sr}_x\text{RuO}_4$ in the whole region of x , by a floating zone method with Ru self-flux. As in the polycrystalline sample preparation, we first made a pellet from the mixture of CaCO_3 , SrCO_3 and RuO_2 . Here, the volatility of RuO_2 is also a serious problem. To compensate for this loss, we prepared a Ru-rich starting material with a composition of $\text{Ca}_{2-x}\text{Sr}_x\text{Ru}_{1.15}\text{O}_4$. After pre-synthesizing the pellet, we ground it again and pressed it under a pressure of 1500 kgf/cm^2 into a rod of 6-8 cm in length and of about 5 mm in diameter. The rod was sintered at 1000°C for 12 hr in air. Here, we also paid much attention to avoid any contamination, especially during the heating. We took the same precautions as those for the polycrystalline samples described above.

In the floating zone method, the focused infrared radiation melts the rod without any physical contact with a crucible, so that practically no contamination is expected during the crystal growth. We used a commercial infrared image furnace (NEC Machinery, Model SC-K15HD) and performed the crystal growth typically under a 90% Ar + 10% O_2 gas mixture with a total pressure of 10 bar with the growth speed of 20 mm/hr. The average size of single crystals obtained so far is about $5 \times 3 \times 3 \text{ mm}^3$, still substantially smaller than those of Sr_2RuO_4 . Details of the single crystal growth of the superconductor Sr_2RuO_4 is presented elsewhere [53].

Bibliography

- [1] J. G. Bednortz and K. A. Müller, *Z. Phys. B* **64**, 189 (1986).
- [2] Y. Maeno, H. Hashimoto, K. Yoshida, S. Nishizaki, T. Fujita, J. G. Bednortz and F. Lichtenberg, *Nature (London)* **372**, 532 (1994).
- [3] K. Ishida, H. Mukuda, Y. Kitaoka, K. Asayama, Z. Q. Mao, Y. Mori, and Y. Maeno, *Nature (London)* **396**, 658 (1998).
- [4] A.P.Mackenzie, S.R.Julian, A.J.Diver, G.J.McMullan, M.P.Ray, G.G.Lonzarich, Y.Maeno, S.Nishizaki and T.Fujita, *Phys. Rev. Lett.* **76**, 3786 (1996).
- [5] Y.Maeno, K.Yoshida, H.Hashimoto, S.Nishizaki, S.Ikeda, M.Nohara, T.Fujita, A.P.Mackenzie, N.E.Hussey, J.G.Bednortz and F.Lichtenberg, *J. Phys. Soc. Jpn.* **66**, 1405 (1997).
- [6] S. Nishizaki, Y.Maeno and T.Fujita: *J. Phys. Soc. Jpn.* **65**, 1876 (1996).
- [7] S. Nakatsuji, S. Ikeda and Y. Maeno, *J. Phys. Soc. Jpn.* **66**, 1868 (1997).
- [8] S. Nakatsuji and Y. Maeno, *Phys. Rev. Lett.* **84**, 2666 (2000).
- [9] S. Nakatsuji and Y. Maeno, *Phys. Rev. B* **62**, 6458 (2000).
- [10] S. Nakatsuji and Y. Maeno, to appear in *J. Solid State Chem.* (2000).
- [11] M. Braden, G. André, S. Nakatsuji and Y. Maeno, *Phys. Rev. B* **58**, 847 (1998).
- [12] H. Fukazawa, S. Nakatsuji and Y. Maeno, *Physica B* **281&282**, 613 (2000).

- [13] O. Friedt, M. Braden, G. André, P. Adelman, S. Nakatsuji and Y. Maeno, submitted to Phys. Rev. B (cond-mat/0007218).
- [14] C. S. Alexander, G. Cao, V. Dobrosavljevic, S. McCall, J. E. Crow, E. Lochner and R. P. Guertin, Phys. Rev. B **60**, R3422 (1999).
- [15] J.B. Goodenough and J.M. Longo: *Landolt-Börnstein New Series*, Vol. 4, part a, (eds K.-H. Hellwege and A.M. Hellwege, Springer, Berlin, 1970) pp.207-214.
- [16] I. Dzialoshinsky: J. Phys. Chem. Solids **4** 241 (1958).
- [17] T. Moriya: in *it Magnetism*, edited by G.T. Rado and H. Suhl (Academic Press, New York, 1963), Vol. I, Chap.3.
- [18] G. Cao, S. McCall, M. Shephard, J. E. Crow and R. P. Guertin, Phys. Rev. B **56**, R2916 (1997).
- [19] T. Oguchi, Phys. Rev. B **51**, 1385 (1995); D. J. Singh, Phys. Rev. B **52**, 1358 (1995).
- [20] S. Nakatsuji and Y. Maeno, J. Low Temp. Phys. **117**, 1599 (1999).
- [21] D. C. Johnston, C. A. Swenson, S. Kondo, Phys. Rev. B **59**, 2627 (1999) and references therein.
- [22] e.g. K. Yosida, *Theory of Magnetism* (Springer-Verlag, Berlin, 1996).
- [23] H. Mukuda, K. Ishida, Y. Kitaoka, K. Asayama, Z. Q. Mao, Y. Mori and Y. Maeno, J. Phys. Soc. Jpn. **67**, 3945 (1998).
- [24] T. Moriya, *Spin Fluctuations in Itinerant Electron Magnetism* (Springer-Verlag, Berlin, 1985).
- [25] e. g. see articles in J. Phys.: Condens. Matter **8** (1996).
- [26] A. J. Millis, Phys. Rev. B **48**, 7183 (1993).
- [27] e. g. T. Moriya, Y. Takahashi and K. Ueda, J. Phys. Soc. Jpn. **59**, 2905 (1990).

- [28] M. Hatatani and T. Moriya, *J. Phys. Soc. Jpn.* **64**, 3434 (1995).
- [29] K. Yoshida, F. Nakamura, T. Goko, T. Fujita, Y. Maeno, Y. Mori and S. NishiZaki, *Phys. Rev. B* **58**, 15062 (1998).
- [30] A. P. Mackenzie, R. K. W. Haselwimmer, A. W. Tyler, G. G. Lonzarich, Y. Mori, S. Nishizaki, and Y. Maeno, *Phys. Rev. Lett.* **80**, 161 (1998).
- [31] S. Kondo, D. C. Johnston, C. A. Swenson, F. Borsa, A. V. Mahajan, L. L. Miller, T. Gu, A. I. Goldman, M. B. Maple, D. A. Gajewski, E. J. Freeman, N. R. Dilly, R. P. Dickey, J. Merrin, K. Kojima, G. M. Luke, Y. J. Uemura, O. Chmaissem, and J. D. Jorgensen, *Phys. Rev. Lett.* **78**, 3729 (1997).
- [32] K. Yamada, *Prog. Theor. Phys.* **53**, 119 (1975).
- [33] S. R. Julian, A. P. Mackenzie, G. G. Lonzarich, C. Bergemann, R. K. W. Haselwimmer, Y. Maeno, S. NishiZaki, A. W. Tyler, S. Ikeda, and T. Fujita, *Physica B* **259-261**, 928 (1999).
- [34] S. Doniach and S. Engelsberg, *Phys. Rev. Lett.* **17**, 750 (1966).
- [35] A. W. Tyler, A. P. Mackenzie, S. NishiZaki and Y. Maeno, *Phys. Rev. B* **58**, 10107 (1998).
- [36] T. M. Rice and W. F. Brinkman, *Phys. Rev. B* **5**, 4350 (1972).
- [37] G. Soda, D. Jerome, M. Weger, J. Alizon, J. Gallice, H. Robert, J. M. Fabre and L. Giral, *J. Phys. (Paris)* **38**, 931 (1977).
- [38] L. Forro, V. Ilakovac, J. R. Cooper, C. Ayache and J. -Y. Henry, *Phys. Rev. B* **46**, 6626 (1992).
- [39] N. Kumar and A. M. Jayannavar, *Phys. Rev. B* **45**, 5001 (1992).
- [40] T. Imai, A. W. Hunt, K. R. Thurber and F. C. Chou, *Phys. Rev. Lett.* **81**, 3006 (1998).
- [41] J. Wahle, N. Blümer, J. Schlipf, K. Held and D. Vollhardt, *Phys. Rev. B* **58**, 12749 (1998) and reference therein.

- [42] In addition to this basic mechanism, the local FM interaction may be stabilized by the Hund's rule coupling between moments induced on in-plane oxygen O(1) sites due to the strong covalency in Ru-O bonds, as discussed in Ref. [45].
- [43] Y. Sidis, M. Braden, P. Bourges, B. Hennion, S. NishiZaki, Y. Maeno and Y. Mori, *Phys. Rev. Lett.* **83**, 3320 (1999).
- [44] I. I. Mazin and D. J. Singh, *Phys. Rev. Lett.* **82**, 4324 (1999).
- [45] I. I. Mazin and D. J. Singh, *Phys. Rev. Lett.* **79**, 733 (1997).
- [46] T. Nomura and K. Yamada, *J. Phys. Soc. Jpn.* **69**, 1856 (1998).
- [47] Y. Maeno, S. Nakatsuji and S. Ikeda, in "Physics and Chemistry of Transition Metal Oxides" (eds. H. Fukuyama and N. Nagaosa, Springer, 1999) pp 313-322.
- [48] I. I. Mazin and D. J. Singh, *Phys. Rev. B* **56**, 2556 (1997).
- [49] S. Alexander and P. W. Anderson, *Phys. Rev.* **133**, A 1594 (1964).
- [50] T. Moriya, *Prog. Theor. Phys.* **33**, 157 (1965).
- [51] M. Takigawa, E. T. Ahrens and Y. Ueda, *Phys. Rev. Lett.* **76**, 283 (1996).
- [52] W. Bao, C. Broholm, G. Aeppli, P. Dai, J. M. Honig and P. Metcalf, *Phys. Rev. Lett.* **78**, 507 (1997).
- [53] Z.Q. Mao, Y. Maeno and H. Fukazawa, to be published in *Matt. Res. Bull.* **39**, No. 11 (2000).

Quasi-Two-Dimensional Mott Transition System $\text{Ca}_{2-x}\text{Sr}_x\text{RuO}_4$

S. Nakatsuji¹ and Y. Maeno^{1,2}

¹*Department of Physics, Kyoto University, Kyoto 606-8502, Japan*

²*CREST, Japan Science and Technology Corporation, Kawaguchi, Saitama 332-0012, Japan*

(Received 28 December 1998)

We have revealed the phase diagram of $\text{Ca}_{2-x}\text{Sr}_x\text{RuO}_4$: the quasi-two-dimensional Mott transition system that connects the Mott insulator Ca_2RuO_4 with the spin-triplet superconductor Sr_2RuO_4 . Adjacent to the metal/nonmetal transition at $x = 0.2$, we found an antiferromagnetically correlated metallic region where non-Fermi-liquid behavior in resistivity is observed. Besides this, the critical enhancement of susceptibility toward the region boundary at $x_c = 0.5$ suggests the crossover of magnetic correlation to a nearly ferromagnetic state, which evolves into the spin-triplet superconductor Sr_2RuO_4 .

PACS numbers: 71.30.+h, 74.70.-b, 75.40.-s

Much attention has been paid to the quasi-two-dimensional Mott transition systems, such as high- T_c cuprates and organic conductors, for their dramatic variation of the electronic states between the extremes of ground states: insulating state and superconductivity. Particularly, the mechanism of the emergence of the unconventional superconductivity from the Mott insulator has been one of the main focuses of intense investigation. Intriguing links have also been revealed between anomalous metallic states near the metal-insulator transition and non-Fermi-liquid (NFL) behavior in the quantum critical regime of a number of heavy fermion compounds [1].

While the d -wave pairing has been revealed in the cuprates, the p -wave superconductivity in Sr_2RuO_4 , which is isostructural to one of the best studied cuprates $\text{La}_{2-x}\text{Sr}_x\text{CuO}_4$, has attracted recent interest [2-4]. The spin-triplet pairing in Sr_2RuO_4 has been demonstrated by NMR Knight shift measurement [3]. As expected from the exotic pairing, its normal state is a highly correlated metal, well described as a quasi-two-dimensional Fermi liquid [5,6]. In contrast, isovalent Ca substitution for Sr drastically changes this superconductor into the Mott insulator Ca_2RuO_4 [7,8]. The decrease of $4d$ -band width in comparison with that of Sr_2RuO_4 , caused by distortions in RuO_2 planes, leads to a Mott-Hubbard-type gap [7,9,10]. Therefore, the new solution system $\text{Ca}_{2-x}\text{Sr}_x\text{RuO}_4$ should provide the important information on the Mott transition route that involves the emergence of the spin-triplet superconductor.

In this Letter, we present the first results on the phase diagram of the quasi-two-dimensional Mott transition system $\text{Ca}_{2-x}\text{Sr}_x\text{RuO}_4$. The metal/nonmetal (M/NM) transition occurs in the Ca-rich region by varying either the Sr content or the temperature. On the verge of the M/NM transition at $x = 0.2$, we have found an antiferromagnetically (AF) correlated metallic region where non-Fermi-liquid behavior in resistivity has been observed. Furthermore, toward the region boundary at $x_c = 0.5$, the system reveals the critical enhancement of low temperature susceptibility. This suggests the crossover of magnetic correlation to a nearly ferromagnetic (FM) state,

which evolves into the spin-triplet superconductor with enhanced paramagnetism.

We have recently succeeded in synthesizing polycrystalline $\text{Ca}_{2-x}\text{Sr}_x\text{RuO}_4$ in the whole region of x , and in growing single crystals by a floating-zone method in the region $0.0 \leq x \leq 0.7$, in addition to Sr_2RuO_4 ($x = 2$). Details of the preparations will be described elsewhere [11]. The crystal structures are studied by powder x-ray diffraction at room temperature. While Ca_2RuO_4 has an orthorhombic $Pbca$ symmetry [9], all the other spectra of $\text{Ca}_{2-x}\text{Sr}_x\text{RuO}_4$ show only the peaks that are well indexed with the single pseudotetragonal symmetry, consistent with $I4/mmm$ of Sr_2RuO_4 . Determination of their precise symmetries is under investigation [12]. Here we adopt the notations for the unit cell with $I4/mmm$ symmetry. Electrical resistivity was measured down to 4.2 K by a standard four-probe dc method and down to 0.3 K by an ac method. Magnetization measurements down to 1.8 K were performed with a SQUID magnetometer.

We have determined the phase diagram as represented in Fig. 1, which consists of the following three regions:

(I) ($0 \leq x < 0.2$) AF insulating ground state. M/NM transition occurs by varying temperature except $x = 0$. Ca_2RuO_4 ($x = 0$) is an insulator at least up to 300 K. M/NM transition by varying x occurs at $x = 0.2$.

(II) ($0.2 \leq x < 0.5$) "Magnetic metallic (M-M) region" below the peak temperature T_p of the susceptibility.

(III) ($0.5 \leq x \leq 2$) Paramagnetic metal. Low temperature susceptibility exhibits critical enhancement at $x_c = 0.5$. Superconductivity with $T_c = 1.5$ K at $x = 2$.

In the paragraphs below, we will describe these characteristic properties of each region in the order of regions I, II, and III. Finally, the physical origin of this distinct variation of the ground state will be discussed.

First, we summarize in Fig. 2 the temperature dependence of the in-plane resistivity $\rho_{ab}(T)$ measured on cooling for various values of x . In region I, $\rho_{ab}(T)$ of the stoichiometric Ca_2RuO_4 ($x = 0$) basically shows activation-type insulating behavior with an activation energy of 0.2 eV [13]. Besides, the electronic specific-heat coefficient was found to be 0 ± 0.2 mJ/mol K²,

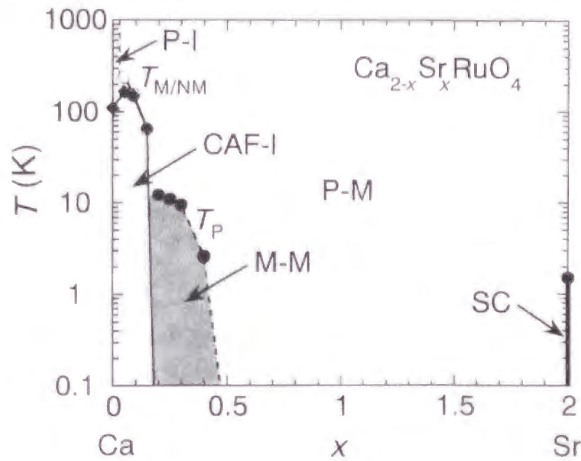


FIG. 1. Phase diagram of $\text{Ca}_{2-x}\text{Sr}_x\text{RuO}_4$ with the abbreviations: P for paramagnetic, CAF for canted antiferromagnetic, M for magnetic, SC for superconducting phase, -M for metallic phase, and -I for insulating phase. The solid circle, the open circle, and the solid diamond represent the peak temperature T_P of the susceptibility for the [001] component, the metal/nonmetal transition temperature $T_{M/NM}$, and the CAF transition temperature T_{CAF} , respectively.

which manifests that Ca_2RuO_4 is truly an insulator with no density of states at the Fermi level $N(E_F)$ [13].

In contrast, slight Sr substitution for Ca stabilizes a metallic state at high temperatures, and induces the M/NM transition at a temperature $T_{M/NM}$ on cooling as in Fig. 1. The results of $x = 0.09$ and 0.15 in Fig. 2 represent $\rho_{ab}(T)$ for region I with $T_{M/NM} = 155$ and 70 K, respectively. With abrupt increases by factors more than 10^4 at $T_{M/NM}$, they show the nonmetallic behavior described by variable-range hopping. For $x = 0.15$, for example, the data below $T_{M/NM}$ well fit $\rho_{ab}(T) = A \exp(T_0/T)^{1/4}$ with $T_0 = 9 \times 10^4$ K. This suggests that strong localization dominating the nonmetallic behavior drives the M/NM transition, preceding the gap opening toward the Mott

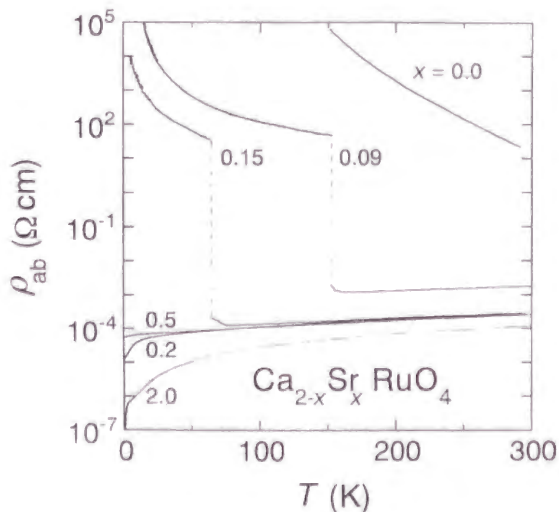


FIG. 2. Temperature dependence of the in-plane resistivity $\rho_{ab}(T)$ for $\text{Ca}_{2-x}\text{Sr}_x\text{RuO}_4$ with different values of x . The vertical broken lines are guides to the eye.

insulator. Below $T_{M/NM}$, the susceptibility χ also shows a distinct magnetic transition at a temperature T_{CAF} on cooling, which finally coincides with the M/NM transition for about $x \geq 0.1$. The magnetization vs the field (M - H curve) at 5 K exhibits weak FM hysteresis ascribable to canted AF as in Ca_2RuO_4 [7,9]. The M/NM transition of the ground state occurs at $x = 0.2$, as illustrated in Fig. 2.

Powder neutron diffraction measurements have been carried out for $x = 0.1$ and 0.2 down to 1.5 K [12], and shown that the M/NM transition either by varying x or T involves the first-order structural transition, consistent with the thermal hystereses observed in $\rho(T)$ and $\chi(T)$.

What characterizes the M-M region in region II is the susceptibility peak. Figure 3 shows $\chi(T)$ curves for $x = 0.2$ under fields of 1 T parallel to [110], [1 $\bar{1}$ 0], and [001] axes. The in-plane susceptibility exhibits the maximum and the minimum for fields along [110] and [1 $\bar{1}$ 0], respectively. There is no observable difference between field-cooled and zero-field-cooled data, so our measurements are not suggestive of spin glass ordering. The most prominent feature is the broad maximum in each axis component. Well above T_P , these components show Curie-Weiss (C-W) behavior with AF Weiss temperatures Θ_W comparable to T_P . Such characteristics indicate that some kind of AF ordering occurs at T_P .

However, the broad nature of these maxima is far from the usual sharp cusp at a Néel point. Moreover, the peak temperatures T_P for the in-plane components are definitely different from each other: $T_P^{[110]}$ for the easy-axis [110] is 8.2 K, while $T_P^{[1\bar{1}0]}$ for the hard-axis [1 $\bar{1}$ 0] is 12.2 K, identical to that for the c -axis [001]. Therefore, although the substantial reduction of the susceptibility should originate from the AF correlation, the long-range order (LRO) does not emerge at T_P , but is somehow destabilized. In fact, no magnetic LRO with a moment larger than the resolution limit of $0.05 \mu_B$ was detected for $x = 0.2$ down to 1.5 K in the neutron diffraction measurement [12].

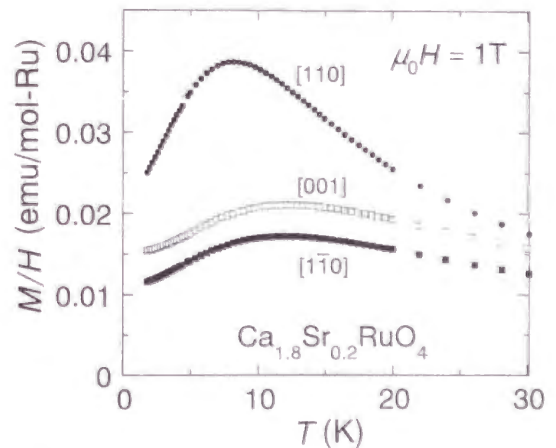


FIG. 3. Temperature dependence of the susceptibility of $\text{Ca}_{1.8}\text{Sr}_{0.2}\text{RuO}_4$ under $\mu_0 H = 1$ T parallel to each axis. Field-cooled and zero-field-cooled curves agree very well.

Another evidence for the AF correlation in the M-M region is the anisotropy of the susceptibility below T_P . As shown in Fig. 3, the [110] component decreases on cooling almost 3 times more than the others. This corresponds to the anisotropy for an AF ordering with the easy-axis [110] and with the hard-axes [110] and [001]. In fact, the anisotropy obtained here is very similar to that of the AF-LRO state in Ca_2RuO_4 [13], with spins aligned antiferromagnetically along the [110] axis [9]. Moreover, the M - H curve in this region exhibits a metamagnetic transition (for example, at $\mu_0 H \approx 2.5$ T \parallel [110] for $x = 0.2$), similar to the one observed in the ordered Ca_2RuO_4 [8]. These substantial resemblances indicate that an AF short-range order (AF-SRO) is well stabilized in the magnetic *metallic* region just next to the M/NM transition.

As presented in Fig. 4, the most intriguing systematic variation in the *metallic* regions II and III was found in the low temperature susceptibility $\chi(0)$, represented here by the value at 2 K. The inset of Fig. 4 displays $\chi(T)$ curves for region III under a field of 0.1 T parallel to the ab plane. The in-plane susceptibility is almost isotropic in this region. For Sr_2RuO_4 , the $\chi(T)$ curve is Pauli-paramagnetic for its Fermi liquid state. The Ca substitution, however, continuously changes it to C-W-like, and finally to Curie-like with $\Theta_W = 0$ K at $x = 0.5$. Corresponding to this evolution of the C-W behavior, $\chi(0)$ for $2.0 \geq x \geq 0.5$ in Fig. 4 increases with decreasing x . It is critically enhanced at $x = 0.5$, reaching a value more than 100 times larger than that of Sr_2RuO_4 .

The enhancement is consistent with the expected increase in $N(E_F)$ by the band narrowing with the Ca substitution. However, this effect alone cannot explain the

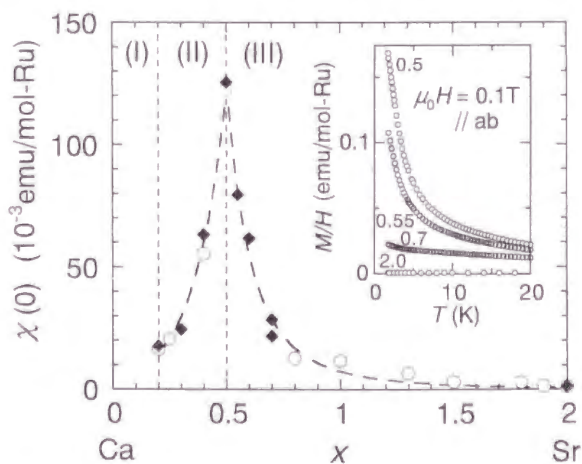


FIG. 4. $\chi(0)$: the susceptibility at 2.0 K against the Sr concentration x in the metallic regions II and III. The values for the polycrystalline samples are indicated by open circles, while for the single crystals, the solid diamonds represent the mean values $\chi_m(0)$ determined by the relation: $\chi_m(0) = \{\chi_a(0) + \chi_b(0) + \chi_c(0)\}/3$. The broken lines are guides to the eye. The inset displays $\chi(T)$ curves for region III under a field of 0.1 T parallel to the ab plane. Field-cooled and zero-field-cooled curves agree very well.

strong temperature dependence near $x = 0.5$. In an itinerant system like this, such an increase of negative Θ_W to zero is ascribable to the evolution of FM spin fluctuations [14]. Therefore, with the enlarged $N(E_F)$, it should be the Stoner enhancement that plays a significant role in the critical behavior around $x = 0.5$. In region II, on the other hand, $\chi(0)$ sharply decreases with decreasing x , reflecting the formation of the susceptibility peak at the higher temperature T_P as shown in Fig. 1.

We note that this critical enhancement of $\chi(0)$ occurs at $x = 0.5$, and thus appears to be correlated with Θ_W approaching zero in region III and T_P increasing from zero in region II. This criticality indicates a drastic change of the ground state at the M-M region boundary, most likely from the nearly FM state to the AF correlated one. Since we detected no evidence of magnetic LRO down to 0.3 K, it should be a magnetic crossover that occurs at $x_c \approx 0.5$. Quite recently, however, a preliminary neutron diffraction measurement has found a second-order structural transition in region II from a high temperature tetragonal to a low temperature orthorhombic phase [12]. It is also at x_c that the transition temperature emerges from zero, just as T_P , while it increases much more rapidly than T_P with decreasing x . This coincidence strongly implies that the structural transition induces the magnetic crossover.

The low temperature parts of $\rho_{ab}(T)$ in Fig. 2 for $x = 0.2, 0.5$, and 2 are presented in Fig. 5, where $\rho_{ab}(T) - \rho_{ab}(0)$ is plotted against $T^{1.4}$. Sr_2RuO_4 shows T -squared dependence as indicated by a fitting curve, reflecting its Fermi liquid state established by a variety of measurements [5,6]. In contrast, for $x = 0.2$ and 0.5, the in-plane resistivities severely deviate from the T -squared dependence. The best fit was obtained in the form of $\rho_{ab}(T) = \rho_{ab}(0) + AT^{1.4}$. At $x = 0.5$, this $T^{1.4}$ dependence appears below about 3 K following the T -linear one up to 5.5 K. Meanwhile, the resistivity for $x = 0.2$ starts to decrease strongly below about $T_P^{[110]} \approx 8$ K and shows the $T^{1.4}$ dependence toward the lowest temperature.

Work on heavy fermion compounds and cuprates has revealed that such NFL behavior is due to critical fluctuations, and persists to low temperature near a magnetic instability [1,15]. Therefore, the NFL behavior observed down to 0.3 K not only around $x_c \approx 0.5$ but at $x = 0.2$ suggests that the enhanced spin fluctuations, which destabilize the magnetic LRO, dominate the entire M-M region. In a two-dimensional system near AF and FM instabilities, the resistivity is expected to show T -linear [16] and $T^{4/3}$ [17] dependence, respectively. The observed $T^{1.4}$ dependence is quite close to the latter one, which is also found in Sr_2RuO_4 under pressure [18]. Along with the strong enhancement of the low temperature susceptibility, this gives a consistent interpretation that $x_c \approx 0.5$ is just near a FM instability. On the other hand, for the AF-SRO in the M-M region, there are basically two possible spin configurations: simple in-plane AF or interlayer AF with the dominant in-plane FM spin fluctuations. It is not possible to distinguish between these possibilities on the basis

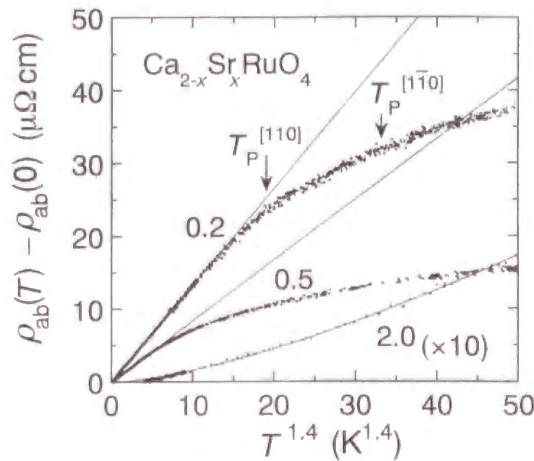


FIG. 5. Temperature dependence of the in-plane resistivity $\rho_{ab}(T)$ for $x = 0.2, 0.5,$ and 2 . Solid lines indicate fits with T^2 ($x = 2$), and $T^{1.4}$ ($x = 0.2$ and 0.5) dependence. The peak temperatures of the susceptibilities are indicated for $x = 0.2$.

of the current data. Further studies by neutron diffuse scattering are needed for this region.

In Fig. 5, it should also be noted that $\rho_{ab}(T) - \rho_{ab}(0)$ becomes smaller with x . This most probably results from the weakened inelastic (especially, spin) scattering due to the band widening. Moreover, for $x = 0.2$, the formation of AF-SRO should induce the strong decrease in $\rho_{ab}(T)$ (below T_P) because of the reduced spin scattering. In fact, well below T_P , the field dependence of the longitudinal in-plane magnetoresistance ($I \parallel H \parallel ab$) for $x = 0.2$ shows a clear peak at $\mu_0 H \approx 2.8$ T, corresponding to the metamagnetic transition, while only a negative dependence was observed above T_P [11]. Nevertheless, the residual resistivity $\rho_{ab}(0)$ for $x = 0.2$ is smaller than that for $x = 0.5$, as in Fig. 2. Since $\rho_{ab}(0)$ is basically determined by the impurity scattering [19], this is attributable to the less randomness in Ca/Sr distribution at $x = 0.2$.

Finally, let us discuss the physical origin of the distinct variation of the ground state in this system. Recent NMR studies clarified that the magnetic interaction in Sr_2RuO_4 is characterized by the weakly ferromagnetic spin fluctuations with the exchange-enhanced in-plane susceptibility [20,21]. This suggests that local spins in triply degenerate t_{2g} orbitals are coupled ferromagnetically with each other. In contrast with the half-filled case, the addition of the fourth electron will align spins at neighboring sites through Hund's coupling, thereby gaining kinetic energy against Coulomb repulsion. This local ferromagnetic interaction must be crucial for the spin-triplet pairing. Nevertheless, as in Fig. 1, Sr_2RuO_4 at $x = 2$ is the singular point for this superconductivity, which disappears already at $x = 1.95$, probably owing to the disorder intrinsic to the Ca substitution.

In contrast with undistorted Sr_2RuO_4 , the RuO_2 plane in Ca_2RuO_4 is so severely distorted that RuO_6 octahedra have unusually flattened shape along the interlayer direction through the Jahn-Teller effect [9]. Thus, the three t_{2g}

orbitals originally degenerate in Sr_2RuO_4 will split into d_{xy} with lower energy and the almost degenerate d_{yz} and d_{zx} with higher energy. Filling them with four electrons, Ca_2RuO_4 may well have the half-filled band, which favors the Mott insulating ground state with AF superexchange coupling between neighboring spins.

Connecting these opposite ground states of the end members, the nearly FM state evolved from Sr_2RuO_4 through band narrowing, starts to change into the AF correlated one beyond $x_c \approx 0.5$. The orbital rearrangement involved in the structural symmetry change may probably cause such a crossover of magnetic correlation. Consequently, not only the band-width control by the Ca/Sr substitution, but the control of the effective filling of carriers through the orbital degeneracy tuning (which may be called " k -space doping") must be essential in this Mott transition system $\text{Ca}_{2-x}\text{Sr}_x\text{RuO}_4$, in contrast with the high- T_c cuprates with a single $d_{x^2-y^2}$ orbital.

The authors acknowledge T. Ishiguro for his support and M. Braden for important collaboration, especially for allowing us to use unpublished information. They are grateful to H. Fukazawa, M. Minakata, and S. Ikeda for their technical support and valuable discussions, to A. P. Mackenzie, K. Yamada, H. Fukuyama, and K. Ishida for useful discussions. This work has been supported in part by a Grant-in-Aid for Scientific Research from the Ministry of Education, Science, Sports and Culture of Japan. One of the authors (S.N.) has been supported by JSPS.

- [1] See, for example, *J. Phys. Condens. Matter* **8** (1996).
- [2] Y. Maeno *et al.*, *Nature (London)* **372**, 532 (1994).
- [3] K. Ishida *et al.*, *Nature (London)* **396**, 658 (1998). Since the sample is in the clean limit with a mean free path ≈ 500 nm, the invariance of the Knight shift across T_c cannot be attributed to the spin-orbit scattering mechanism in the dirty spin-singlet superconductor.
- [4] G. M. Luke *et al.*, *Nature (London)* **394**, 558 (1998).
- [5] A. P. Mackenzie *et al.*, *Phys. Rev. Lett.* **76**, 3786 (1996).
- [6] Y. Maeno *et al.*, *J. Phys. Soc. Jpn.* **66**, 1405 (1997).
- [7] S. Nakatsuji *et al.*, *J. Phys. Soc. Jpn.* **66**, 1868 (1997).
- [8] G. Cao *et al.*, *Phys. Rev. B* **56**, R2916 (1997).
- [9] M. Braden *et al.*, *Phys. Rev. B* **58**, 847 (1998).
- [10] A. V. Puchkov *et al.*, *Phys. Rev. Lett.* **81**, 2747 (1998).
- [11] S. Nakatsuji *et al.* (unpublished).
- [12] M. Braden (private communication).
- [13] H. Fukazawa *et al.* (to be published).
- [14] T. Moriya, *Spin Fluctuations in Itinerant Electron Magnetism* (Springer, Berlin, 1985).
- [15] A. J. Millis, *Phys. Rev. B* **48**, 7183 (1993).
- [16] For example, T. Moriya *et al.*, *J. Phys. Soc. Jpn.* **59**, 2905 (1990).
- [17] M. Hatatani *et al.*, *J. Phys. Soc. Jpn.* **64**, 3434 (1995).
- [18] K. Yoshida *et al.*, *Phys. Rev. B* **58**, 15062 (1998).
- [19] T. M. Rice *et al.*, *Phys. Rev. B* **5**, 4350 (1972).
- [20] H. Mukuda *et al.*, *J. Phys. Soc. Jpn.* **67**, 3945 (1998).
- [21] T. Imai *et al.*, *Phys. Rev. Lett.* **81**, 3006 (1998).

Switching of magnetic coupling by a structural symmetry change near the Mott transition in $\text{Ca}_{2-x}\text{Sr}_x\text{RuO}_4$

S. Nakatsuji

Department of Physics, Kyoto University, Kyoto 606-8502, Japan

Y. Maeno

*Department of Physics, Kyoto University, Kyoto 606-8502, Japan
and CREST, Japan Science and Technology Corporation, Japan*

(Received 24 February 2000)

We studied the structural, magnetic, and transport properties of the quasi-two-dimensional Mott transition system $\text{Ca}_{2-x}\text{Sr}_x\text{RuO}_4$. In the vicinity of the metal-nonmetal (M-NM) transition at $x=0.2$, we found a structural transition accompanied by a structural symmetry change with the instability point at $x_c=0.5$. The critical change across the structural transition in the temperature dependence of the susceptibility indicates a crossover of the metallic state, most likely from the nearly antiferromagnetic state next to the M-NM transition to the nearly ferromagnetic state around x_c . The latter evolves into the spin-triplet superconductor Sr_2RuO_4 ($x=2$) with enhanced paramagnetism. We argue that the competition between the structural instability and the ferromagnetism results in such a structural symmetry change with orbital degeneracy lifting, which induces the switching of magnetic coupling. In addition, a changeover from metallic to nonmetallic behavior was observed across the structural transition in the out-of-plane resistivity, which reveals highly anisotropic transport due to the quasi-two-dimensional electronic structure.

I. INTRODUCTION

The appearance of a wide range of ground states in the 4d transition metal oxides of ruthenates has recently attracted much research attention. By controlling both the bonding state in RuO_2 layers and the layer-stacking dimensionality, perovskite ruthenates exhibit various kinds of ground states such as spin-triplet superconductivity, itinerant ferromagnetism, antiferromagnetism, and the Mott insulating state.¹

Among them, the quasi-two-dimensional $\text{Ca}_{2-x}\text{Sr}_x\text{RuO}_4$ provides a new type of Mott transition system that continuously connects the Mott insulator Ca_2RuO_4 with the spin-triplet superconductor Sr_2RuO_4 .² The phase diagram has clarified the unusual variation of the ground state in the Mott transition route toward the spin-triplet superconductor, which consists of the following three regions as in Fig. 1.

First in region I ($0 \leq x < 0.2$), the metal-nonmetal (M-NM) transition occurs by varying either the Sr content or the temperature. In region II ($0.2 \leq x < 0.5$) near the M-NM transition, an antiferromagnetically (AF) correlated metallic state has been found at low temperatures, which we will refer to as the magnetic metallic (M-M) region. Moreover, the critical increase of low-temperature susceptibility observed near its region boundary at $x_c=0.5$ suggests a dramatic change of the ground state to a nearly ferromagnetic (FM) one, which evolves into the spin-triplet superconductor in region III ($0.5 \leq x \leq 2$).

In this paper, we report on the structural, magnetic, and transport studies of the metallic region in $\text{Ca}_{2-x}\text{Sr}_x\text{RuO}_4$. In the Ca-rich region near the M-NM transition, we found a structural transition possibly of second order with the zero-temperature instability point at x_c . A detailed analysis of the temperature dependence of the susceptibility has revealed

that it is this transition that induces the magnetic crossover, most likely from the AF correlated state in the M-M region, to the nearly FM state around the instability point. The observed structural symmetry change may result in a variation in the shape and the effective filling of the triply degenerate bands through Jahn-Teller-type orbital rearrangement. We propose such a band splitting model to explain the magnetic crossover. The critical enhancement of the low-temperature susceptibility toward the structural instability point is ascribable to the result of the competition between the ferromagnetism and the Jahn-Teller instability. Finally, across the

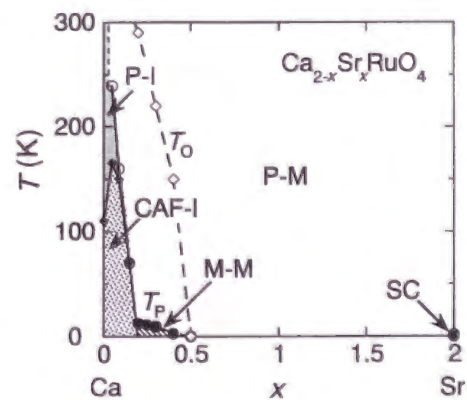


FIG. 1. Phase diagram of $\text{Ca}_{2-x}\text{Sr}_x\text{RuO}_4$ with abbreviations: P for paramagnetic, CAF for canted antiferromagnetic, M for magnetic, SC for superconducting phase, -M for metallic phase, and -I for insulating phase. The boundaries are characterized by the peak temperature T_P of susceptibility for the [001] component (solid circle), the metal-nonmetal transition temperature T_{M-NM} (open circle) and the antiferromagnetic transition temperature T_N (solid diamond). T_0 (open diamond) is the temperature below which the in-plane susceptibility starts to show twofold anisotropy.

structural transition, we observed a changeover from metallic to nonmetallic behavior in the out-of-plane resistivity, which reveals the highly anisotropic transport due to the quasi-two-dimensional electronic structure.

II. EXPERIMENT

We have succeeded in synthesizing polycrystalline samples and in growing single crystals of $\text{Ca}_{2-x}\text{Sr}_x\text{RuO}_4$ in the whole region of x . Details of the preparations will be described elsewhere.³ The crystal structures were studied by powder x-ray diffraction analysis at room temperature. The results for the single crystals indicate no trace of any second phase. For polycrystalline samples, almost all the spectra were identified as single phase, except for minor peaks of CaO detected in several batches.

To determine the oxygen content, a thermogravimetric (TG) analysis was performed, in which powdered samples were heated up to 1200°C at a rate of 2°C/min in a 90% Ar+10% H₂ flow. All the results show one sharp decrease in the thermogravimetric weight around 440°C, corresponding to the decomposition reaction $\text{Ca}_{2-x}\text{Sr}_x\text{RuO}_{4+\delta} \rightarrow (2-x)\text{CaO} + x\text{SrO} + \text{Ru} + (1+\delta/2)\text{O}_2$. From these results, we determined δ values such as -0.01(2) for the stoichiometric Ca_2RuO_4 (corresponding to S phase in Refs. 4–6) and 0.00(2) for $x=0.09, 0.2, 1.0, \text{ and } 2$. As a result, all the members of $\text{Ca}_{2-x}\text{Sr}_x\text{RuO}_4$ essentially have 4.0 oxygen atoms per formula unit and the electronic configuration is $\{Kr\}4d^4$. Due to a large crystal field, Ru^{4+} ions should be in the low-spin configuration t_{2g}^4 .

The electrical resistivity was measured by a standard four-probe dc method. Magnetization measurements from 330 K down to 1.8 K were made with a superconducting quantum interference device (SQUID) magnetometer equipped with a sample-stage rotator. For high-temperature measurements up to 700 K, we used a sample space oven inserted into the magnetometer.

III. RESULTS

A. Structural transition in region II

In Fig. 2, we display the results of x-ray diffraction measurements of powdered single crystals for $x=0.09, 0.2, \text{ and } 2$. All diffraction spectra are similar to each other, reflecting the basic K_2NiF_4 -type structure. Especially, the results of Sr_2RuO_4 ($x=2$) and $x=0.2$ agree with the same tetragonal symmetry. Meanwhile, the spectrum of $x=0.09$ shows weak but definite orthorhombicity with splitting between (hkl) and (khl) peaks. For example, the inset of Fig. 2 shows that the (110) peak of $x=0.2$ splits into (200) and (020) peaks of $x=0.09$. Accordingly, the result of $x=0.09$ is well indexed with an orthorhombic unit cell with a volume of $\sqrt{2}a_t \times \sqrt{2}a_t \times c_t$, where a_t and c_t are parameters for an $I4/mmm$ cell. This is a situation similar to the case of Ca_2RuO_4 ($x=0$) with an orthorhombic $Pbca$ symmetry.^{4,5}

The cell parameters for all the regions are shown in Fig. 3. In order to obtain an overall view, we adopted the $I4/mmm$ cell for the tetragonal lattice, the same as that of Sr_2RuO_4 , while for the orthorhombic one, $a/\sqrt{2}$ and $b/\sqrt{2}$ are given instead of a and b . At each composition, the parameters for single-crystalline samples agree well with those

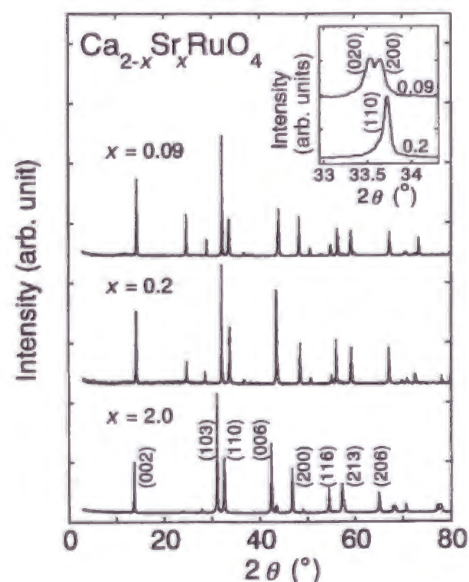


FIG. 2. X-ray (Cu $K\alpha$) diffraction spectra at room temperature for $\text{Ca}_{2-x}\text{Sr}_x\text{RuO}_4$ with $x=0.09, 0.2, \text{ and } 2$. The inset shows that the (110) peak of $x=0.2$ splits into (020) and (200) peaks for $x=0.09$. For the inset, the $K\alpha_2$ component has been subtracted.

for polycrystalline ones. This indicates that the nominal composition x for each single crystal is essentially the same as the actual composition. Starting from Sr_2RuO_4 , the volume decreases continuously with the Ca substitution owing to the smaller size of Ca^{2+} than that of Sr^{2+} . However, there are clear kinks without discontinuity in $a, b, \text{ and } c$ at $x=0.2$,

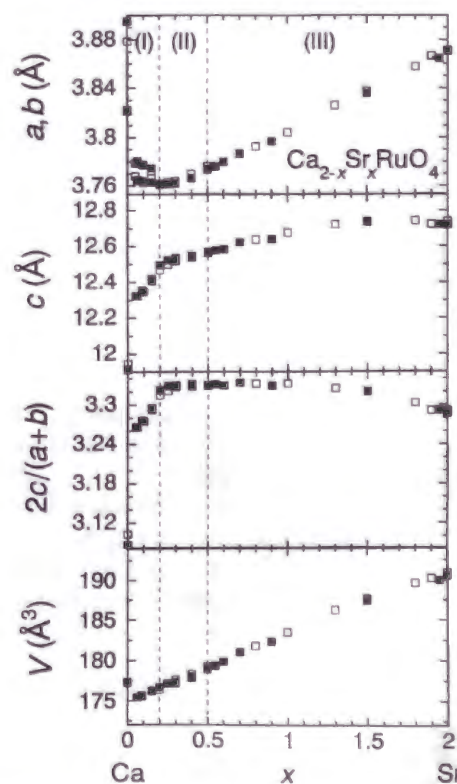


FIG. 3. Cell parameters $a, b, c, 2c/(a+b)$, and unit cell volume V of $\text{Ca}_{2-x}\text{Sr}_x\text{RuO}_4$ at room temperature. The open and solid squares represent those parameters of polycrystalline and single-crystalline samples, respectively.

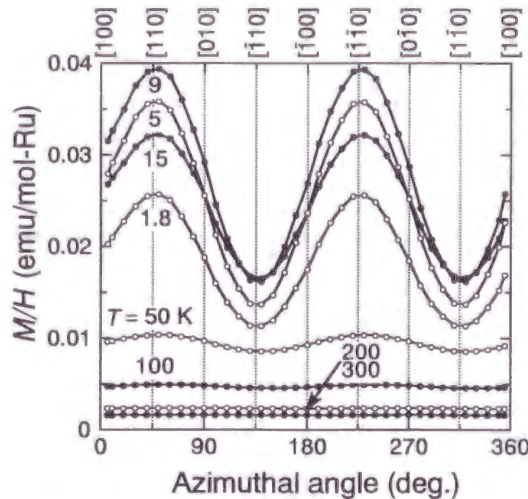


FIG. 4. In-plane anisotropy of the susceptibility under $\mu_0 H = 1$ T for $\text{Ca}_{1.8}\text{Sr}_{0.2}\text{RuO}_4$ at different temperatures.

where the splitting between a and b starts in region I. This clearly reveals a structural transition at room temperature from a tetragonal phase in regions II and III to an orthorhombic one in region I. Finally, near $x=0$, there is a large jump of the cell parameters probably due to a first-order structural transition, accompanied by the M-NM transition.² Therefore, the orthorhombic symmetry of the metallic phase in region I should be different from the orthorhombic $Pbca$ symmetry of the insulating phase.

In region II, the susceptibility $\chi(T)$ shows a broad peak at the temperature T_P , which characterizes the AF correlation in the M-M region.² At the same time, it exhibits another important aspect, namely, the in-plane anisotropy. The azimuthal angle dependence of the in-plane susceptibility at various temperatures is displayed in Fig. 4 for $x=0.2$. In comparison with the isotropic dependence at high temperatures, the anisotropy with twofold symmetry becomes evident as the temperature decreases. In order to quantify this temperature dependence, we define $R(T)$ as the susceptibil-

ity ratio of the easy axis $[110]$ to the hard axis $[1\bar{1}0]$. Figure 5 shows that $R(T)$ for $x=0.2$ increases on cooling and reaches more than 200% below $T_P \approx 12$ K. It is worth noting that, as in the inset of Fig. 5, $R(T)$ for $x=0.2$ starts to deviate from the isotropic value 100% at a characteristic temperature $T_O \approx 290$ K.

Since the magnetic anisotropy reflects the structural symmetry,⁷ the appearance of the twofold symmetry below T_O is ascribable to a structural transition from a high-temperature tetragonal to a low-temperature orthorhombic phase. We measured the in-plane azimuthal dependence of the susceptibility at various temperatures also for $x=0.3, 0.4, 0.5,$ and 0.7 . The twofold symmetry was found only in region II. From the $R(T)$ plots shown in Fig. 5, we determined T_O as 220 K for $x=0.3$, 150 K for 0.4 , and below 1.8 K for 0.5 and 0.7 . Plotting the variation of T_O in the phase diagram of Fig. 1, we notice that the T_O line crosses room temperature around $x=0.2$. Quite consistently, it is at this point where the structural transition was detected by the x-ray diffraction measurement. In addition to the strong shrinkage of the c axis in Fig. 3, the a and b axes start to elongate and split in region I. Therefore, we conclude that across the T_O line, a structural transition occurs from a tetragonal phase in the Sr-rich and high-temperature region to an orthorhombic phase in the Ca-rich and low-temperature region, involving the lattice flattening.

This transition is also detected as kinks in the resistivity data $\rho_{ab}(T)$ and $\rho_c(T)$ [see Fig. 8 for $\rho_{ab}(T)$ of $x=0.2$ and the inset of Fig. 9(a) for $\rho_c(T)$ of $x=0.2$ and 0.4]. The absence of the thermal hysteresis at these kinks suggests that this transition should be of the second order. The decrease of $\rho_c(T)$ and increase of $\rho_{ab}(T)$ below T_O are consistent with the lattice flattening. This will weaken the hybridization between the in-plane Ru $4d$ orbitals, while supporting coherent hopping between layers.

Neutron powder diffraction measurements have recently been performed for samples with $x=0.1, 0.2, 0.5,$ and 1.0 .⁸ The results confirm that the second-order structural transition from a high-temperature tetragonal to a low-temperature orthorhombic phase occurs at T_O , inducing the lattice flattening owing to orthorhombic deformation of RuO_6 octahedra as well as their tilting. Details of the results will be described elsewhere.⁸

Another important point is that T_O decreases with x and finally goes down to zero at $x=0.5$ as in Fig. 1. This suggests that $x_c \approx 0.5$ should be the instability point at absolute zero, in other words, the quantum critical point of the second-order structural transition.

B. Evolution of the temperature dependence of the susceptibility

In the entire metallic region, the $\chi(T)$ curve shows a systematic variation with x . We define the susceptibility $\chi \equiv M/H$ at low enough fields (up to 1 T) where the magnetization M shows linear dependence on the field H . In Figs. 6(a) and 6(b), we display the in-plane $\chi_{ab}(T)$ curves for single-crystalline samples in regions II and III, respectively. The inverse susceptibilities measured up to 700 K for polycrystalline samples in regions II and III are also given in the insets of Fig. 6(a) and Fig. 6(b), respectively.

In order to clarify the evolution of the temperature dependence, we performed a Curie-Weiss (CW) analysis on both

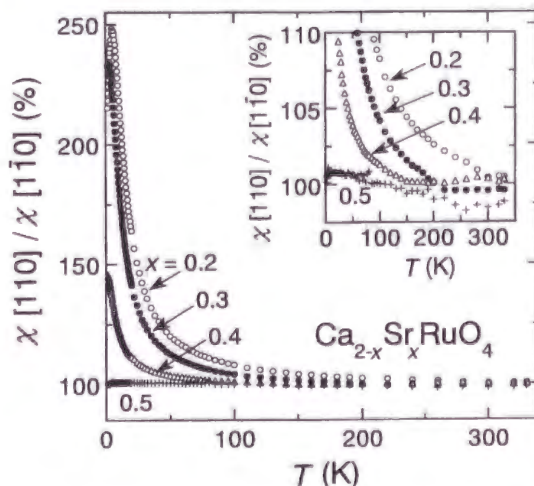


FIG. 5. Temperature dependence of the anisotropy ratio of the in-plane susceptibilities: $R(T) = \chi[110]/\chi[1\bar{1}0]$ for $\text{Ca}_{2-x}\text{Sr}_x\text{RuO}_4$ with $x=0.2, 0.3, 0.4,$ and 0.5 . The inset shows the appearance of the in-plane anisotropy at T_O .

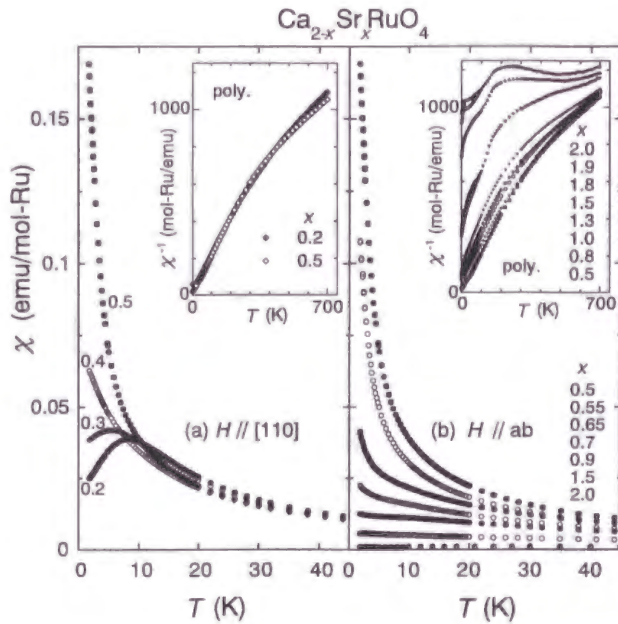


FIG. 6. Temperature dependence of the in-plane susceptibility for $\text{Ca}_{2-x}\text{Sr}_x\text{RuO}_4$ with different values of x (a) in region II for the $[110]$ component and (b) in region III. For both regions, the zero-field-cooled (ZFC) and field-cooled (FC) curves agree very well. The insets for (a) and (b) display the inverse susceptibility of polycrystalline samples in regions II and III, respectively. For polycrystalline samples only around $x=2$, the difference between the ZFC and FC curves can be seen at low temperatures. This is probably due to a small inclusion ($<0.04\%$) of ferromagnetic impurity $\text{Ca}_{1-x}\text{Sr}_x\text{RuO}_3$.

polycrystalline and single-crystalline samples. The analyses were made in a high-temperature (HT) fitting region, 300–700 K for polycrystalline samples, and in a low-temperature (LT) fitting region, 50–330 K for both polycrystalline and single-crystalline samples. For the samples in region II, we restricted the LT region from 50 K up to $(T_O - 20)$ K below the structural transition. Since Ca_2RuO_4 exhibits a first-order transition around 350 K,^{8,9} we performed the fitting for the HT region between 380 and 700 K. We adopted the fitting formula as

$$\chi = \chi_0 + \frac{C}{T - \Theta_W}. \quad (3.1)$$

Here, χ_0 is a temperature-independent term, C is the Curie constant, and Θ_W is the Weiss temperature. The effective Bohr magneton p_{eff} was derived from the formula

$$C = \frac{N_A p_{\text{eff}}^2 \mu_B^2}{3k_B}, \quad (3.2)$$

where N_A , μ_B , and k_B are Avogadro's number, the Bohr magneton, and Boltzmann's constant. For $x=1.9$ and 2, the fitting was not successful because χ is almost constant up to 700 K.

Except for near $x=2$, χ_0 has values only of the order of 10^{-4} emu/mol Ru, and is negligible in comparison with the low-temperature susceptibility $\chi(0)$ at 1.8 K.² Hence, we will focus on the fitting results of p_{eff} and Θ_W , which are summarized in Figs. 7(a) and 7(b), respectively. As shown

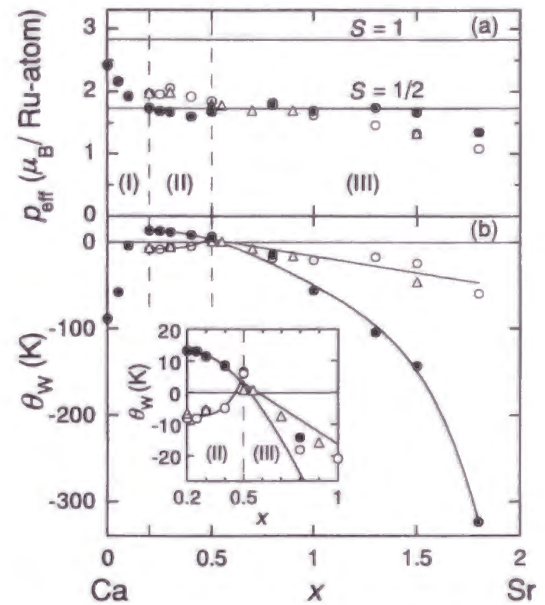


FIG. 7. Curie-Weiss parameters against the Sr content x in $\text{Ca}_{2-x}\text{Sr}_x\text{RuO}_4$. The solid and open circles correspond to the results of polycrystalline samples for the high-temperature and the low-temperature fitting regions, respectively. The open triangles represent the low-temperature fitting results of single crystals for the ab -plane component in region III and $[1\bar{1}0]$ component in region II. In the panel (a), the solid horizontal lines correspond to the effective Bohr magnetons with $S=1/2$ and 1. The inset in the panel (b) is an enlarged figure for region II. The solid curves are guides to the eye.

by band calculations,¹⁰ the states at the Fermi level (E_F) in Sr_2RuO_4 are mainly composed of $4d$ t_{2g} bands. Basically, this configuration should not change throughout the system, and thus the itinerant t_{2g} spins are responsible for the dominating CW term in Eq. (3.1).

Figure 7(a) shows a systematic x dependence of p_{eff} . First, Ca_2RuO_4 ($x=0$) has the largest p_{eff} with almost 80% of the expected value for the $S=1$ configuration. As the system goes away from the insulating phase, p_{eff} decreases rapidly in region I and finally becomes almost constant in the region $0.2 \leq x \leq 1.5$. Quite interestingly, the results in this region, especially the HT results for polycrystalline samples (solid circles), are close to the value corresponding to $S=1/2$ spin. Given Hund's coupling in the t_{2g} band, the $S=1$ configuration is naturally expected. In addition to being a metal, the enhanced spin fluctuations due to the structural two dimensionality and the orbital degree of freedom are probably responsible for the reduced p_{eff} . However, this mechanism alone does not explain why the effective S remains close to $1/2$.

According to the conventional analysis, positive and negative values of Θ_W indicate the strength of ferromagnetic and antiferromagnetic interactions, respectively. While for Ca_2RuO_4 this rule works well and $\Theta_W \approx 90$ K has the same order of magnitude as its Néel point $T_N = 110$ K, a slight Ca substitution reduces the absolute value of Θ_W much faster than that of T_N . However, the increase of negative Θ_W is still qualitatively consistent with the decrease of AF coupling of the order of T_N in region I.

In region III, Θ_W for both HT and LT regions also has

negative values, but increases with decreasing x . LT results for single crystals (open triangles) are consistent with those for polycrystalline samples (open circles). In general, a fairly large value of Θ_W is necessary to reproduce the almost temperature-independent behavior of Eq. (3.1). Accordingly, near the Pauli paramagnetic Sr_2RuO_4 , Θ_W has a large negative value, and owing to the evolution of Curie-Weiss behavior the magnitude decreases rapidly with the Ca substitution. Thus, the negative value of Θ_W in this region does not indicate the strength of the AF coupling. Alternatively, according to the self-consistent renormalization (SCR) theory,¹¹ this increase in negative Θ_W to zero can be well understood as the result of the evolution of FM spin fluctuations. The band narrowing due to the Ca substitution must be the main cause of this FM coupling, as we will discuss in Sec. IV B 2.

Here, it is also important to stress that both HT and LT results show qualitatively the same feature that Θ_W with negative values increases with the Ca substitution. Furthermore, they finally coincide around $x=0.8$ and approach zero together near $x=0.5$.

Once the system enters region II, however, Θ_W for each fitting region starts to show definitely a different x dependence, as shown in the inset of Fig. 7(b). While the result for $T>T_0$ (solid circles) increases continuously on the extended track from region III, Θ_W for $T<T_0$ of both polycrystalline samples (open circles) and the $[1\bar{1}0]$ component of single-crystalline samples (open triangles) stops increasing at $x=0.5$ but starts to decrease in region II. Notably, Θ_W for $T<T_0$ has a negative value with the same order of magnitude as T_P . This sign reversal of Θ_W across T_0 indicates that *the structural transition induces a change of magnetic coupling*.

In the ground state, this change becomes evident; it is at $x_c \approx 0.5$ that both Θ_W in region III and T_P in region II vanish so that $\chi(0)$ critically enhances as shown in Fig. 6. This criticality indicates that the ground-state magnetism drastically changes at the structural instability. The continuous increase of the HT result of Θ_W across $x=0.5$ suggests that without the structural transition, $\chi(0)$ would keep diverging with decreasing x . Therefore, the critical point at $x_c \approx 0.5$ should be very close to a FM instability. In reality, however, the AF correlation takes over toward the Mott transition in the M-M region. Here, the negative Θ_W as well as T_P must be the indicator of the strength of the AF coupling. Thus, it is natural to consider that the structural transition halts the growth of the FM instability and switches on the AF coupling.

C. Anisotropic transport properties

Reflecting the quasi-two-dimensional structure, the temperature dependence of the resistivity $\rho(T)$ is quite anisotropic. Figure 8 presents the temperature-dependent part of the in-plane resistivity: $\rho_{ab}(T) - \rho_{ab}(0)$ measured down to 0.3 K for various values of x . All curves show metallic behavior (i.e., $d\rho/dT > 0$). In fact, at low temperatures, $\rho_{ab}(T)$ are less than the Mott-Ioffe-Regel (MIR) limit of metallic conduction of about $200 \mu\Omega \text{ cm}$ for Sr_2RuO_4 ,¹² which suggests coherent metallic transport within the plane. As can be seen in Fig. 8, $\rho_{ab}(T) - \rho_{ab}(0)$ increases quite systematically with the Ca substitution. Because the temperature-dependent term is basically determined by inelastic scattering, which

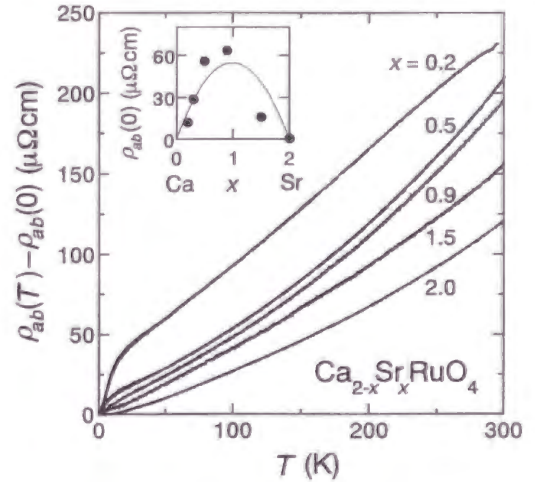


FIG. 8. Temperature dependence of the in-plane resistivity $\rho_{ab}(T)$ for $\text{Ca}_{2-x}\text{Sr}_x\text{RuO}_4$ with different values of x . The inset shows the x dependence of the in-plane residual resistivity $\rho_{ab}(0)$. The solid curve represents a fit to the Nordheim law.

becomes severe for a narrow band metal with high $N(E_F)$, this increase is consistent with the band narrowing with the Ca substitution. In addition, $\rho_{ab}(T) - \rho_{ab}(0)$ for $x=0.2$ shows a steep decrease below $T_P \approx 12$ K. This should come from a reduction of the spin scattering by the formation of AF short-range order in the M-M region.²

The x dependence of the residual resistivity $\rho_{ab}(0)$ is presented in the inset of Fig. 8. In contrast with the continuous increase of $\rho_{ab}(T) - \rho_{ab}(0)$, $\rho_{ab}(0)$ has a peak around $x=1.0$, which is qualitatively consistent with the Nordheim law. The Nordheim formula $Ax(x-2)$ roughly fits the x dependence of $\rho_{ab}(0)$, as indicated by the solid curve with $A=54 \mu\Omega \text{ cm}$. This result strongly implies that the randomness intrinsic to the Ca substitution is responsible for the residual resistivity in this system.

In comparison with the metallic behavior of the in-plane component, the out-of-plane resistivity $\rho_c(T)$ is less temperature dependent and in some cases even nonmetallic (i.e., $d\rho/dT < 0$). In order to show the temperature dependence clearly, we display $\rho_c(T)$ normalized by the values at 300 K: $\rho_c(T)/\rho_c(300 \text{ K})$ in Fig. 9(a). All of them were measured down to 0.3 K. Here $\rho_c(300 \text{ K})$ hardly depends on x and remains within $28 \pm 3 \text{ m}\Omega \text{ cm}$ for all x .

The MIR limit for the metallic c -axis conduction of Sr_2RuO_4 is estimated to be about $4 \text{ m}\Omega \text{ cm}$.¹³ While the order of the limit should not be changed in this isostructural system, all the results of $\rho_c(T)$ are one order of magnitude higher than the limit except for Sr_2RuO_4 . Therefore, the metallic behavior observed in the region $0.15 \leq x < 0.5$ is not attributable to the coherent conduction in the band picture. Instead, we consider here the diffusion and thermally assisted hopping processes for the transport mechanism. In both processes, quasiparticles hop between layers with a jumping frequency τ_c^{-1} , and the out-of-plane resistivity reads

$$\rho_c = [N(E_F)e^2l^2\tau_c^{-1}]^{-1}, \quad (3.3)$$

where $N(E_F)$ is the density of states at E_F , e is the elementary charge, and $D = l^2\tau_c^{-1}$ is the diffusion coefficient with a jumping (interlayer) distance l .

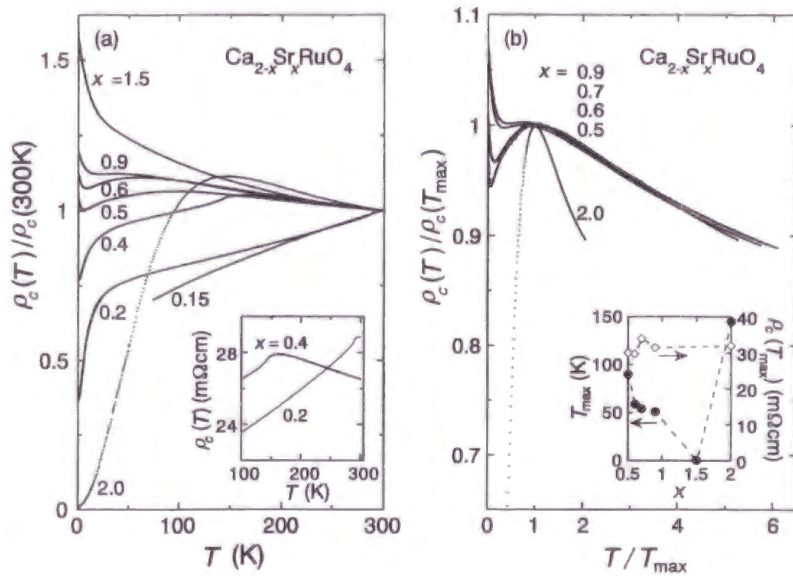


FIG. 9. (a) Temperature dependence of the out-of-plane resistivity $\rho_c(T)$ normalized by the values at 300 K for $\text{Ca}_{2-x}\text{Sr}_x\text{RuO}_4$ with different values of x . For $x=0.15$, the data are shown only above the M-NM transition point ~ 70 K. The inset illustrates the crossover at T_0 for $x=0.2$ and 0.4 . (b) The variation of $\rho_c(T)/\rho_c(T_{\max})$ against T/T_{\max} for several values of x in region III. The inset displays the x dependence of T_{\max} (solid circle) and $\rho_c(T_{\max})$ (open diamond).

$\rho_c(T)/\rho_{ab}(T)$ shows large anisotropy throughout the system. For example, the values for $x=0.2, 0.9, 1.5$, and 2 are 120, 130, 160, and 230 at 300 K and 780, 600, 2300, and 930 at 2 K, respectively. Therefore, the Fermi surface in this system must be remaining in almost cylindrical topology as that of Sr_2RuO_4 . Consequently, the interlayer transfer integral t_c should be so small that the in-plane scattering becomes a dominant process for the c -axis transport. In this case, one can write the jumping rate as¹³⁻¹⁶

$$\tau_c^{-1} = t_c^2 \tau_{ab} / \hbar^2, \quad (3.4)$$

where τ_{ab}^{-1} is the in-plane scattering rate and $h=2\pi\hbar$ is the Plank constant. From this equation, one can easily understand that even with this incoherent mechanism, ρ_c shows metallic behavior when ρ_{ab} is coherent so that τ_{ab}^{-1} becomes smaller on cooling. Hence, the metallic behavior in $0.15 \leq x < 0.5$ should arise from this mechanism.

The thermally assisted hopping process takes place when the thermal energy $k_B T$ is much larger than the effective bandwidth W_c for the c -axis transport. In this case, the jumping rate can be expressed as¹³

$$\tau_c^{-1} = \tau_{c0}^{-1} \exp[-(\alpha W_c / k_B T)^n], \quad (3.5)$$

where α is a numerical factor and n depends on the dimensionality of the hopping. This process explains the nonmetallic behavior at high temperatures.

First in region I, $\rho_c(T)$ for $x=0.15$ is metallic at all the temperatures measured down to the M-NM transition temperature of about 70 K. However in region II, a clear change-over from nonmetallic to metallic behavior has been observed across T_0 on cooling. [See the inset of Fig. 9(a) for $x=0.2$ and 0.4 .] As we discussed in Sec. III A, the structural transition at T_0 involves the lattice flattening, which should enhance the interlayer coherence by enlarging t_c . In contrast with the nonmetallic behavior due to the thermally assisted hopping at high temperatures, this increase in t_c by the transition must stabilize the diffusive hopping process below

T_0 , and thus more strongly metallic behavior appears with the Ca substitution.

In region III, however, the crossover in the temperature dependence occurs even without a structural transition, forming a maximum at T_{\max} . Figure 9(b) demonstrates a scaling with the normalized axes $\rho_c(T)/\rho_c(T_{\max})$ and T/T_{\max} in $0.5 \leq x \leq 0.9$. The inset of Fig. 9(b) illustrates the x dependence of T_{\max} and $\rho_c(T_{\max})$. Here $\rho_c(T_{\max})$ stays almost constant at around 32 m Ω cm, consistent with the result of the pressure dependence for Sr_2RuO_4 .¹³

In this case, since the thermally assisted hopping becomes effective when $k_B T$ is larger than $W_c = 4t_c$, the crossover temperature T_{\max} should be roughly proportional to t_c . In fact, this expectation is consistent with several observations. First, given this assumption, Eq. (3.5) qualitatively explains the nearly universal temperature dependence above T_{\max} as in Fig. 9(b).¹⁷ Second, on this assumption, T_{\max} shown in the inset of Fig. 9(b) indicates that W_c increases with decreasing x from 0.9 to 0.5. This is quite consistent with the expected enhancement in t_c due to the shrinkage of the interlayer distance $l=c/2$ as shown in Fig. 3. Moreover, the extension of the metallic region below T_{\max} toward $x=0.5$ is also understandable by Eq. (3.4) with this increase in t_c . Finally, Eq. (3.5) may reproduce the nearly constant $\rho_c(T_{\max})$ in this region, as discussed in Ref. 13.

Although the metallic region becomes wider with higher T_{\max} as x changes from 1.5 to 0.5, the incoherent conduction at low temperatures still remains even at $x=0.5$. This may be due to an anisotropic weak localization effect by disorders in (Ca/Sr)O layers, which basically retains the coherent conduction in RuO_2 layers. Once the structural transition occurs in region II, however, $\rho_c(T)$ finally becomes metallic with a strong decrease at low temperatures.

On the other hand, in this region III, T_{\max} decreases rapidly from $x=2$ to 1.5. The Ca substitution for Sr_2RuO_4 introduces not only randomness in SrO layers, but also distortion in RuO_2 layers. Actually, a recent powder neutron diffraction study confirms that the Ca substitution drives the rotation of RuO_6 octahedra along the c axis, which is absent in Sr_2RuO_4 .⁸ Hence, this rotational distortion as well as the

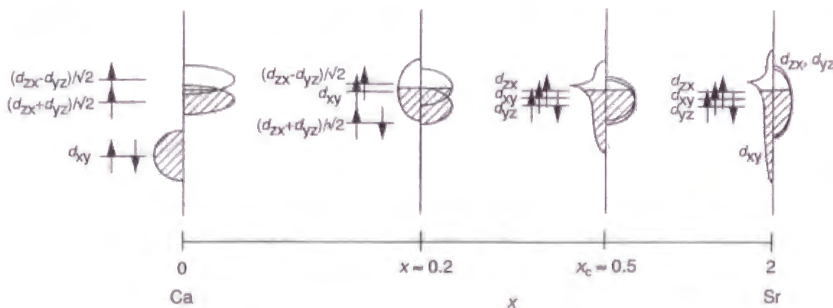


FIG. 10. Schematic variation of the electronic configuration in $\text{Ca}_{2-x}\text{Sr}_x\text{RuO}_4$ according to the band splitting model.

localization effect due to the randomness may be correlated with the incoherent $\rho_c(T)$ at $x = 1.5$.

To summarize this section, we confirmed by the above analyses that the c -axis transport in this system is dominated by the hopping process, which systematically changes from the diffusive metallic hopping to the thermally assisted one with the Sr content x and the temperature, characterized by the small t_c (\sim several 10 K) due to the quasi-two-dimensional electronic structure.

IV. DISCUSSION

A. Origin of the magnetoelastic coupling in Ca_2RuO_4

To understand those rich and unusual phenomena in $\text{Ca}_{2-x}\text{Sr}_x\text{RuO}_4$, we will discuss the variation of the ground-state magnetism and electronic structure. First, let us look into the Mott insulator Ca_2RuO_4 . The neutron diffraction measurement by Braden *et al.*⁵ has revealed strong magnetoelastic coupling in Ca_2RuO_4 . They reported severe flattening as well as tilting of RuO_6 octahedra on cooling toward its Néel temperature. The in-plane oxygen O(1) distance elongates along the b axis of the $Pbca$ unit cell, while the Ru-apical-oxygen O(2) bond shortens. However, once the staggered moment starts to align along the b axis, both flattening and tilting of RuO_6 octahedra saturate at lower temperatures.

Although the flattening of octahedra may be understood simply by the Jahn-Teller effect,¹⁸ in order to explain the strong magnetoelastic coupling, we have to take account of spin-orbit coupling. Since the flattening induces a distinct orthorhombic crystal field, the t_{2g} orbitals split into three nondegenerate ones such as $d_{x_0^2-y_0^2}$ with the lowest energy, $d_{z_0x_0}$ in the middle, and $d_{y_0z_0}$ with the highest energy. Here, the x_0 , y_0 , and z_0 axes correspond to the a , b , and c axes of the orthorhombic $Pbca$ unit cell, respectively. [If we take the x and y axes along the in-plane Ru-O bonds as in the $I4/mmm$ cell, $d_{x_0^2-y_0^2}$, $d_{y_0z_0}$, and $d_{z_0x_0}$ are transformed into d_{xy} , $(d_{zx} - d_{yz})/\sqrt{2}$, and $(d_{zx} + d_{yz})/\sqrt{2}$, respectively.] Basically, the tilting of RuO_6 octahedra along the b axis also stabilizes the above configuration, generating the orthorhombic crystal field by the second-nearest oxygens from a Ru ion. In this situation, the second-order perturbation theory for the spin-orbit coupling allows us to deduce that the b_0 axis should become the easy axis of the spin alignment, which agrees with the observation of Braden *et al.*⁵

At the same time, since the shortening of the out-of-plane Ru-O bond is nearly twice as much as the elongation of the in-plane one, the $d_{x_0^2-y_0^2}$ or d_{xy} orbital should have much

lower energy than the other two orbitals. Given the four electrons in the t_{2g} orbitals, such electronic structure may well realize a half-filled configuration at E_F [with two electrons in $(d_{zx} - d_{yz})/\sqrt{2}$ and $(d_{zx} + d_{yz})/\sqrt{2}$ orbitals as shown in Fig. 10], which favors AF superexchange coupling between neighboring spins. As a result, the orthorhombic distortion enhanced toward T_N stabilizes both the superexchange interaction and spin-orbit coupling in the Néel state. In this sense, the observed strong magnetoelastic coupling should be a cooperative phenomenon involving Jahn-Teller effect, superexchange, and spin-orbit coupling.

B. Ground-state crossover in the metallic region

1. Electronic configuration of Sr_2RuO_4

NMR studies have revealed that Sr_2RuO_4 exhibits exchange-enhanced paramagnetism with a local ferromagnetic coupling between in-plane spins at neighboring sites.^{19,20} The origin of this coupling should consist in the electronic configuration. Because the out-of-plane Ru-O bond is longer than the in-plane ones, d_{xy} should have slightly different energy among the t_{2g} orbitals. However, the two-dimensional spreading d_{xy} forms a γ band wide enough to degenerate with the $d_{yz,zx}$ orbitals that produce rather narrow α and β bands, reflecting their one-dimensional networks.¹⁰ Consequently, the Ru^{4+} t_{2g} band provides the electronic configuration of *four electrons in the triply degenerate band*. In addition, according to the band structure calculation,¹⁰ the γ band has a large peak in the density of states (DOS) near E_F due to van Hove singularity (vHS), and results in a strongly asymmetric DOS of the overall t_{2g} band.

According to the theories on ferromagnetism in strongly correlated systems,²¹ such an asymmetric DOS with a strong peak near E_F favors ferromagnetism for its ground state, while a symmetric, half-filled band stabilizes antiferromagnetism. Although the electronic configuration of Sr_2RuO_4 nearly satisfies the former condition, no substantial FM fluctuation has been detected so far. It is probably because of the rather low $N(E_F)$ that the FM fluctuations are not well developed to a wide range but remain local so as to realize the exchange-enhanced paramagnetism.²²

We note that a recent inelastic neutron scattering measurement has revealed the existence of incommensurate spin fluctuations located at $(\pm 0.6\pi/a, \pm 0.6\pi/a, 0)$.²³ This is consistent with the prediction of nesting instability between α and β bands by a band structure calculation.²⁴ One dimensionality of the $d_{yz,zx}$ orbital network results in this nesting

effect. For the superconductivity, however, we speculate that the local ferromagnetic coupling mentioned above possibly stabilizes the spin-triplet pairing of Sr_2RuO_4 , while the incommensurate spin fluctuations may have a minor or even an adverse effect. Mazin and Singh examined competition between p - and d -wave superconductivity by a calculation including both incommensurate and FM spin fluctuations, and drew a similar conclusion.^{24,25}

2. Band splitting model

The Ca substitution in Sr_2RuO_4 brings about the critical enhancement of the low-temperature susceptibility toward $x = 0.5$, which suggests that the structural instability point at $x_c \approx 0.5$ should be close to a FM instability. In contrast, it is the AF correlation that becomes substantial in the M-M region at $x < 0.5$. For the simplified picture of this switching of magnetic coupling, we propose the *band splitting model*, which is schematically illustrated in Fig. 10. In this model, the changes in the shape and filling of the band are vital to control the magnetism.

First, let us discuss the origin of the evolution of the FM correlation toward x_c in region III. While Sr_2RuO_4 has no structural distortion, the Ca substitution stabilizes and enhances the rotational distortion of RuO_6 octahedra along the c axis, as we mentioned in Sec. III C. As a consequence, the rotational distortion causes the following two main effects to enhance the FM coupling.

One is the band narrowing which enlarges $N(E_F)$. The distortion weakens the orbital hybridization and reduces the bandwidth. At the same time, since the structural symmetry remains tetragonal in region III, the crystal field symmetry around a Ru ion should be basically the same. Thus, the Ca substitution will neither lift the triple degeneracy of the bands nor blunt the vHS. Therefore, the system should keep basically the same asymmetric DOS which favors ferromagnetism. Additionally, the band narrowing will enhance the vHS, thereby $N(E_F)$ as well, so that the FM coupling gets stronger by the Stoner mechanism. This tendency is consistent with results by a recent mean-field theory based on the band structure of Sr_2RuO_4 .²⁶

Second, the rotation of octahedra will produce a stronger hybridization between d_{yz} and d_{zx} , which weakens the one-dimensional nature of α and β bands. Thus the nesting of these bands, the origin of the incommensurate spin correlation in Sr_2RuO_4 , may become weaker with decreasing x . As a result, rotational distortion should develop the FM coupling from the enhanced paramagnetism of Sr_2RuO_4 .

In the M-M region, however, the triple degeneracy must be lifted by the structural transition. The twofold anisotropy of the in-plane susceptibility below T_0 indicates the broken tetragonal symmetry, which lifts the degeneracy of d_{yz} and d_{zx} orbital bands: the α and β bands. As a neutron diffraction measurement has clarified,⁸ the O(1)-O(1) bond of octahedra splits into a shorter one along $[110]$ and a longer one along $[\bar{1}\bar{1}0]$ below T_0 , while the Ru-O(1) and Ru-O(2) bonds keep their lengths almost the same as those for $x = 0.5$ as well as for Sr_2RuO_4 . In addition, the tilt of RuO_6 octahedra occurs across the transition, which reduces the angle of the Ru-O(1)-Ru bond along $[010]$. Considering both the hybridization between the orbitals and the crystal field effect, the splitting in the bond length should bring about the

following band degeneracy lifting, similar to the discussion in Sec. IV A: the $(d_{zx} + d_{yz})/\sqrt{2}$ orbital will form a narrower band with a lower energy, whereas the $(d_{zx} - d_{yz})/\sqrt{2}$ will generate a wider band with a higher energy, as depicted in Fig. 10. Since the lowest-energy band absorbs more electrons, the filling of the bands at E_F decreases toward one-half. Taking account of the spin-orbit coupling, this model naturally explains the in-plane anisotropy of the susceptibility in the M-M region.

Moreover, the symmetry breaking distortion may lift the degeneracy of the states piled up at the vHS of the γ band, as what is discussed for the case in the Ca substitution of $\text{Ca}_{1-x}\text{Sr}_x\text{RuO}_3$.^{1,27} Therefore, due to the band splitting and the suppression of the vHS, the band at E_F will become more symmetric with smaller $N(E_F)$. This change from an asymmetric, strongly peaked band to a symmetric, half-filled band should weaken the FM coupling, but instead enhance the AF superexchange coupling in the M-M region.

In this model, the band degeneracy controls the electron filling of each band. This differs from the carrier doping to the single $d_{x^2-y^2}$ band of the high- T_c cuprates by chemical substitutions in block layers. In contrast with this type of "real space doping," the filling control here may be called "k-space doping."

We note here the significant dependence on this filling of magnetic coupling, from the FM one at x_c with 2/3 filling to the AF one at $x \approx 0.2$ with effectively half filling, while the shape of the DOS should also be vital for the switching of magnetic coupling as we discussed above. In fact, this dependence is consistent with theoretical studies by Alexander and Anderson²⁸ and by Moriya.²⁹ Based on a mean-field theory using the Anderson impurity model, they showed that the magnetic coupling switches from FM exchange to AF superexchange as the filling approaches one-half. Especially, Moriya predicted that such a switching occurs around 60% filling in the case with a simple band structure.²⁹ Notably, this suggests that the 2/3 filling in region III is already quite close to the critical point, as long as $N(E_F)$ is large enough, thereby with the asymmetric DOS.

Then, why does the band splitting occur below x_c instead of a FM ordering? In order to understand this, we have to take account of the orbital degree of freedom. As $N(E_F)$ increases with band narrowing, the triply degenerate bands are prone to meet a Jahn-Teller-type instability as well as a FM instability. In fact, the gap by the Jahn-Teller effect will stabilize the fourth electron in comparison with the degenerate case, and this stabilization energy becomes larger for a narrower band with higher $N(E_F)$. Therefore, we suggest that in region III, these instabilities compete with each other, and consequently the structural transition for the ground state takes over at x_c .

Moreover, orbital fluctuations and/or the dynamical Jahn-Teller effect as critical phenomena are expected on the verge of the instability point. This orbital fluctuation may lead to a nonuniform exchange interaction of spins through dynamical lifting of the orbital degeneracy. This dynamical coupling between spins and orbitals, which was recently suggested in the case of V_2O_3 ,^{30,31} would suppress a magnetic (especially FM) long-range order at around x_c .

Across $x \approx 0.2$ into region I, the first-order structural transition occurs² and induces another type of orbital ordering by the Jahn-Teller effect, as we discussed in Sec. IV A. Sup-

ported by this orbital ordering, the system finally achieves AF long-range order as well as the insulating ground state.

We conclude that the interplay between the band shape control and the k -space doping plays a crucial role in the dramatic variation of the ground states. The development of FM coupling toward the structural transition suggests a competition between the instabilities of ferromagnetism and Jahn-Teller orbital ordering. This competition results in the band degeneracy lifting to induce the switching of magnetic coupling. The rich and unusual phenomena of the quasi-two-dimensional Mott transition system $\text{Ca}_{2-x}\text{Sr}_x\text{RuO}_4$ should help deepen our insight into the role of the orbital degree of freedom in the Mott transition mechanism as well as in itinerant magnetism.

ACKNOWLEDGMENTS

The authors acknowledge T. Ishiguro for his support in many aspects, and M. Braden and O. Friedt for an important collaboration, especially for allowing us to use some of the unpublished information. They thank H. Fukazawa, M. Minakata, and S. Ikeda for their technical support and valuable discussions. They are grateful to K. Yamada, M. Sigrist, and M. Shiga for useful discussions. This work has been supported in part by a Grant-in-Aid for Scientific Research from the Ministry of Education, Science, Sports and Culture of Japan. One of the authors (S.N.) has been supported by JSPS Research Fellowships.

- ¹E.g., Y. Maeno, S. Nakatsuji, and S. Ikeda, in *Physics and Chemistry of Transition Metal Oxides*, edited by H. Fukuyama and N. Nagaosa (Springer-Verlag, Berlin, 1999), pp. 313–322.
- ²S. Nakatsuji and Y. Maeno, *Phys. Rev. Lett.* **84**, 2666 (2000).
- ³S. Nakatsuji *et al.* (unpublished).
- ⁴S. Nakatsuji, S. Ikeda, and Y. Maeno, *J. Phys. Soc. Jpn.* **66**, 1868 (1997).
- ⁵M. Braden, G. André, S. Nakatsuji, and Y. Maeno, *Phys. Rev. B* **58**, 847 (1998).
- ⁶H. Fukazawa, S. Nakatsuji, and Y. Maeno, *Physica B* **281&282**, 613 (2000).
- ⁷E.g., K. Yosida, *Theory of Magnetism* (Springer-Verlag, Berlin, 1996).
- ⁸O. Friedt, M. Braden, G. André, P. Adelman, S. Nakatsuji, and Y. Maeno, cond-mat/0007218 (unpublished).
- ⁹C.S. Alexander, G. Cao, V. Dobrosavljevic, S. McCall, J.E. Crow, E. Lochner, and R.P. Guertin, *Phys. Rev. B* **60**, R8422 (1999).
- ¹⁰T. Oguchi, *Phys. Rev. B* **51**, 1385 (1995); D.J. Singh, *ibid.* **52**, 1358 (1995).
- ¹¹T. Moriya, *Spin Fluctuations in Itinerant Electron Magnetism* (Springer-Verlag, Berlin, 1985).
- ¹²A.W. Tyler, A.P. Mackenzie, S. NishiZaki, and Y. Maeno, *Phys. Rev. B* **58**, R10 107 (1998).
- ¹³K. Yoshida, F. Nakamura, T. Goko, T. Fujita, Y. Maeno, Y. Mori, and S. NishiZaki, *Phys. Rev. B* **58**, 15 062 (1998).
- ¹⁴G. Soda, D. Jerome, M. Weger, J. Alizon, J. Gallice, H. Robert, J.M. Fabre, and L. Giral, *J. Phys. (Paris)* **38**, 931 (1977).
- ¹⁵L. Forro, V. Ilakovac, J.R. Cooper, C. Ayache, and J.-Y. Henry, *Phys. Rev. B* **46**, 6626 (1992).
- ¹⁶N. Kumar and A.M. Jayannavar, *Phys. Rev. B* **45**, 5001 (1992).
- ¹⁷The curve for $x=2$ in Fig. 9(b) is not on the universal one. This is probably caused by the fact that only Sr_2RuO_4 has no rotational distortion as we will discuss below, which results in the difference in parameters such as α and n in Eq. (3.5).
- ¹⁸As discussed below, it is owing to the flattening of the octahedra that the d_{xy} orbital will have lower energy than the other two. Therefore, the flattening is naturally explained by the Jahn-Teller effect to produce this orbital splitting, which stabilizes the fourth electron in comparison with the degenerate case.
- ¹⁹H. Mukuda, K. Ishida, Y. Kitaoka, K. Asayama, Z.Q. Mao, Y. Mori, and Y. Maeno, *J. Phys. Soc. Jpn.* **67**, 3945 (1998).
- ²⁰T. Imai, A.W. Hunt, K.R. Thurber, and F.C. Chou, *Phys. Rev. Lett.* **81**, 3006 (1998).
- ²¹J. Wahle, N. Blümer, J. Schlipf, K. Held, and D. Vollhardt, *Phys. Rev. B* **58**, 12 749 (1998) and references therein.
- ²²In addition to this basic mechanism, the local FM interaction may be stabilized by the Hund's rule coupling between moments induced on in-plane oxygen O(1) sites due to the strong covalency in Ru-O bonds, as discussed in Ref. 25.
- ²³Y. Sidis, M. Braden, P. Bourges, B. Hennion, S. NishiZaki, Y. Maeno, and Y. Mori, *Phys. Rev. Lett.* **83**, 3320 (1999).
- ²⁴I.I. Mazin and D.J. Singh, *Phys. Rev. Lett.* **82**, 4324 (1999).
- ²⁵I.I. Mazin and D.J. Singh, *Phys. Rev. Lett.* **79**, 733 (1997).
- ²⁶T. Nomura and K. Yamada, *J. Phys. Soc. Jpn.* **69**, 1856 (2000).
- ²⁷I.I. Mazin and D.J. Singh, *Phys. Rev. B* **56**, 2556 (1997).
- ²⁸S. Alexander and P.W. Anderson, *Phys. Rev.* **133**, A1594 (1964).
- ²⁹T. Moriya, *Prog. Theor. Phys.* **33**, 157 (1965).
- ³⁰M. Takigawa, E.T. Ahrens, and Y. Ueda, *Phys. Rev. Lett.* **76**, 283 (1996).
- ³¹W. Bao, C. Broholm, G. Aeppli, P. Dai, J.M. Honig, and P. Metcalf, *Phys. Rev. Lett.* **78**, 507 (1997).